Icarus 328 (2019) 246–273

Contents lists available at ScienceDirect

Icarus

journal homepage: www.elsevier.com/locate/icarus

The distribution, composition, and particle properties of Mars mesospheric aerosols: An analysis of CRISM visible/near-IR limb spectra with context from near-coincident MCS and MARCI observations

R. Todd Clancy[a,*], Michael J. Wolff[a], Michael D. Smith[b], Armin Kleinböhl[c], Bruce A. Cantor[d], Scott L. Murchie[e], Anthony D. Toigo[e], Kim Seelos[e], Franck Lefèvre[f], Franck Montmessin[f], Frank Daerden[g], Brad J. Sandor[a]

[a] Space Science Institute, 4750 Walnut Street, Suite 205, Boulder, CO 80301, USA
[b] NASA Goddard Space Flight Center, Greenbelt, MD 20771, USA
[c] Jet Propulsion Laboratory, California Institute of Technology, 4800 Oak Grove Dr., Pasadena, CA 91109, USA
[d] Malin Space Science Systems, 5880 Pacific Center Blvd., San Diego, CA 92121, USA
[e] John Hopkins University Applied Physics Laboratory, Columbia, MD 20723, USA
[f] Laboratoire Atmosphères Milieux Observations Spatiales, Paris, France
[g] Royal Belgian Institute for Space Aeronomy BIRA-IASB, Brussels, Belgium

A B S T R A C T

The Compact Reconnaissance Imaging Spectral Mapper (CRISM) onboard the Mars Reconnaissance Orbiter (MRO) obtains pole-to-pole observations (i.e., full MRO orbits) of vertical profiles for visible/near-IR spectra (λ = 0.4–4.0 μm), which are ideally suited to identifying the composition and particle sizes of Mars ice and dust aerosols over 50–100 km altitudes in the Mars mesosphere. Within the coverage limitations of the CRISM limb data set, a distinct compositional dichotomy is found in Mars mesospheric ice aerosols. CO_2 ice clouds appear during the aphelion period of Mars orbit (Solar Longitudes, L_s ~ 0–160°) at low latitudes (~20S–10N) over specific longitude regions (Meridiani, Valles Marineris) and at typical altitudes of 55–75 km. Apart from faint water ice hazes below 55 km, mesospheric H_2O ice clouds are primarily restricted to the perihelion orbital range (L_s ~ 160 – 350°) at northern and southern mid-to-low latitudes with less apparent longitudinal dependences. Mars mesospheric CO_2 clouds are presented in CRISM spectra with a surprisingly large range of particle sizes (cross section weighted radii, R_{eff} = 0.3 to 2.2 μm). The smaller particle sizes ($R_{eff} \leq 1$ μm) appear concentrated near the spatial (latitude and altitude) boundaries of their global occurrences. CRISM spectra of mesospheric CO_2 clouds also show evidence of iridescence, indicating very narrow particle size distributions (effective variance, V_{eff} ~ 0.03) and so very abrupt CO_2 cloud nucleation. Furthermore, these clouds are sometimes accompanied by altitude coincident peaks in 1.27 μm O_2 dayglow, which indicates very dry, cold regions of formation. Mesospheric water ice clouds generally exhibit small particle sizes (R_{eff} = 0.1–0.3 μm), although larger particle sizes (R_{eff} = 0.4–0.7 μm) appear infrequently. On average, water ice cloud particle sizes decrease with altitude over 50–80 km in the perihelion mesosphere. Water ice mass appears similar in clouds over a large range of observed cloud particle sizes, with particle number densities increasing to ~10 cm^{-3} for R_{eff} = 0.2 μm. Near coincident Mars Climate Sounder (MCS) temperature and aerosol profile measurements for a subset of CRISM mesospheric aerosol measurements indicate near saturation (H_2O and CO_2) conditions for ice clouds and distinct mesospheric temperature increases associated with mesospheric dust loading. Dayside (3 pm) mesospheric CO_2 clouds with larger particle sizes ($R_{eff} \geq 0.5$ μm) scatter surface infrared emission in MCS limb infrared radiances, as well as solar irradiance in the MCS solar band channel. Scattering of surface infrared emission is most strikingly presented in nighttime (3 am) MCS observations at 55–60 km altitudes, indicating extensive mesospheric nighttime CO_2 clouds with considerably larger particle sizes (R_{eff} ~ 7 μm). Mesospheric CO_2 ice clouds present cirrus-like waveforms over extensive latitude and longitude regions (10° × 10°), as revealed in coincident Mars Color Imager (MARCI) nadir imaging. Solar tides, gravity waves, and the large orbital variation of the extended thermal structure of the Mars atmosphere influence all of these behaviors. Mesospheric dust aerosols appear infrequently over the non-global (planet encircling) dust storm era of the CRISM limb data set (2009–2016), and exhibit smaller particle sizes (R_{eff} = 0.2–0.7 μm) relative to dust in the lower atmosphere. One isolated case of an aphelion (L_s = 96°) mesospheric dust layer with large dust particle sizes (R_{eff} ~ 2 μm) over Syria Planum may reflect high altitude, non-local transport of dust over elevated regions.

1. Introduction

The current CRISM limb analysis of aerosol scattering/absorption emphasizes mesospheric aerosol distributions, where global aerosol definitions are more restricted in prior observational studies relative to the lower atmosphere but are nonetheless eclectic with a long pedigree.

* Corresponding author.
E-mail address: clancy@spacescience.org (R.T. Clancy).

https://doi.org/10.1016/j.icarus.2019.03.025
Received 9 December 2018; Received in revised form 1 March 2019; Accepted 18 March 2019
Available online 26 March 2019

Mariner 9 (1971–1972), Viking (1976–1982), Pathfinder (1997), Mars Global Surveyor (MGS, 1997–2006), Mars Odyssey (MO, 2001–current), Mars Express (MEx, 2003–current), and Mars Reconnaissance Orbiter (MRO, 2006–current) observations from a variety of measurement wavelengths (ultraviolet to thermal IR) and observational approaches (nadir and limb imaging, spectroscopy, and occultations) have characterized individual elements of ice and dust aerosols in the Mars mesosphere. Mariner 9 (Anderson and Leovy, 1978) and Viking (Jaquin et al., 1986) limb imaging first defined the vertical extension of aerosols to altitudes above 50 km.

Pathfinder descent and imaging observations first suggested the existence of mesospheric CO_2 ice clouds (Clancy and Sandor, 1998; Magalhães et al., 1999). Since then, low latitude aphelion CO_2 clouds have become the most actively studied of Mars mesospheric aerosols, partly because they are (were) novel but also due to the range of Mars missions and instruments deployed shortly after their discovery. The very distinct spatial/seasonal distributions of these clouds have been characterized from MGS Thermal Emission Spectrometer (TES) limb scans and Mars Orbiter Camera (MOC) limb imaging (Clancy et al., 2007), OMEGA (Observatoire pour la Minéralogie, l'Eau, les Glaces et l'Activité) nadir imaging (Määttänen et al., 2010; Montmessin et al., 2007), THEMIS (Thermal Emission Imaging System) mapping (McConnochie et al., 2010), and CRISM nadir imaging (Vincendon et al., 2011). Direct spectroscopic confirmation of their CO_2 composition was first obtained from nadir OMEGA observations (Montmessin et al., 2007), and most recently from Planetary Fourier Spectrometer (PFS) observations (Aoki et al., 2018). Mesospheric CO_2 clouds have also been tentatively identified in MCS observations (Puspitarini et al., 2016; Sefton-Nash et al., 2013). Several observational approaches have been applied to define CO_2 cloud particle sizes (Määttänen et al., 2010; Montmessin et al., 2007; Vincendon et al., 2011).

Specific water ice aerosol identifications in the mesosphere are surprisingly limited to date. The distribution of "loop" cloud detections in MRO Mars Climate Sounder (MCS) thermal infrared and visible (solar integrated) band limb scans within the mesosphere indicate detached layer aerosols must be quite common in the perihelion season over a wide range of latitudes (Sefton-Nash et al., 2013, including geometric definition of "loop" clouds), although the presented spectral band analysis is not very specific to composition. MCS profile retrievals do return dust and water opacities (but not CO_2 ice, which affects the temperature retrieval) up to 80 km altitudes, based on thermal infrared (e. g.; 12 μm for water ice, 22 μm for dust — Kleinböhl et al., 2009) radiance distinctions. These have not, as yet, been a focus of published analysis apart from specific dust studies indicated below (Heavens et al., 2015; Kleinböhl et al., 2015), and a more recent analysis of hydrogen escape rates as inferred from MCS profile retrievals for mesospheric water ice clouds (Heavens et al., 2018). There are also a number of mesospheric aerosol analyses that clearly point to widespread mesospheric water ice clouds, based on near-IR spectral analysis (Vincendon et al., 2011), correspondence with vertical-horizontal structure or thermal considerations (Clancy et al., 2010; Fedorova et al., 2009; Määttänen et al., 2010; McConnochie et al., 2010; Vincendon et al., 2011).

Specific dust aerosol identifications in the Mars mesosphere, in the absence of global dust storm conditions, are still rarer. Mariner 9, MGS, and MRO limb observations presented the global extension of dust and related ice aerosols into the mesosphere during the 1972 (Anderson and Leovy, 1978), 2001 (Clancy et al., 2010), and 2007 (Kleinböhl et al., 2013) planet encircling dust storms, respectively (MY9, MY25, MY28). As we indicate in the following CRISM analysis of the 2009–2017 period during which such global dust storms did not occur, mesospheric dust aerosols are uncommon. This conclusion supports a recent analysis of 50–80 km MCS dust retrievals (Kleinböhl et al., 2015), challenging the identification of widespread dust layers at 50–60 km based upon TES limb retrievals (Guzewich et al., 2013). However, MCS observations of mesospheric detached dust layers are reported over high elevation regions, associated with topographically forced, mesoscale circulations (Heavens et al., 2015).

The following analysis and presentation regard the distribution of Mars atmospheric aerosols over the 50–100 km mesospheric region, in which the seasonal (solar longitude, L_s), spatial (latitude and altitude, primarily), compositional (water ice, CO_2 ice, and dust), particle size distribution (effective radius, R_{eff}, primarily and effective variance, V_{eff}, in special cases), and limb path averaged abundances (optical depths) are derived from limb imaged visible/near-IR (0.4–4 μm) spectra. These 2009–2016 CRISM (Compact Reconnaissance Imaging Spectrometer for Mars) limb spectra extend from the surface of Mars to above 120–150 km altitudes with better than 0.5 km vertical resolution, and obtain full latitudinal and nearly complete (although irregularly sampled) seasonal coverage as accumulated over multiple Mars years (MY29–33, as defined in Clancy et al., 2000). The retrieved aerosol behaviors are considered in the context of mesospheric water vapor abundances (including anomalous $O_2(^1\triangle_g)$ dayglow peaks), water and CO_2 ice formation processes (including cloud iridescence), and near-coincident Mars Color Imager (MARCI) and Mars Climate Sounder (MCS) observations from the same Mars Reconnaissance Orbiter (MRO).

The extended spatial/temporal coverages of CRISM visible/Near-IR limb spectra prove quite diagnostic for the study of Mars mesospheric aerosols; due to reduced limb optical depths (relative to the lower atmosphere) that support uniform vertical coverage, and contiguous 0.4–4 μm spectral resolution ($\delta\lambda \sim 0.01$ μm) that supports accurate definitions of an extensive range of aerosol particle sizes (and sometimes V_{eff}) presented by Mars mesospheric aerosols. This study demonstrates that Mars mesospheric aerosol distributions are quite distinct from those extensively characterized at altitudes below 50 km; in terms of considerably smaller particle sizes, distinct dust and ice spatial and temporal distributions, and the presence of low latitude CO_2 ice clouds in the aphelion season. Dust aerosols (apart from global dust storm activity) are much less prominent and water ice and CO_2 ice aerosols appear nearly exclusively within perihelion and aphelion annual portions of the Mars orbit, respectively. These distinctions in the spatial/temporal distributions of mesospheric dust and ice aerosols and their particle size distributions are a focus of this study. Although this CRISM limb analysis primarily employs 1-D limb profile spectra, we also provide a subset of CRISM limb images characterizing the ~50 km horizontal structure of mesospheric aerosols as viewed orthogonally to the limb optical paths.

MCS and MARCI near-coincident and near-simultaneous comparisons provide a key component of the current study as well. In particular, MARCI wide-angle (daily global) imaging provides characterization of kilometer resolved morphologies and horizontal scales of mesospheric aerosol distributions along the ~300 km CRISM limb sampling path. Hence, MARCI comparisons serve to constrain cloud particle densities and processes sampled in CRISM limb retrievals. MCS has obtained the most complete temporal (including diurnal) and spatial limb profiling data set of Mars atmospheric aerosols over 2006–2018, including mesospheric (50–80 km) profiling with dense latitudinal coverage contributed by rapid in-orbit-plane limb scanning. MCS obtains thermal infrared (12–45 μm) limb radiances appropriate to dust and water aerosol retrievals (Kleinböhl et al., 2009), but also offers sensitivity to scattering of surface continuum emission by CO_2 cloud particles (Hayne et al., 2012; Puspitarini et al., 2016). Apart from identifying consistent dust and water ice detections in the MCS and CRISM limb measurements, we consider the distinct sensitivities of MCS and CRISM limb measurements for mesospheric CO_2 clouds, and the unique sensitivity of MCS radiances to nighttime (3 am) mesospheric CO_2 clouds. Inter-comparison of MRO MCS, MARCI, and CRISM mesospheric aerosol measurements constitutes a unique opportunity for near-coincident, simultaneous views of Mars atmospheric aerosols in nadir and limb geometry over two orders of magnitude wavelength coverage (0.4–45 μm).

Table 1
CRISM Limb $O_2(^1\Delta_g)$ dayglow observation summary (each entry is one full orbit of observations).

Date[a]	Year[b]	MY[c]	L_S[d]	Longitudes[e]	Latitudes[f]
July 10, 11	2009	29	301°	H, T	88S–56N
February 10, 11	2010	30	50°	T	51S–85N
April 7	2010	30	74°	H, T	42S–87N
April 28, 29	2010	30	83–84°	H, T	43S–87N
May 26	2010	30	96°	H, T	39S–86N
August 22, 23	2010	30	137°	0, 100–210W	50S–25S
August 22, 23	2010	30	137°	0, 100–140W	41N–84N
October 17	2010	30	166°	H, T	64S–82N
December 5, 6	2010	30	193°	H, T	83S–63N
March 31–April 1	2011	30	265°	H, T	87S–39N
May 14, 15	2011	30	292–293°	H, T	86S–44N
June 28	2011	30	319°	H, T	85S–52N
August 22, 23	2011	30	349°	H, T	81S–65N
September 13	2011	31	0°	H, T	76S–70N
December 10, 11	2011	31	41–42°	H, T	54S–87N
April 24, 26	2012	31	101–102°	H, T, M	40S–86N
November 14–16	2012	31	206–208°	H, M, V	84S–64N
January 8, 9	2013	31	241°	M, V	87S–47N
March 7	2013	31	277°	H	75S–19S
December 11, 13	2013	32	61–62°	M, V	38S–87N
February 5, 6	2014	32	86°	H, V	27S–86N
April 1–3	2014	32	110–111°	H, M, V	36S–81N
May 26–28	2014	32	136–137°	H, M, V	37S–85N
July 20, 22, 26	2014	32	164–167°	H, M, V	54S–86N
February 13, 14	2015	32	290–291°	H, M	79S–48N
April 15, 17	2015	32	326–327°	H, M, V	86S–66N
August 31, September 1, 4	2015	33	35–37°	H, M, V	48S–86N
October 25, 30–31	2015	33	59–62°	H, M, V	37S–80N
December 20, 23, 25	2015	33	84–86°	H, M, V	33S–85N
February 28, March 4, 5	2016	33	115–118°	H, M, V	34S–87N
May 10, 11, 15	2016	33	150–153°	H, M, V	47S–87N
July 3, 5, 6	2016	33	179–181°	H, M, V	65S–83N
August 30	2016	33	213°	H	83S–3N
December 21	2016	33	284°	M	87S–56N

[a] Day/Month of CRISM orbit of observations.
[b] Year of CRISM orbit of observations.
[c] Mars Year of CRISM orbit of observations, as in Clancy et al. (2000).
[d] Mars Solar Longitude (90° for northern summer solstice, 70° for aphelion).
[e] EQ Longitude of CRISM orbit of observations (H ~ 295W, T ~ 105W, M ~ 0W, V ~ 75W).
[f] Latitudinal Coverage of CRISM orbit of observations (at 6–12° latitude intervals).

2. CRISM limb spectroscopic/imaging observations

The CRISM visible-near infrared (λ = 0.4–4 μm, 7–15 nm resolution) imaging spectrometer has mapped Mars surface mineralogy at high spatial resolution (15–20 m/pixel) from the MRO near-polar, sun synchronous orbit (local time, LT, ~3 pm/3 am) since November of 2006. CRISM instrumental and science capabilities, including early results, are provided in Murchie et al. (2007, 2009). CRISM is nominally operated in the nadir but, beginning in 2009, CRISM limb observations have been obtained through MRO spacecraft yaw maneuvers for 1–3 orbits/longitudes scheduled roughly every 30° of Mars solar longitude (L_S). However, numerous interruptions associated with MRO spacecraft or CRISM instrumental considerations (particularly degrading CRISM coolers in later years) contribute an irregular pattern of seasonal and MY coverage, as indicated in Table 1. The final CRISM limb measurements employed for analysis (i. e., with near-IR spectral coverage) were obtained in December of 2016. CRISM limb observations formally ended in November of 2017 when IR detector cooling became inoperable.

2.1. CRISM limb observation coverages

During CRISM limb operations, spacecraft yaws were employed to place the CRISM field-of-view (fov) at the atmospheric limb in the plane of the MRO orbit. The CRISM gimbal drive, nominally applied to obtain contiguous surface spectroscopic imaging in the nadir, also supports atmospheric limb scanning from the surface to altitudes above 120–150 km (Clancy et al., 2012). This atmospheric limb scanning mode leads to roughly 500 m vertical resolution with horizontal spatial imaging of ~200 m resolution spanning approximately 30 km fovs orthogonal to the limb path, all with full visible/near-IR spectral coverage. CRISM limb scans were obtained in the aft (backward) direction of the orbit plane until April of 2012 and subsequently in the bow (forward) direction. This change in the CRISM limb scan direction correlates with the appearance of a faint background spectral signature that sets the lower limit of retrievable aerosol scattering, as discussed subsequently.

CRISM limb observations were generally taken over 2–3 full orbits observed within a 1–5 day period every 2–4 months (as indicated above). By comparison, the MRO spacecraft obtains 780 orbits during a 2 month period. The near-polar orbit of MRO provides for full latitudinal coverage from each orbit of observation. The longitudinal coverage is limited to 4 selected longitudes of interest, centered on Hellas Basin (H — 295W), the Tharsis ridge (T — 105W), Meridiani (M — 0W), and Valles Marineris (V— 75W). Longitudes here refer to the equatorial (EQ) crossing of the orbit, and change considerably at very high latitudes (particularly over the poles) due to the slightly inclined MRO polar orbit. As apparent in Table 1, the longitudes of CRISM limb viewing were limited to 2 orbits centered on Hellas and Tharsis regions over 2009–2011 and then modified to 3 orbits centered on Hellas, Meridiani, and Valles Marineris from 2012 to 2016. The latter two longitude regions correspond to peak occurrences of mesospheric (55–75 km) CO_2 ice clouds, which are particularly well characterized by CRISM visible-to-near infrared spectra in limb viewing.

The latitudinal sampling varies with altitude and latitude along the orbit, depending on the range of solar illuminated latitudes employed for aerosol scattering analysis (a function of L_S), and the altitude gimbal scanning pattern. Generally, there are 6–14° latitudinal offsets between limb scans, which does not support the kind of detailed discrete ("loop") limb cloud analysis associated with the rapid limb scanning operations of the MCS instrument. A discrete cloud viewed at a true limb tangent altitude of 65 km in CRISM limb spectra is projected (for 10 degree latitudinal limb scan spacing) to 45 km altitudes in the preceding and following limb scans. This behavior can be identified for particularly bright mesospheric CO_2 ice clouds but is less apparent for H_2O ice clouds, which are less bright and less spectroscopically distinct from lower altitude aerosols (particularly in their non-aphelion season of occurrence when 40–50 km dust and ice aerosols are much more prominent). With the (sometimes) exception of vertically extended polar hood clouds, Mars mesospheric cloud scattering is dominated by horizontally discrete scattering layers exhibited as distinct limb brightness maxima projected at altitude along the limb viewing path.

Consequently, the following analysis emphasizes CRISM spectral brightness fits for aerosol composition and R_{eff} at the specific altitudes of such brightness peaks, adopting a very simplified single scattering approach. In cases where brightness peaks at multiple altitudes are observed, we model each peak independently, assigning an altitude equivalent to its projected altitude. This projected altitude (aeroid altitudes are used throughout this presentation) is less than or equal to its true aeroid altitude, depending on its location along the viewed limb path. We also pursue limb profile retrievals, employing multiple-scattering RT and assuming spherical shell symmetry, for a small subset of the CRISM limb data. This serves to assess the accuracy of the single-scattering analysis for aerosol composition and particle size on the full data set, but also provides determination of limb path aerosol opacity. In the context of these derived R_{eff}, limb opacities, and assumptions on cloud horizontal scales (informed by MARCI nadir imaging), effective cloud particle number densities are estimated. These approaches are defined in more detail subsequently, but are mentioned here in the context of the employed CRISM limb profiling data set. Apropos to the

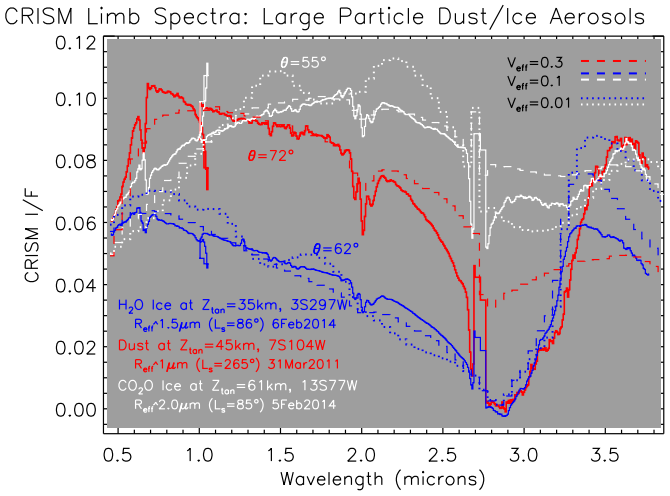

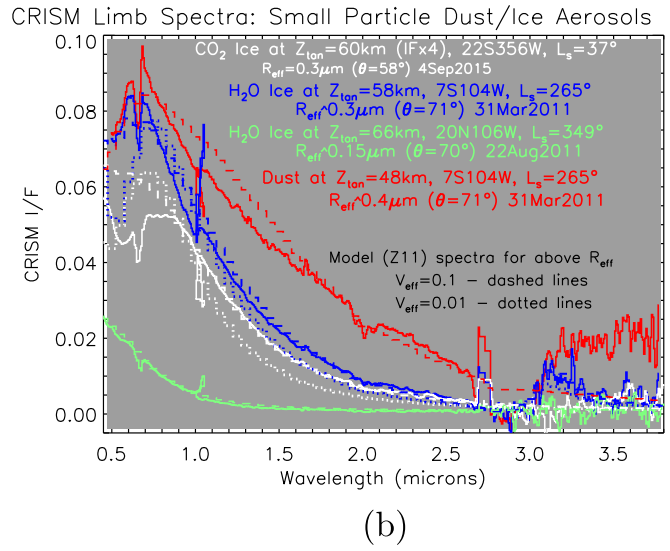

Fig. 1. Two sets of CRISM limb spectra are presented for larger particle sizes (upper, R_{eff} = 1–2 μm) and smaller particle sizes (lower, R_{eff} = 0.15–0.4 μm). Observed limb spectra (solid lines) are compared to single scattering model fits (dashed and dotted lines) for spectrally identified dust (red), H_2O ice (blue, green), and CO_2 ice (white) clouds with best fit particle sizes (R_{eff}). In the case of ice particle size distributions, two cases for the size distribution variance (V_{eff} = 0.1, 0.01) are plotted to indicate reflectance spectra sensitivity to this parameter. Later figures more clearly demonstrate observed spectral reflectances indicative of very narrow size distributions and, hence, cloud iridescence. Dates, locations, season (L_s), and scattering angles (θ) for the various observations are presented in the figure.

single altitude approach, the horizontal (orthogonal to the limb optical path) imaged resolution is averaged to form a single vertical profile for each CRISM limb scan, although individual cases of mesospheric ice cloud limb images (CO_2 clouds, in particular) are presented.

2.2. CRISM limb spectra characteristics for mesospheric aerosols

Fig. 1 presents examples of CRISM limb spectra for the three aerosol compositions relevant to the Mars mesosphere (dust, H_2O ice, CO_2 ice), for larger (R_{eff} = 1–2 μm, Fig. 1a) and smaller (R_{eff} = 0.15–0.4 μm, Fig. 1b) effective particle sizes. The solid colored lines (red — dust, white — CO_2 ice, blue — H_2O ice, green — very fine H_2O ice) display the observed limb radiances at the indicated tangent altitudes (35–61 km) in terms of Lambert reflectance (I/F, or 4 × I/F for the small particle size CO_2 ice case). Limb tangent reflectance spectra at altitudes below the mesosphere are presented in Fig. 1b for the dust and H_2O ice cases in order to provide large aerosol particle cases that are not common in the mesosphere. Notice that small dust particle sizes (R_{eff} = 0.4 μm) at 48 km altitudes overlie larger dust particle sizes (R_{eff} = 1.0 μm) at 45 km altitudes, indicating strong vertical gradients in dust particle sizes just below the mesosphere at this time (L_s = 265°). By comparison, large particle size CO_2 clouds are common in the mesosphere. In all of the analyzed mesospheric limb spectra, limb I/F correspond to optically thin conditions as averaged over the limb optical path, although optically thick conditions may exist locally along the optical path for bright CO_2 clouds in particular. Distinct discontinuities in the CRISM spectra are exhibited near 0.7, 1.1, and 2.7 μm, associated with CRISM spectrometer and order filter boundaries (Murchie et al., 2007). Dotted and dashed line spectral fits, as described subsequently, demonstrate how basic single scattering models represent these observed limb radiances for the indicated aerosol compositions and particle size distributions (R_{eff} and V_{eff}). We reiterate that these model single-scattering fits do not obtain aerosol scattering opacities, but are simply scaled in magnitude to match the observed limb I/F over the full observed spectral shape.

For the generally small particle sizes of Mars atmospheric aerosols (i. e., compared to surface ice), visible/near-IR absorption is most apparent in dust aerosol absorption shortward of 0.6 μm (associated with Fe charge transfer) and dust and H_2O ice aerosol absorption over the 2.7 to 3.2 μm spectral range (associated with OH stretching). Both of these absorptions (and CO_2 gas absorptions at 2 and 2.7 μm) are further imprinted on limb aerosol scattering spectra through reflected illumination from the surface and lower atmospheric dust and H_2O ice clouds. CO_2 ice clouds are non-absorbing over the CRISM wavelength coverage (apart from 2.7 μm absorption overlain by very strong CO_2 gas band absorption), but their limb scattering spectra are also modified by this reflected illumination of the surface and lower atmosphere. Fig. 2 presents the single scattering cross-section (σ_{scat}) and albedo (ω_{scat}) for dust, H_2O ice, and CO_2 ice spheres with smaller (R_{eff} = 0.5, V_{eff} = 0.1) and larger (R_{eff} = 1.5, V_{eff} = 0.1) particle size distributions (assuming gamma size parameterizations; Hansen and Travis, 1974). The spectral character of σ_{scat} (top panel of Fig. 2) roughly mimics the observed limb spectra for dust and ices for the limb scattering angles represented in

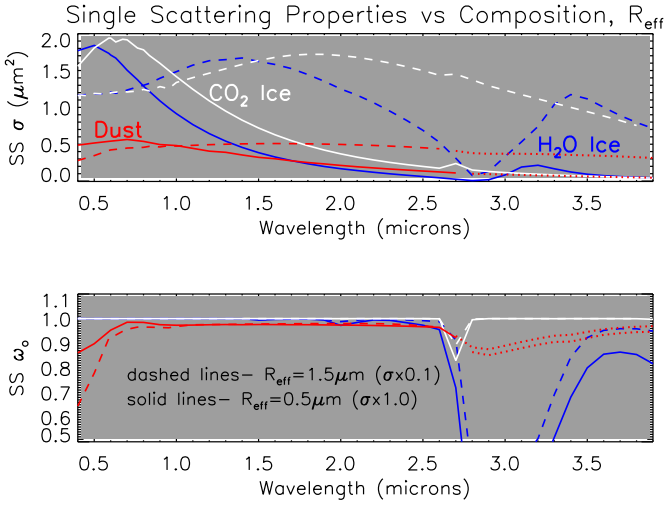

Fig. 2. Model single scattering cross sections (upper) and albedos (lower) are presented for smaller (solid lines, R_{eff} = 0.5 μm) and larger (dashed lines, R_{eff} = 1.5 μm) particle size distributions (V_{eff} = 0.3 for dust — red lines; V_{eff} = 0.1 for CO_2 ice — white lines and H_2O ice— blue lines). These scattering angle integrated properties were calculated for spheres versus wavelength over the CRISM spectral range, employing optical indices from Hansen (2005), Warren and Brandt (2008) and Wolff et al. (2009).

the CRISM spectra of Fig. 1 (θ = 55–71°). However, as demonstrated below, limb aerosol scattering spectra depend significantly on scattering angle over the extended range of θ sampled in CRISM limb observations (34–144°).

Nevertheless, the general characteristics of these visible/near-IR scattering spectra are: 1) peak reflectance at a wavelength near the R_{eff} of the scattering aerosol, 2) a characteristic H_2O scattering peak over wavelengths of 3–3.5 μm that decreases in wavelength and amplitude with decreasing ice particle size, 3) enhanced scattering by dust over near-IR wavelengths (1.5–2.5 and 3.2–3.8 μm), and 4) spectrally featureless scattering by CO_2 ice apart from interference effects associated with very narrow particle size distributions (dotted lines, Fig. 1 models — iridescence, as discussed later). One caveat, with respect to the dust spectral analysis, is that we do not have consistent optical constants beyond a wavelength of 2.6 μm, the wavelength limit of the dust optical constant analysis of Wolff et al., 2009. Values for dust optical constants longward of 2.6 μm are drawn from Määttänen et al., 2009, which lead to less accurate dust fits in this region. The mismatch in observed/modeled dust spectra in Fig. 1 and the dotted lines for the dust scattering properties in Fig. 2 for wavelengths beyond 2.6 μm reflect this limitation. However, mesospheric dust aerosols, particularly for larger particles (Fig. 1a), are not substantially represented in the 2009–2016 CRISM limb observations of mesospheric aerosols.

The scattering parameters provided as a function of wavelength in Fig. 2 are integrals with respect to scattering angle, whereas the CRISM limb spectra reflect direct scattering of solar flux at a fixed scattering angle and scattering of the approximately hemispheric illumination of solar flux reflected by the underlying surface and lower atmosphere. The proportion of these illumination sources is roughly 5:1 for a lower boundary reflectance of order 0.2. Hence, the scattering observed from mesospheric aerosols in CRISM limb spectra is dominated by the direct solar illumination at the specific scattering angle associated with the latitude, season (L_S), LT, and limb pointing direction. Clearly, the absolute brightness of the observed aerosol scattering will increase dramatically from backward to forward scattering, but the spectral shape of the limb reflectance spectra will also change, particularly for smaller aerosol particle sizes. Fig. 3 demonstrates such scattering angle (θ) sensitivity for fine mesospheric H_2O ice clouds observed at 41S (θ = 100°) and 44N (θ = 39°) at L_s = 293° in MY30. The strong spectral distinctions between these observed limb spectra are contributed in large part by the distinct scattering angles of observation. Model fits for R_{eff} for these northern and southern mid-latitude mesospheric clouds yield 0.15 μm (diamond symbols) and 0.3 μm (triangle symbols), respectively. However, model reflectance spectra for R_{eff} = 0.2 μm (asterisk symbols) indicate that their distinct scattering angles account for the largest differences in their limb reflectance spectra.

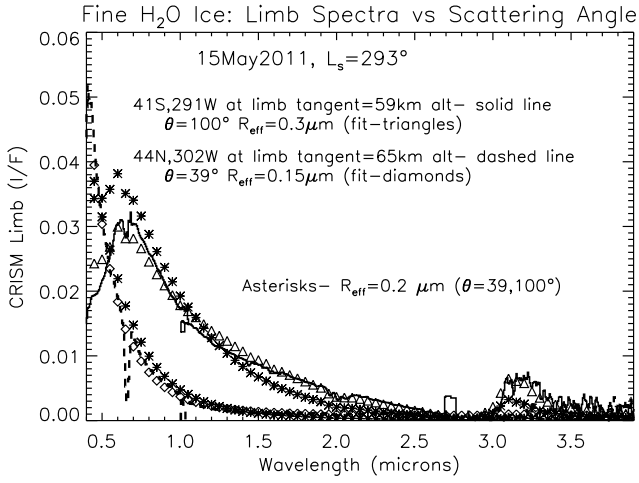

Fig. 3. The sensitivity of the observed (lines) and modeled (symbols) limb reflectance spectra to scattering angle is strong, for smaller particle sizes in particular. H_2O ice clouds observed at a scattering angle (θ) of 100° (41S, solid line) are fit with R_{eff} = 0.3 μm (triangle symbols). H_2O ice clouds observed at a scattering angle of 39° (44N, dashed line) are fit with R_{eff} = 0.15 μm (diamond symbols). The largest spectral distinction between these observed limb reflectance spectra is associated with their very distinct scattering angles of observation. This is demonstrated by model reflectances calculated for R_{eff} = 0.2 μm at scattering angles of 100° and 39°, both of which plotted as asterisk symbols.

Clearly, it is necessary to simulate scattering phase functions for ice and dust compositions over a large range of particle sizes in order to derive accurate values for R_{eff} and composition from these limb spectra. Fortunately, the spectral shape variations with scattering angle indicated in Fig. 3 are not very sensitive to the specific particle shapes adopted for these scattering phase function calculations. For much of the following analysis, we adopt equidimensional (D = L), randomly oriented cylinders for calculation of single scattering phase functions versus wavelength, employing the T-matrix code of Mishchenko et al. (1996, 2016). This choice reflects current models for cirrus ice cloud particle shapes in the upper troposphere (Yang et al., 2003) and is also qualitatively consistent with the observation of iridescence in mesospheric CO_2 clouds (as discussed subsequently). Fig. 4 demonstrates that CRISM spectra of mesospheric scattering, for small H_2O ice as in Fig. 3, are not particularly sensitive to this particle shape choice. CRISM limb spectra calculated for the scattering angles and R_{eff} = 0.2 μm of Fig. 3 are compared for assumed particle shapes of spheres (dotted lines), equidimensional cylinders (D/L = 1, solid lines) and elongated cylinders with (D/L = 0.5, dashed lines). The differences among the calculated scattering spectra, which are again scaled for comparison of spectral shapes, are small and contribute minor uncertainties in terms of deriving aerosol composition and particle sizes from CRISM limb spectra of mesospheric aerosol scattering.

Aerosol optical indices versus wavelength for dust, H_2O ice, and CO_2 ice are adopted from Hansen (2005), Warren and Brandt (2008), and Wolff et al. (2009), respectively. The aerosol particle size distribution function (gamma distribution function, Deirmendjian, 1964) and variances (V_{eff} = 0.1 for ice; 0.3 for dust) are assumed from prior analyses (Clancy et al., 1995; Clancy et al., 2003; Curran et al., 1973; Tomasko et al., 1999; Toon et al., 1977; Wolff et al., 2009). These assumptions are effectively unconstrained by the CRISM limb spectra, and the derived compositions and R_{eff} are generally insensitive to their adoption.

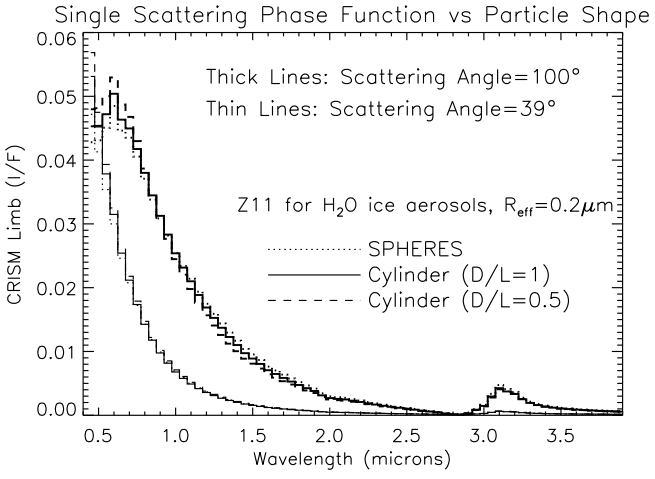

Fig. 4. While limb scattering spectra are sensitive to scattering angle, they are much less sensitive to the details of the aerosol particle shapes. Model limb reflectance spectra for three particle shapes (spheres — dotted lines, equidimensional cylinders — solid lines, and cylindrical columns — dashed lines) are compared for forward (θ = 39°, thin lines) and side (θ = 100°) scattering angles.

However, interference patterns exhibited in a significant number of the observed CO_2 ice aerosols (i. e., iridescence) do provide some constraints on V_{eff}, as discussed below. In order to characterize the necessary ranges of composition, R_{eff}, and V_{eff} exhibited in CRISM limb spectra of Mars mesospheric aerosols, over 100 specific single scattering phase functions were calculated via the T-matrix analysis.

3. Single scattering fits for aerosol composition and particle size (R_{eff})

A very simple approach is adopted to derive mesospheric aerosol composition and particle size versus altitude, latitude, longitude, and season based on CRISM visible/infrared spectroscopy of the imaged/scanned atmospheric limb of Mars. The limb brightness spectra of ~470 limb brightness peaks are identified in the full CRISM limb data set (Table 1) and best fit (by visual inspection) with a two-term single scattering model for definition of composition (dust, H_2O ice, CO_2 ice) and particle size (R_{eff} = 0.1–3.0 μm).

$$I/F_M(\lambda) = C \times \left[Z(\theta,\lambda) + R(\lambda) \times \sum_{\theta=30}^{150} Z(\theta,\lambda)/121 \right]$$

The first, dominant term contributing to the observed spectral limb brightness is direct scattering of incident solar irradiance, associated with the single scattering phase function $Z(\theta, \lambda)$. The second term is aerosol single scattering $[Z(\theta, \lambda)]$ of the diffusely reflected solar irradiance from the lower atmosphere and surface, $R(\lambda)$, which is defined by the CRISM observed surface/atmosphere reflectance spectrum measured at the lower boundary of each limb scan. This second scattering term is summed over a representative range of scattering angles (θ = 30–150°) from this lower boundary reflecting layer to the mesospheric cloud to the MRO spacecraft. This simple scattering approach does not account for thermal emission contributions, which can be significant for wavelengths longward of 3.5 μm. However, mesospheric aerosol emission is reduced by the lower atmospheric temperatures in this region such that thermal emission contributions are dominated by aerosol scattering of surface thermal emission rather than aerosol emission. Furthermore, CRISM spectral noise limits the useful application of limb signal beyond ~3.8 μm. Hence, thermal emission is not particularly relevant for the current study. It is, however, incorporated in the set of multiple scattering RT limb retrievals presented for comparison in a following section.

The scaling constant, C, indicates that there is no attempt to characterize limb optical depths with this approach, only the aerosol composition and particle size are defined through the spectral shape of the observed limb scattering (Fig. 1). One of the issues in limb analysis is the assumption of spherical shell symmetry, which is clearly not appropriate for discrete aerosol layers. Such discreteness along the limb optical path can be identified by an abrupt decay of limb brightness below the peak brightness altitude (Clancy et al., 2007). We address limb opacity with a separate radiative transfer approach on a subset of CRISM limb observations, with added assumptions about the horizontal cloud extent in order to estimate cloud particle number densities.

Figs. 5–8 provide a sampling of these single scattering best fit spectra to CRISM limb spectra for a range of aerosol particle sizes and compositions. As indicated above, best fit solutions (symbols in Figs. 5–8) to the observed CRISM spectra (lines in Figs. 5–8) are obtained visually rather than by minimization of differences between the observations and models at specific wavelengths. It is not simple to devise a stable and accurate least-squares-type fit given the range of observational parameters (wavelength, scattering angle) and aerosol properties (composition, R_{eff}, V_{eff}) that characterize CRISM limb spectra of mesospheric aerosol scattering. In order to verify the visual fitting method adopted for the full CRISM limb data set, we employ vertical profile retrievals employing minimization of model/data limb radiance differences at selected wavelengths. This approach, which is described in a subsequent section, is applied to a subset of the CRISM observations

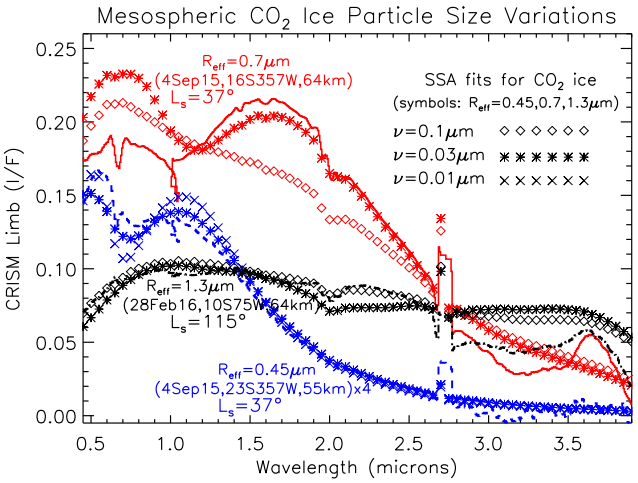

Fig. 5. CRISM observed (lines) and model fits (symbols) of limb spectral reflectance for a set of mesospheric CO_2 ice clouds, in which cloud particle sizes (R_{eff}) of 1.3 μm (28Feb2016, dash-dotted), 0.7 μm (4Sep2015 at 16S, solid), and 0.45 μm (4Sep2015 at 23S, dashed) are derived. Models for three different particle size distribution variances (V_{eff} = 0.1 for diamond symbols, 0.03 for asterisk symbols, and 0.01 for X symbols) indicate spectral interference patterns that are notable for the R_{eff} = 0.7 and 0.45 μm particle size clouds. This evidence of CO_2 cloud iridescence is less prominent in larger CO_2 cloud particle sizes as iridescence in such cases occurs at smaller scattering angles than obtained with CRISM limb observations.

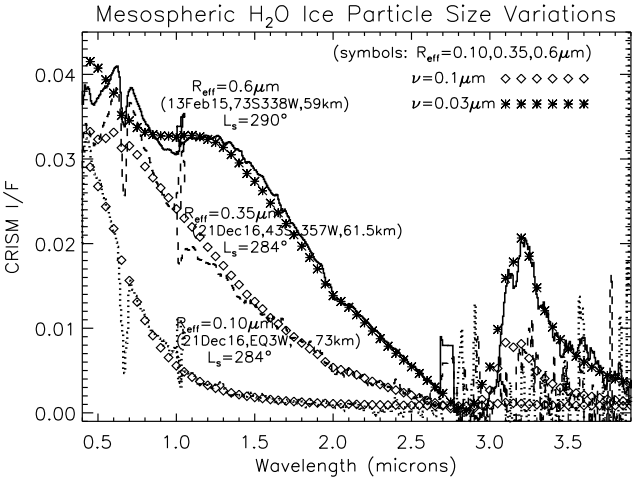

Fig. 6. CRISM observed (lines) and model fits (symbols) of limb spectral reflectance for a set of mesospheric H_2O ice clouds, in which cloud particle sizes (R_{eff}) of 0.6 μm (13Feb2015, solid), 0.35 μm (21Dec2016 at 43S, dashed), and 0.10 μm (21Dec2016 at the equator, dotted) are derived. Models for two different particle size distribution variances (V_{eff} = 0.1 for diamond symbols, 0.03 for asterisk symbols) indicate spectral interference patterns that are notable for the R_{eff} = 0.6 μm particle size case. This is the strongest case for mesospheric H_2O cloud iridescence, although the predominantly small particle sizes of mesospheric H_2O clouds presents less sensitivity in CRISM limb spectra for cloud iridescence.

selected to represent the derived range of mesospheric aerosol compositions and particle sizes. This point is mentioned above with respect to deriving limb path opacities, but it also provides a useful comparison between the visual fits of the single scattering analysis to minimization fits with multiple scattering radiative transfer.

Fig. 5 presents a set of mesospheric CO_2 cloud spectra (lines) for best-fit (symbols) particle sizes (R_{eff}) of 0.45, 0.7, and 1.3 μm. The occurrence of CO_2 cloud iridescence, not clearly present in the CO_2 limb spectra of Fig. 1, is evidenced by spectral interference (diffraction)

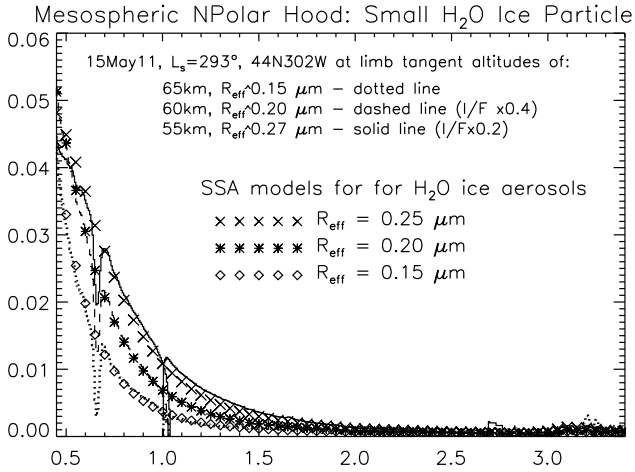

Fig. 7. CRISM observed (lines) and model fits (symbols) of mesospheric limb spectral reflectance characterizing the vertically decreasing particle sizes of H_2O ice clouds in the northern polar hood (L_s = 293°, 44N). Cloud particle sizes decrease from R_{eff} = 0.27 μm at 55 km (aeroid) to 0.15 μm at 65 km.

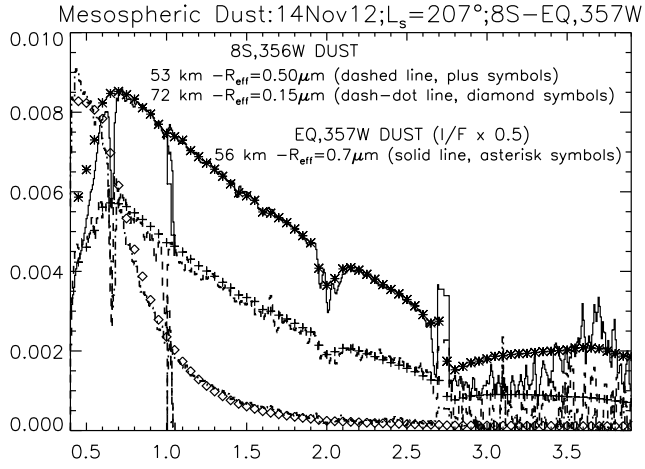

Fig. 8. CRISM observations (lines) and model fits (symbols) to limb spectral reflectances associated with a 14Nov2012 (L_s = 207°) regional storm injection of dust into the low latitude (here, 8S–equator) mesosphere of Mars. Dust particle sizes (R_{eff}) of 0.7–0.5 μm at ~55 km decrease to 0.15 μm by 70 km (aeroid) altitudes. This event constitutes the most extensive mesospheric dust aerosols detected in CRISM limb observations for the 2006–2016 period (MY29–33), during which planet encircling dust storms did not occur. MCS also observed this regional dust event (Heavens et al., 2015), suggesting the dust particle size distributions indicated in these CRISM observations reflect a considerably evolved state (see text).

patterns over λ = 0.45–2.0 μm for the two smaller ice particle size clouds provided in Fig. 5. These spectral variations are reproduced in single scattering phase function spectra with narrow particle size distributions (V_{eff} = 0.01–0.03, asterisk and X symbols), but not in broader particle size distributions (V_{eff} = 0.1, diamond symbols). This behavior is discussed in detail subsequently in a section specifically devoted to cloud iridescence.

Fig. 6 presents a set of H_2O ice scattering spectra for which derived ice particles sizes (R_{eff}) vary from 0.1 to 0.6 μm. The R_{eff} = 0.6 μm case reflects atypical conditions among the observed set of mesospheric water ice measurements, in terms of the larger ice particle size and the tentative identification of iridescence (i. e., a narrower size distribution, V_{eff} = 0.03). The full set of CRISM retrieved water ice particle sizes is dominated by R_{eff} < 0.4 μm, as presented below. While such iridescence is rarely detected (≤1%) in mesospheric H_2O versus CO_2 ice clouds, it is also true that the CRISM scattering spectra of fine (R_{eff} = 0.1–0.3 μm) H_2O ice aerosols provide less capable identification of spectral interference patterns associated with iridescence. This is due to the reduced spectral range of observed scattering for such small H_2O ice particles (particularly with small scattering angles, Fig. 3), as indicated by the smallest ice particle case in Fig. 6, and a set of similarly small H_2O ice particles presented for the north polar hood (NPH) in Fig. 7. These NPH aerosol scattering spectra indicate distinct vertical gradients in H_2O ice particle sizes (R_{eff} decreases by a factor-of-two between aeroid altitudes of 55 and 65 km), as well as the sensitivity of CRISM limb scattering spectra to small water ice particle sizes.

Fig. 8 presents a set of three CRISM limb spectra of scattering by mesospheric dust aerosols, for particle sizes (R_{eff}) ranging from 0.15 to 0.7 μm. For Mars planet encircling dust storm conditions (which did not occur over the CRISM period of limb observations), larger dust particle sizes (R_{eff} = 1–2 μm) have been observed to altitudes above 70 km (Clancy et al., 2010). Mesospheric dust aerosols over the CRISM period of limb observations are rare and their particle sizes (R_{eff}) are generally smaller than 0.7 μm. The dust aerosols presented in Fig. 8 correspond to low latitude initiation of dust lifting activity near L_s = 207° in MY31, as catalogued among high altitude dust layers in Heavens et al. (2015). At 8S, 356W (Meridiani region) and for the period of CRISM observation, this dust exhibits a sharp decrease in dust particle sizes between 53 km (R_{eff} = 0.5 μm) and 72 km (R_{eff} = 0.15 μm). These smaller dust particle sizes and their vertical gradient, in conjunction with the more spatially/temporally complete MCS observations (addressed in a later section), imply an evolved mesospheric dust size distribution rather than the initial dust size distribution injected into the mesosphere.

3.1. Sensitivity and accuracy of derived aerosol R_{eff} and composition

Sensitivity limits of the CRISM limb observations depend in part on the particle size of the scattering aerosol. As Figs. 5–8 show, smaller particle sizes lead to shortwave (0.4–0.7 μm) peaks in limb brightness, whereas larger particle sizes lead to broadwave (0.4–4.0 μm) brightness ramps. The latter case can lead to reduced aerosol sensitivity from a spectral contrast perspective. In the case of CRISM limb observations, it also conflicts with an instrumental scattering artifact of the level 0.0005 (in I/F units). This background scattering appears similar in spectral form to scattering by large (R_{eff} ~2 μm) ice or dust aerosols, extends over most latitudes of CRISM limb observations, and decreases slowly from 50 to 80 km altitudes. These latitude and altitude behaviors suggest an instrumental artifact, but its abrupt appearance in CRISM limb observations with a change in CRISM scan direction (from backward to forward with respect to the spacecraft flight direction in late 2012) is most indicative of an instrumental artifact. This artifact preferentially limits faint detections of large particle size aerosols, but an I/F limit of 0.001 in limb brightness serves as a general sensitivity limit for CRISM limb detections of mesospheric aerosol scattering.

Determinations of aerosol effective radii (R_{eff}) via the single scattering analysis yield accuracies of ~10% and precisions of order 20%. This accuracy figure refers primarily to the average difference between the SSA solutions with multiple scattering limb RT/profile retrieval determinations presented in the following section. Systematic uncertainties associated with the baseline adopted values for the particle size distribution (gamma) and dust and ice size distribution variances (apart from iridescence) can lead to similar order biases in derived R_{eff} for small particle sizes, particularly where the adopted distribution variances V_{eff} approach derived values for R_{eff}. It should also be noted that the derived R_{eff} values may reflect averaging of substantial particle size variations (i.e., distinct cloud populations) along the limb path viewing. The detection limit for small particle sizes is of order R_{eff} = 0.05 μm, in terms of R_{eff} discrimination. However, such small particle sizes lead to substantially reduced scattering brightnesses. CRISM limb spectra could in principle detect the brighter upper mesospheric R_{eff} = 0.08–0.13 μm hazes reported by Montmessin et al. (2006). However, these SPICAM stellar extinction measurements regard

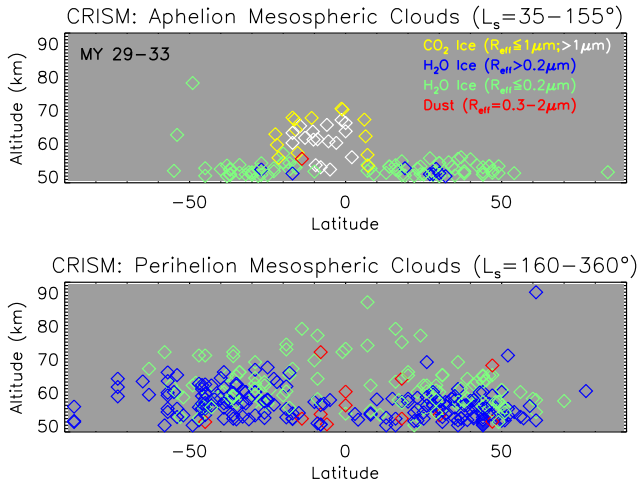

Fig. 9. The full set of mesospheric aerosol particle size (R_{eff}) and composition determinations from CRISM limb spectral reflectance profiling over 2009–2016 indicates a distinctive orbital variation in Mars mesospheric aerosol composition, particle size, and spatial distributions. During the cold aphelion portion of the Mars orbit (upper panel, reflecting the L_s = 35–155° range of CRISM limb observations), weak water ice clouds with small particle sizes (green symbols, $R_{eff} \leq 0.2$ μm) are restricted to lower mesospheric altitudes (< 55 km, aeroid) and midlatitudes. Aphelion mesospheric CO_2 ice clouds predominate low latitudes (20S–10N) at 55–75 km altitudes, with smaller cloud particle sizes (yellow symbols, $R_{eff} \leq 1$ μm) forming around the altitude/latitude boundaries of a population of larger particle size CO_2 clouds (white symbols, $R_{eff} > 1$ μm). During the warm perihelion portion of the Mars orbit (bottom panel, reflecting the L_s = 160–360° range of CRISM limb observations), H_2O ice clouds predominate with infrequent fine dust aerosols presented over the 2006–2016 period of CRISM limb observing. On average, larger H_2O cloud particle sizes (blue symbols, $R_{eff} > 0.2$ μm) occur at lower altitudes (~50–60 km). Summer polar regions exhibit relatively few mesospheric aerosols.

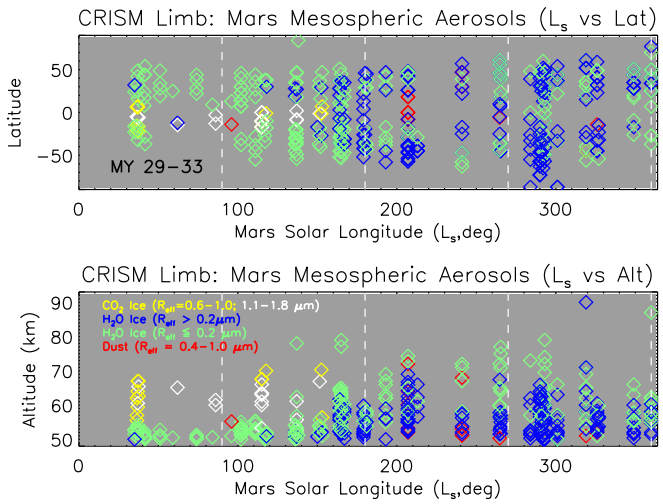

Fig. 10. The resolved seasonal (L_s) variations of CRISM retrieved mesospheric aerosol compositions and particle sizes (R_{eff}) are presented versus latitude (upper panel) and aeroid altitude (lower panel). Symbol colors characterize aerosol particle sizes and composition as indicated on the lower panel and in the Fig. 9 caption. Larger particle size mesospheric H_2O clouds (blue symbols) begin to appear after L_s = 150°. CO_2 mesospheric ice clouds (white/yellow) appear over L_s = 35–160° (CRISM limb observations are absent over the L_s = 5–30° range). Mesospheric H_2O ice clouds extend to midlatitudes (50–55NS, sun-lighted latitudes) with a variable decrease at low latitudes. Maximum mesospheric H_2O ice cloud altitudes increase somewhat abruptly from below 55 km to as high as 90 km after L_s = 140°.

nighttime conditions not accessible with CRISM limb scattering observations.

Compositional determinations, among the dust and CO_2/H_2O ice components, are accurate in an "either-or" sense with the following caveats. Roughly, 5% of identified mesospheric H_2O ice clouds, almost all of which are presented at aeroid altitudes between 50 and 55 km and at low to mid latitudes, suggest possible minor components of dust scattering. The nature of the weak dust signature in these cases is poorly defined; intimate (dust cores) or spatial (along the limb path) ice/dust mixing may account for this behavior. All of the CRISM limb views of mesospheric aerosol scattering incorporate reflected illumination from lower atmospheric dust/H_2O ice aerosols and the dust covered surface. This limits the identification of minor aerosol components, such as from nucleation cores, limb path averaging, or possible H_2O ice contamination of CO_2 ice clouds.

3.2. Derived distributions of mesospheric aerosol composition and R_{eff}

The detailed distributions of Mars mesospheric aerosol composition and particle size (R_{eff}), as characterized by the single scattering analysis of the full set of CRISM limb observations, are presented in Figs. 9–15. Fig. 9 presents the latitudinal and (aeroid) altitude distribution of dust (red symbols), CO_2 ice ($R_{eff} \leq 1$ μm, yellow symbols; $R_{eff} > 1$ μm, white symbols), and H_2O ice ($R_{eff} \leq 0.2$ μm, green symbols; $R_{eff} > 0.2$ μm, blue symbols) aerosols. The upper (L_s = 35–155°) and lower (L_s = 160–360°) panels of Fig. 9 emphasize the sharp compositional distinctions of Mars mesospheric aerosols between the cold aphelion portion of the Mars orbit and the warm perihelion portion of the Mars orbit, respectively. At the most basic level, Fig. 9 shows that H_2O ice clouds extending well into the mesosphere are restricted to the warm perihelion portion of the Mars orbit, where ~20 K increased global

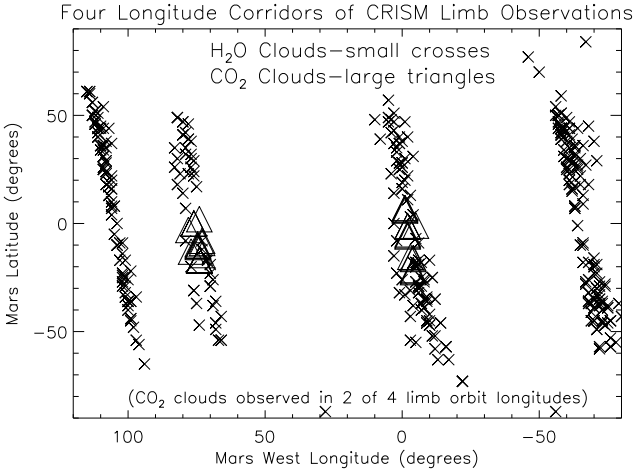

Fig. 11. CRISM limb observations were restricted in frequency (every two months on average) and number of orbits (1–3 per observational opportunity). Four Mars longitude corridors were sampled over the 2009–2016 period of limb observing, corresponding to equator crossing longitudes of ~105W, 75W, 0W, and 300W. The latitude/longitude set of mesospheric (all altitudes over 50–90 km) ice cloud detections is presented versus CO_2 ice (large triangles) and H_2O ice (small crosses) composition. As indicated in prior studies, mesospheric CO_2 ice clouds occur over specific longitudes, associated with non-migrating thermal tides (González-Galindo et al., 2011; Spiga et al., 2013). The limited longitudinal definition for mesospheric CO_2 clouds presented here is consistent with prior studies.

atmospheric temperatures are forced by ~40% increased solar flux/heating. This orbital forcing of atmospheric temperatures creates strong orbital forcing of a global hygropause level (Clancy et al., 1996), such that water vapor abundances above 50 km are reduced by 2 orders of magnitude over the aphelion versus perihelion periods, as exhibited in observations (Clancy et al., 2017) and models (Millour et al., 2014). The restriction of aphelion mesospheric water ice aerosols to below

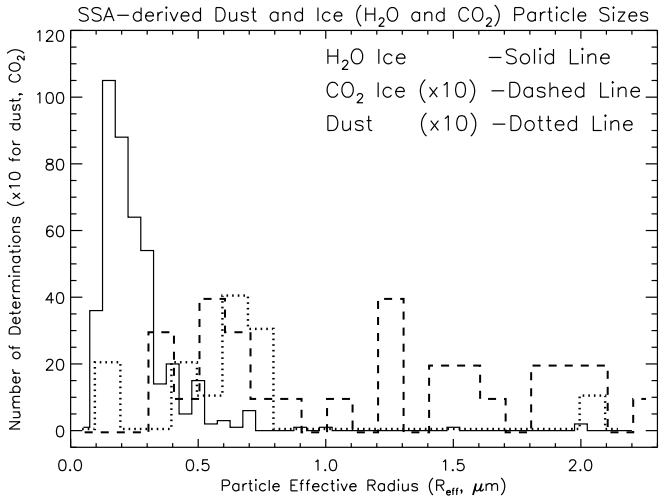

Fig. 12. The distributions of mesospheric aerosol particle size (R_{eff}) measurements are presented for dust (dotted line, binsize = 0.1 μm), H_2O ice (solid line, binsize = 0.05 μm), and CO_2 ice (dashed line, binsize = 0.1 μm). Notice that the measurement numbers for the less frequently observed dust and CO_2 aerosols have been scaled by a factor of 10. Mesospheric H_2O ice cloud particles are narrowly distributed at small R_{eff} (0.1–0.3 μm). Mesospheric CO_2 ice cloud particles are broadly distributed over larger R_{eff} (0.3–2.3 μm). Mesospheric dust cloud particles for this non-planet encircling dust storm era are distinctly smaller than observed during the 2001 planet encircling dust storm (Clancy et al., 2010).

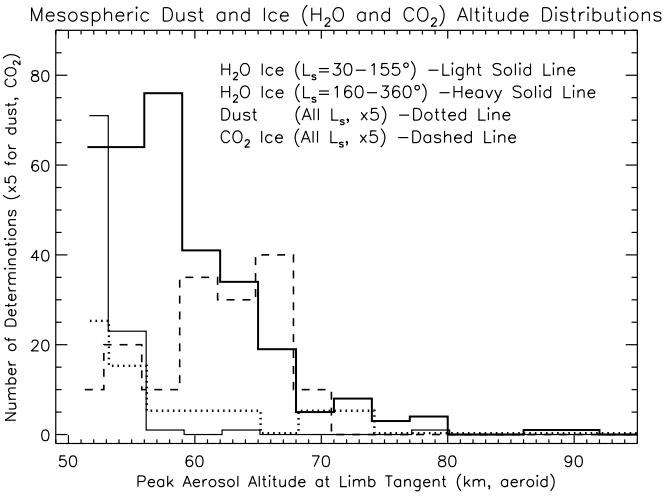

Fig. 13. The distributions of observed mesospheric aerosol altitudes are presented for dust (dotted line), H_2O ice (light solid line, L_s = 30–155°; heavy solid line, L_s = 160–360°), and CO_2 ice (dashed line). The dust and CO_2 ice numbers are scaled by ×5 to emphasize the relative altitudes among the aerosols. These are minimum actual altitudes, assuming that the observed aerosol layers peak at the limb tangent. Mesospheric CO_2 cloud altitudes of 60–65 km are most common, whereas mesospheric H_2O cloud altitudes are very seasonal, reaching as high as 90 km in the late perihelion season. Aerosols are not detected in CRISM limb observations above this level.

55 km and with small particle sizes presumably reflects this water vapor abundance decline, given that atmospheric temperatures are ~20 K colder in this season.

The top panel of Fig. 9 also displays the latitude/altitude distribution of aphelion mesospheric CO_2 ice clouds (white and yellow symbols) resulting from the globally cold aphelion atmosphere and more specifically, low latitude minimum temperatures associated with solar tides and gravity waves (Clancy and Sandor, 1998; Listowski et al., 2014; Spiga et al., 2012; Yiğit et al., 2015). Several other key aspects

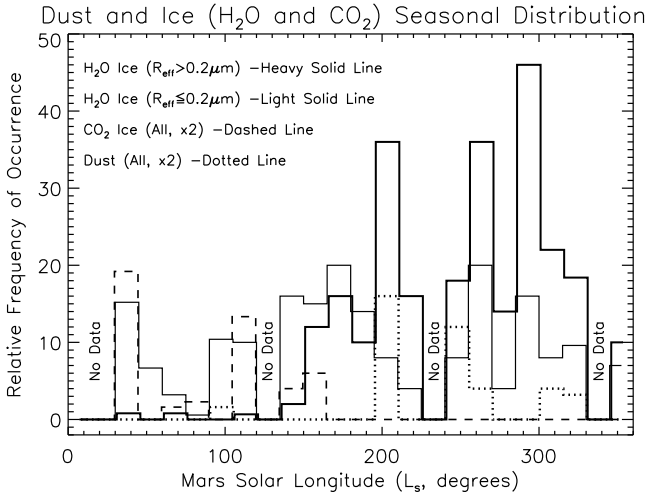

Fig. 14. The number of mesospheric aerosol detections versus Mars season (L_s, 15° bins) is distinguished by H_2O ice (heavy solid line, R_{eff} > 0.2 μm; light solid line, R_{eff} ≤ 0.2 μm), CO_2 ice (dashed line), and dust (dotted line) compositions. L_s periods lacking CRISM limb observations are indicated. The numbers for dust and CO_2 ice detections have been scaled ×2 to emphasize the relative L_s variations among the aerosol types.

regarding CRISM measurements of mesospheric CO_2 cloud distributions are: 1) 20S–10N latitudes of occurrence, 2) peak projected altitudes of 70–75 km, and 3) smaller CO_2 particles sizes (yellow symbols, R_{eff} ≤ 1 μm) at the latitude/altitude margins of CO_2 cloud occurrence.

Fig. 9 also emphasizes the very limited occurrence of mesospheric dust during the 2009–2016 period of CRISM limb observations, which falls between the planet encircling dust storm years of 2007 (MY28) and 2018 (MY34). The majority of perihelion period (lower panel of Fig. 9) occurrences of mesospheric dust loading are associated with dust events in 2012 (MY31) at low latitudes (L_s = 207°) and at northern midlatitudes (L_s = 241°). There is one curious aphelion mesospheric dust occurrence at L_s = 96°, which is discussed in a later section.

Fig. 10 presents the detailed seasonal (L_s) variations in Mars mesospheric aerosols and CRISM limb observational coverage versus latitude (upper panel) and altitude (lower panel). Significant L_s gaps in CRISM limb coverage are present over L_s = 5–30° (most important with respect to mesospheric CO_2 clouds) and several narrower L_s gaps distributed over L_s = 220–340°. The latitudinal distribution of mesospheric aerosols displayed in the upper panel of Fig. 10 is fairly uniform over low-to-mid latitudes (50S–50N) with the exceptions of a gap in 50S–30N aerosols centered around aphelion (L_s = 70° ± 20°) and a more variable gap in low latitude (20S–20N) ice aerosols over L_s = 200–360°. Illuminated high latitude regions (latitudes 60° in later spring/summer/early spring seasons) exhibit few mesospheric aerosols, with the exception of occasional bright H_2O cloud layers presented at the summer poles around 50 km altitudes. As discussed for Fig. 9, larger H_2O ice particle sizes (R_{eff} > 0.2 μm) are largely confined to the perihelion period (L_s > 160°).

The altitude/L_s distributions of CRISM mesospheric aerosol measurements are presented in the lower panel of Fig. 10, which reflects the CRISM coverage gaps and the L_s variation of larger H_2O ice particle sizes (R_{eff} > 0.2 μm) as discussed for the upper panel of Fig. 10. Mesospheric H_2O ice clouds exhibit vertical confinement below 55 km (aeroid) altitudes centered over the aphelion season (L_s = 30–140°). They extend to > 70 km altitudes centered over the perihelion season (L_s = 180–340°), with smaller particle sizes (R_{eff} ≤ 0.2 μm) more prominent at the higher altitudes (> 60 km). Mesospheric ice aerosols extend as high as 90 km, but are primarily limited to altitudes below 75 km (aeroid). Altitudes above 95–100 km show no evidence of aerosol scattering, with top altitudes of measurement varying with latitude from 120 km at southern high latitudes to > 160 km at northern high

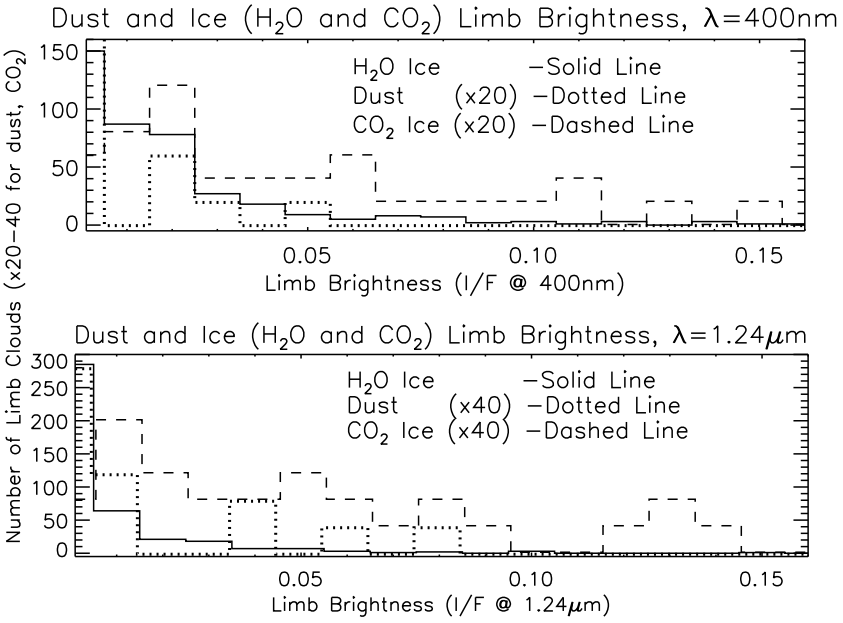

Fig. 15. The observed distributions of limb brightness (I/F) at λ = 0.4 μm (upper panel) and 1.24 μm (lower panel), as distinguished by aerosol composition. The numbers of dust (dotted line) and CO_2 (dashed line) aerosol I/F measurements are scaled by ×20/×40 (upper/lower panel) for convenience of comparison, to highlight the brighter, larger particle size (on average) characteristics of CO_2 clouds.

latitudes. Low latitude mesospheric CO_2 ice clouds are observed over L_s = 35–155° to as high as 75 km altitudes. The key L_s = 5–30° period, which is not covered in the CRISM limb data set, is also a prominent season for such CO_2 clouds as characterized in previous studies (Clancy et al., 2007; Määttänen et al., 2010; Montmessin et al., 2007; Vincendon et al., 2011).

The (W) longitude/latitude distributions of mesospheric CO_2 ice clouds incorporated in CRISM limb views are plotted in Fig. 11, which also indicates the limited longitudinal distribution of CRISM limb observations. Four distinct longitudes of the MRO orbit characterize the CRISM limb data set, two of which obtained mesospheric CO_2 ice clouds (large triangle symbols). These longitudes (~75W and 0W) agree with results of prior studies regarding the distinct longitudinal distributions for mesospheric CO_2 ice clouds (Clancy et al., 2007; Määttänen et al., 2010; Montmessin et al., 2007; Vincendon et al., 2011), which correspond to surface influences on non-migrating thermal tides (González-Galindo et al., 2011) and thermal tide influences on mesospheric gravity wave forcing (Spiga et al., 2012; Yiğit et al., 2015). Fig. 11 (and Figs. 9 and 10) shows much weaker longitude/latitude influences on mesospheric water ice clouds (small cross symbols), with the exception of reduced occurrence frequencies at low latitudes and higher latitudes for such water ice clouds during the perihelion period.

Fig. 12 presents the specific particle size ranges (number of determinations versus derived R_{eff}) as retrieved for dust (dotted line, ×10), CO_2 ice (dashed line, ×10), and H_2O ice (solid line). The factor-of-ten scaling for the number of dust and CO_2 ice determinations simply reflects the smaller number of such aerosol detections and the need to display all three aerosol populations on the same vertical scale. The 2× finer size (R_{eff}) bin employed for mesospheric H_2O ice also reflects the greater number of such measurements, which supports a finer characterization of the detailed distribution of mesospheric H_2O ice particle sizes. The most striking aspect of this figure are the very different particle size ranges exhibited for mesospheric H_2O and CO_2 ice clouds. Mesospheric H_2O ice particle sizes are very strongly peaked near R_{eff} = 0.2 μm, whereas mesospheric CO_2 ice particle sizes exhibit essentially an even distribution of R_{eff} from 0.3 to 2.3 μm. This dichotomy between mesospheric H_2O and CO_2 ice particle size variations presumably reflects a distinction in trace versus bulk constituent cloud microphysics. Mesospheric dust aerosols also exhibit a relatively narrow range of small particle sizes (R_{eff} = 0.2–0.7 μm, with one exception discussed subsequently) in these non-planet-encircling dust storm years. All three mesospheric aerosol populations show little evidence of a small particle size continuum. For example, mesospheric H_2O aerosol measurements (with the best measurement statistics) exhibit a distinct decrease in detections for $R_{eff} \leq$ 0.1 μm. This does not preclude a significantly bimodal particle size distribution associated with a distinct population of very fine ($R_{eff} \leq$ 0.05 μm) ice aerosols, as proposed by Fedorova et al. (2014). The CRISM wavelength range would not discriminate such fine aerosols against the scattering of larger (brighter) particle size aerosols.

Fig. 13 presents the aeroid altitude distribution of CRISM measurements for mesospheric dust (dotted line, ×5), CO_2 ice (dashed line, ×5), and H_2O ice (thin solid line — L_s = 30–155°, thick solid line, L_s = 160–360°). Once again, these are projected altitude distributions at the limb tangent point, aerosols viewed in the fore or background of the limb tangent point will have their true altitudes underestimated (typically by as much as 5 km). As also illustrated in Figs. 9 and 10, mesospheric H_2O ice clouds during the earlier (aphelion) period are primarily confined to altitudes below 55 km, whereas perihelion-period mesospheric H_2O ice clouds extend to higher altitudes (typically 55–70 km, but up to 90 km). Mesospheric dust, which is observed only in the perihelion season apart from a single aphelion case (also called out for a large particle size above), is observed at altitudes typically below 55 km. Whereas there is a tendency for mesospheric H_2O and dust aerosol occurrences and particle sizes (Figs. 6–10) to decrease with altitude, mesospheric CO_2 cloud altitudes tend to cluster over 60–70 km aeroid altitudes. Nevertheless, there do appear to be CO_2 clouds below this level, as also suggested by "loop" cloud measurements from MCS in this aphelion season (Fig. 9 of Sefton-Nash et al., 2013). It is also important to note that CRISM limb observations were not obtained over the peak season (L_s = 10–30°) of mesospheric CO_2 cloud occurrence (Fig. 8 of Vincendon et al., 2011, Fig. 6 of Sefton-Nash et al., 2013), due to unfortunate timing with MRO safing and CRISM instrument cooling issues. It is likely that mesospheric CO_2 cloud altitudes vary with L_s, as changes in the mesospheric temperatures over this L_s range are significant in terms of the vertical phasing of mesospheric thermal tides (Millour et al., 2014). Peak CO_2 cloud altitudes (~80 km) over L_s = 10–30° are suggested in MCS "loop" cloud peak altitudes (Fig. 9 of Sefton-Nash et al., 2013) and in HRSC cloud altitude determinations (Fig. 11b of Määttänen et al., 2010).

Such seasonal changes in mesospheric thermal structure appear less likely to explain a distinct pause in mesospheric CO_2 cloud formation over L_s ~50–90° that is exhibited in the current and prior L_s characterizations of such clouds (Clancy et al., 2007; Montmessin et al.,

2007; Vincendon et al., 2011). Fig. 14 presents the orbital/seasonal evolution of the relative frequency for observed mesospheric aerosols as separated by composition (H_2O ice — solid lines, CO_2 ice — dashed line, dust — dotted line) and particle size (H_2O ice only: $R_{eff} \leq 0.2\,\mu m$ — light solid line; $R_{eff} > 0.2\,\mu m$ — heavy solid line). The observed frequencies are approximately normalized by the number of CRISM orbits obtained in each L_s bin of 15°, and dust and CO_2 ice populations are further scaled by a factor-of-two for presentation purposes. The seasonal coverage of CRISM limb observations is far from uniform, with four distinct L_s coverage gaps noted on Fig. 14. Nevertheless, several broad conclusions can be drawn. Mesospheric dust and larger particle size H_2O ice aerosols are primarily confined to perihelion solar longitudes ($L_s \geq 150°$). Both CO_2 and fine H_2O ice clouds appear over aphelion solar longitudes ($L_s \leq 160°$), and both exhibit the $L_s \sim 50-90°$ decreases mentioned above for mesospheric CO_2 clouds. LMD MCD simulations exhibit distinct minima in mesospheric water vapor and water ice aerosols over this L_s range relative to preceding and following L_s ranges (0–40°, 100–140°, Millour et al., 2014). LMD MCD mesospheric temperatures over the $L_s \sim 50-90°$ range exhibit a vertical shift in mesospheric thermal tides, as indicated above, with ~10 K warmer temperatures below ~60 km and ~10 K colder temperatures above 60 km. These temperature profile variations are not obviously related to the notable decrease in mesospheric CO_2 and H_2O cloud formation over this period. The observed and modeled decreases in fine water ice aerosols appear related to aphelion minimum altitude hygropause conditions below 40 km altitudes. Perhaps a related reduction in condensation nuclei (CN) extending into the mesosphere leads to the observed suppression of mesospheric CO_2 clouds over this aphelion L_s period. The nucleation of mesospheric CO_2 clouds remains poorly understood even though it constitutes the primary limitation in simulating mesospheric CO_2 clouds (Listowski et al., 2014). This critical uncertainty is discussed in more detail subsequently.

Fig. 15 presents the distribution of aerosol limb brightness (I/F units) at wavelengths of 0.4 and 1.25 μm (upper and lower panels), as distinguished among the dust (dotted lines) and ice (CO_2 — dashed lines; H_2O — solid lines) mesospheric aerosols. The dust and CO_2 numbers (vertical scales) are scaled by ×20 (upper panel, $\lambda = 0.4\,\mu m$) and by ×40 (lower panel, $\lambda = 1.25\,\mu m$) for presentation purposes. For the most part, the limb I/F of mesospheric H_2O ice clouds fall below 0.05 for $\lambda = 0.4\,\mu m$, and below 0.02 for $\lambda = 1.25\,\mu m$. Dust and particularly CO_2 ice aerosol layers exhibit a much broader range of limb brightnesses. Mesospheric CO_2 clouds are intrinsically brighter on average and in peak brightnesses than mesospheric H_2O clouds. Individual limb brightnesses characterized in Fig. 15 reflect the opacity of mesospheric aerosol layer as integrated along the limb path of observation, the scattering angle of observation, and the aerosol particle size (through the aerosol scattering properties). The scattering angle of observation varies widely for mesospheric H_2O clouds (θ = 30–150°) as they are exhibited over a wide range of latitudes. Conversely, the scattering angles for mesospheric CO_2 clouds vary over a more restricted range (θ = 50–80°) due to their confinement to low latitudes (Figs. 9–11). Hence, the broader I/F range of mesospheric CO_2 versus H_2O ice clouds reflects a broader range of intrinsic brightnesses (opacities) and particle sizes (Fig. 12).

4. Radiative transfer fits for aerosol composition, opacity, and particle size (R_{eff})

The single scattering analysis of the preceding chapter lacks a quantitative approach to defining mesospheric aerosol opacities. In the following section, a profile retrieval analysis for mesospheric aerosol composition, particle size, and opacity employing multiple scattering radiative transfer (RT) with spherical shell geometry is extended for mesospheric analysis by co-author Smith for this purpose. These retrievals provide both a comparison to the above single scattering solutions for composition and R_{eff} employing a more standard profile retrieval analysis, and a measure of mesospheric number densities based the simultaneous retrieval of particle size and opacity. This analysis is numerically intense and requires considerable individual data processing. Hence a much smaller (~10%) but representative set of CRISM limb observations are analyzed in this fashion.

The RT profile retrievals adopt the numerical approaches developed for CRISM limb aerosol retrievals by Smith et al. (2013), and also applied to profile retrievals for Mars water vapor (Smith et al., 2011) and O_2 airglow (Clancy et al., 2017). The key elements are a pseudo-spherical multiple scattering code based upon the discrete ordinates method (Stamnes et al., 1988) and vertical profile retrieval based upon the non-linear Levenberg-Marquardt algorithm (Press et al., 1992). The pseudo-spherical limb RT generates a plane parallel multiple scattering radiation field that is integrated along spherical limb paths, which is shown to agree with full spherical RT simulations to within a few percent (Smith et al., 2013). Scattering and thermal emission are included in the RT, including the effects of aerosol scattering from surface reflectance and thermal emitted radiances. Selected wavelengths for RT calculation and profile retrieval weighting incorporate 12 wavelengths spanning 0.74 to 3.7 μm. Although this wavelength range does not encompass 0.4–0.7 μm wavelengths fit with the single scattering analysis, it does in fact characterize smaller aerosol particle sizes (R_{eff} = 0.2–0.4 μm) reasonably well due to the diagnostic leverage over the 0.7–1.0 μm wavelength range. Gaseous CO_2 and H_2O absorption is avoided in the selection of the modeled wavelengths, which are designed to maximize dust and ice (CO_2 and H_2O) aerosol discrimination.

Dust, H_2O and CO_2 ice optical indices are identical to those adopted for the single scattering analysis. However, Mie phase functions are employed, in conjunction with these optical indices, to calculate aerosol scattering and absorption properties for the H_2O and CO_2 ice cloud particles (whereas the dust particle scattering properties follow the same shape/phase functions employed in the SSA analysis). As indicated in Fig. 4, the phase function wavelength dependences for spheres versus cylinders are not substantially different in terms of defining aerosol particle sizes from CRISM limb spectra. Aerosol particle size distribution functions are defined by gamma distributions with fixed particle size distribution variances (V_{eff} = 0.3 for dust, 0.1 for ice), as is the case for the single scattering analysis with the exception of modeling CO_2 cloud iridescence. As in Smith et al. (2013), the RT employs 50 vertical layers over 0–80 km, and 32 terms in the Legendre polynomial expansion for the angular distribution of the radiation field. The non-linear iterative profile retrieval algorithm searches for best fit solutions to opacity and effective particle sizes (R_{eff}) versus altitude from the surface to 80 km.

The retrievals are designed to either assume a single component aerosol composition or fit for a two component composition, such as dust and H_2O ice or CO_2 and H_2O ice. While dust and H_2O ice aerosols are commonly found in association in the lower Mars atmosphere (e. g., dust vertically capped by H_2O ice, McCleese et al., 2010; Smith et al., 2013), mesospheric dust is rare over non-planet encircling dust storm years and H_2O and CO_2 ice aerosols are spatially and seasonally segregated by their distinct condensation temperatures. As discussed earlier, reflected illumination from surface dust and lower atmospheric dust and H_2O ice aerosols limits the capability of CRISM limb spectra to constrain minor mixing components of mesospheric aerosols. Analysis of an isolated December 2013 (L_s = 62°, 65 km, 15S, 73W) CO_2 cloud in terms fractional CO_2 and H_2O composition provides only an upper limit of ~20% for H_2O ice fraction. Furthermore, the limb observing geometry does not specify whether this upper limit applies to intimate (condensation core) or spatial (along the limb path) mixing.

The retrieved opacity, R_{eff} profiles exhibit altitude-to-altitude oscillations on the ~1.5 km vertical resolution of the retrievals, contributed by retrieval correlations between these aerosol parameters and the limited signal-to-noise ratios at wavelengths beyond 2 μm (particularly for weak or small particle size limb aerosols). The more spatially discrete character of Mars mesospheric aerosols in comparison to lower

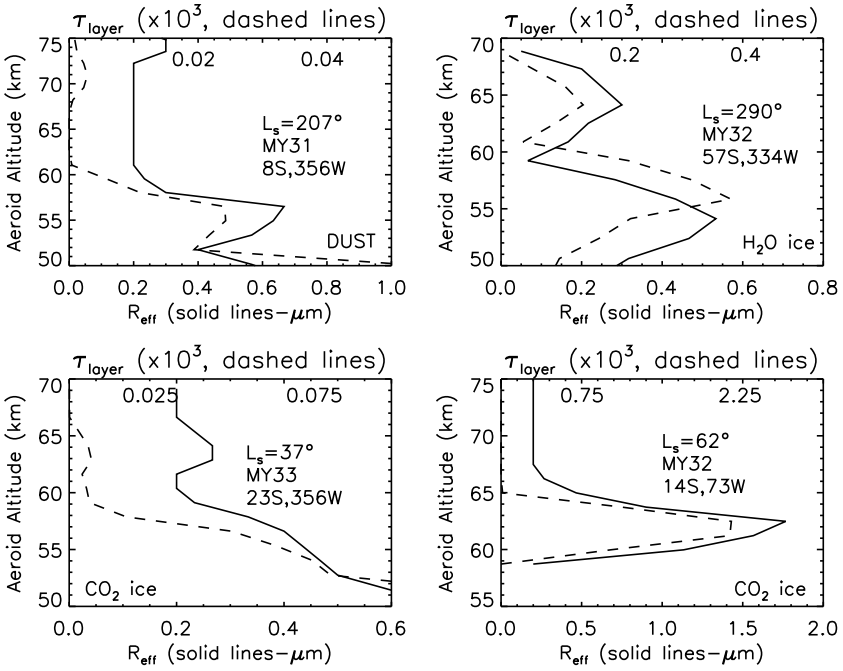

Fig. 16. A set of aerosol optical depth (dashed lines with upper scales) and particle sizes (R_{eff} in μm, solid lines with lower scales) profiles are retrieved employing multiple scattering, pseudo-spherical limb radiative transfer and the non-linear Levenberg-Marquardt inversion algorithm (Smith et al., 2011). These solutions also obtain aerosol composition among dust (upper left panel), H_2O ice (upper right panel), and CO_2 ice (lower panels). The presented optical depths refer to normal optical depth (referenced to λ = 2.219 μm, as in Smith et al., 2013) for retrieved ~1.5 km layers, although both the plotted R_{eff} and τ profiles are smoothed by running 3-layer averaging to reduce profile oscillations present in the retrievals. Average R_{eff} and τ retrieval uncertainties are ~20%. However, these are spherical shell solutions such that discrete cloud layer optical depths will scale as the ratio of the spherical path (~300 km) to the actual cloud horizontal extent.

atmospheric dust and H_2O aerosols contributes additional profile noise. The horizontal discreteness of mesospheric aerosols is indicated in nadir imaging, in MCS "loop" scan structure, and in the sharp decreases in CRISM limb brightnesses below the peak brightness altitude. It is also expected for mesospheric clouds in their predicted association with gravity wave forcing. The spherical shell RT model cannot reproduce the sharp decrease in limb brightness below such discrete scattering layers (e. g., Clancy et al., 2007), and this adds to the oscillatory vertical variations in retrieved opacity and R_{eff} profiles. To reduce noise associated with vertical profile oscillations resulting from both sources, we apply 3-layer vertical smoothing to the retrieved opacity and R_{eff} profiles. Average uncertainties for these vertically smoothed optical depth (referenced to λ = 2.2 μm) and R_{eff} profiles are ~20%, although there is considerable variation in the quality of fit among the ~30 CRISM mesospheric aerosol profile retrievals performed.

Fig. 16 presents a set of four retrieved profiles, smoothed to 4–5 km vertical resolution, including mesospheric aerosols for dust (upper left), H_2O ice (upper right) and CO_2 ice (lower panels) compositions. The dashed lines provide layer optical depths (upper scale for 1.5 km layers, $\tau_{\lambda=2.2\ \mu m}$ scaled by 10^3), the solid lines provide cloud particle effective sizes (lower scales for R_{eff} in μm). The presented optical depths refer to cloud/aerosols extended uniformly over spherical shells, which is to say with horizontal scales of order 300 km. As we argue below, mesospheric ice clouds are more horizontally confined such that considerably higher (e. g., 5–10×) cloud opacities pertain to the discrete mesospheric clouds sampled in the CRISM limb views.

Generally, retrieved mesospheric aerosol opacities yield minimal vertical optical depths ($\tau_{nadir} \leq 0.001$). However, the brightest CO_2 ice clouds, in particular, present vertical optical depths of order several tenths, as apparent in OMEGA, THEMIS, CRISM, and MARCI nadir imaging of mesospheric CO_2 ice clouds. For example, the CO_2 cloud presented in the lower right panel of Fig. 16 corresponds to a vertical optical depth of ~0.05, if it is assumed to extend over ~30 km horizontal scales.

Fig. 17 presents a comparison of RT/profile retrieved R_{eff} to R_{eff} best fit with the single scattering analysis, for ~40 specific mesospheric aerosol layers as selected for a variety of aerosol compositions, R_{eff}, and peak limb brightnesses. The vertical axis indicates the RT/profile retrieved R_{eff} and the horizontal axis indicates the % difference between this R_{eff} and the R_{eff} returned with the single scattering analysis. Aerosol

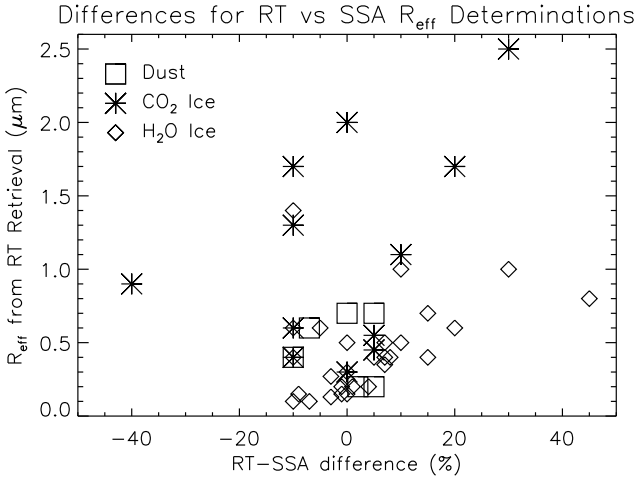

Fig. 17. Comparison of Mars mesospheric aerosol particle sizes (R_{eff}) as derived from the single scattering approximation (SSA — e. g., Fig. 12) to the reduced set of true profile retrieval solutions (RT — e. g., Fig. 16). The difference in R_{eff} between the two approaches (in %) is presented versus the RT derived R_{eff}. Dust, CO_2 ice, and H_2O ice aerosol compositions for each R_{eff} solution are denoted by square, asterisk and diamond symbols, respectively. Overall, R_{eff} solutions for the two approaches are observed to agree within ± 15% with perhaps somewhat larger differences for $R_{eff} \geq 1$ μm.

composition is denoted by distinct symbols (squares — dust, asterisks — CO_2 ice, diamonds — H_2O ice). Fig. 17 indicates that the two distinct methods of aerosol particle size determination provide agreement within, generally, ± 15%, although with differences as high as 40% for roughly 10% of the comparisons. These increased differences between the techniques are most prominent for particle sizes with R_{eff} ~1 μm, although this effect may simply be a consequence of the statistics of small numbers. Overall, the simplified RT and single layer limitations of the single scattering analysis do not impart significant average errors in retrieved R_{eff} for mesospheric aerosol layers.

4.1. Estimated aerosol number densities and implications for condensation nuclei densities

The RT/profile retrieval solutions for R_{eff} and opacity further support an assessment of particle number densities for mesospheric aerosol layers, with the assumption of average horizontal extents for these aerosol layers. The retrieved aerosol opacity refers to a uniform spherical shell, or roughly a horizontally projected 300 km limb scattering path. The actual spatial filling of this limb path by mesospheric clouds will be variable and depend both on individual mesospheric cloud scales and their multiplicity along the limb path. These parameters are best known from nadir imaging of mesospheric CO_2, and to a lesser extent H_2O, ice clouds from THEMIS (McConnochie et al., 2010), HRSC and OMEGA (Määttänen et al., 2010; Montmessin et al., 2007; Scholten et al., 2010), and CRISM (Vincendon et al., 2011) nadir imaging observations. In a following section, we add MARCI images to this list. Generally, mesospheric CO_2 clouds appear as cirrus-like filamentary structures with spatial dimensions of order 10 × 100 km and with wave-like patterns of multiplicity. Individual clouds are preferentially oriented east-to-west with wavelike periodicities often extending north and southward over 100–300 km scales. Mesospheric H_2O ice cloud forms are less constrained, they appear to extend over similar spatial scales but perhaps with less filamentary, more "clumpy" morphologies (Vincendon et al., 2011).

The CRISM limb views are north–south along the MRO orbit plane, such that they preferentially intersect the short axis of the filamentary mesospheric CO_2 clouds. However, the wave-train character of these clouds in the north-south direction will lead, on average, to multiple clouds incorporated in CRISM limb views. To obtain a coarse estimate of cloud particle number densities, we assume that retrieved limb optical depths correspond to 20% filling by mesospheric CO_2 or H_2O clouds. Hence, we scale retrieved ice opacities by a constant factor of 5. Mesospheric dust aerosols are not obviously characterized by such spatial variations such that we do not scale dust opacities by this factor. Clearly, a fixed scaling factor for mesospheric cloud filling does not account for the variable cloud sampling obtained among the CRISM limb observations, and so will contribute an effective noise to the derived distribution of mesospheric aerosol number densities. Furthermore, uncertainty in the estimated average limb path filling factor likely contributes ~50% uncertainties to estimated average cloud particle number densities. Nevertheless, these estimated particle number densities prove interesting in their magnitude and dependence with particle size (R_{eff}).

Fig. 18 presents these estimated particle number densities versus derived particle size (R_{eff}), where dust and CO_2/H_2O ice aerosols are distinguished by separate symbols. Determination of these particle number densities employs extinction cross sections calculated at the 2.22 μm wavelength of the retrieved limb opacities, as a function of the derived aerosol composition and R_{eff}, and for gamma particle size distributions with V_{eff} = 0.1. The primary source of error in the resulting particle number densities arises from the adoption of a constant aerosol filling factor along the limb optical path, which likely contributes of order −50%, +100% noise in the individual particle number densities presented in Fig. 18.

A range of particles number densities from 0.01 to 30 cm^{-3} exhibits a distinct inverse relationship with particle size (R_{eff}). In particular, average mesospheric H_2O ice and dust aerosol number densities scale with R_{eff} similarly to a constant aerosol mass dependence (dashed line). This behavior is notably less evident for estimated mesospheric CO_2 cloud particle number densities. This behavior may be influenced by observational biases including the fact that small aerosol particle sizes require larger number densities for detection. Smaller aerosol particle sizes may also imply hazes that lead to more extended horizontal scales (i. e., the 5× scaling factor overestimates their number densities or, alternatively, underestimates the compactness of clouds with larger particle sizes).

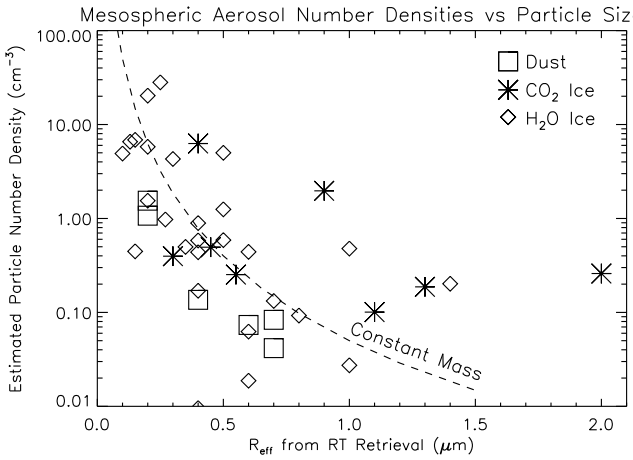

Fig. 18. Estimated aerosol particle number densities (cm^{-3}) are derived from the set of limb RT retrievals for aerosol composition, R_{eff}, and optical depth (Figs. 16 and 17). These are plotted against the RT retrieved R_{eff} values and distinguished in composition by symbols as indicated. In all cases, peak optical depths are selected from the RT profile retrievals, and these peak optical depths have been scaled by ×5 for the CO_2 and H_2O ice aerosols only, as an estimated average correction for their discrete horizontal extents. The dashed line curve provides a reference to the number density/particle size dependence for a constant aerosol mass.

Alternatively, a constant mass behavior for mesospheric H_2O ice aerosols could indicate that these mesospheric clouds incorporate, on average, a fixed proportion of available mesospheric water vapor independent of microphysical processes that affect their particle sizes, such as condensation nuclei (CN) number densities. If we assume the average altitude of ~60 km for the set of H_2O ice clouds represented in Fig. 18 and an average particle number density of 1 cm^{-3}, the implied water mass density is roughly equivalent to 15% of the LMD MCD water vapor abundance at this altitude over the perihelion season. The LMD MCD simulated water ice mass is similarly ~10% of the simulated LMD MCD water vapor abundance. However, the LMD MCD simulated water ice particle sizes at this altitude level are both very large (R_{eff} = 2–4 μm) and confined to low latitudes. These behaviors conflict sharply with the mid-latitude and small particle size characteristics determined from CRISM limb observations of mesospheric H_2O ice clouds.

A key limitation in modeling Mars mesospheric ice aerosols regards uncertain sources and number densities for mesospheric condensation nuclei (CN). This problem is most fully described in the analysis of mesospheric CO_2 ice clouds (Listowski et al., 2014), but applies equally to mesospheric H_2O ice clouds. Fine (R_{eff} = 0.2–0.3 μm) dust particles, which presumably are related to CN for water ice nucleation in the LMD MCD, are similar in size to those retrieved for 60 km altitudes in the CRISM limb observations. The LMD MCD number densities for these dust populations are ~0.01 cm^{-3}, as compared to ~1 cm^{-3} number densities estimated from 60 km CRISM limb observations for dust and H_2O aerosols in this particle size range. This difference in dust particle number densities at least partly reflects the atypical dust opacities represented in the CRISM dust profile retrievals, which correspond to relatively rare CRISM dust measurements in the mesosphere. However, the H_2O particle size and number density values are typical of the Mars perihelion mesosphere. Consequently, the large mesospheric H_2O ice particle sizes simulated in the LMD MCD may reflect a related paucity in the model CN dust number density as the CRISM and LMD MCD water mass contents of mesospheric H_2O aerosols are similar. Along these lines, it is tempting to argue that the "constant mass" curve in Fig. 18 reflects a variation in available mesospheric CN.

Listowski et al. (2014) show small CN number densities in the LMD MCD model lead to similar (two orders of magnitude) under predictions

in mesospheric CO_2 ice cloud opacities. The number densities of H_2O mesospheric aerosols presented in Fig. 18, as indicative of available CN, could support increased model simulated opacities for mesospheric CO_2 ice clouds. However, these dust and H_2O aerosol sizes and densities do not extend to the aphelion season of mesospheric CO_2 cloud occurrence (Figs. 9, 10, and 14). Much smaller dust or H_2O ice CN particle sizes, not detectable with CRISM limb spectra ($R_{eff} < 0.1$ μm), would be required to explain the observed mesospheric CO_2 cloud number densities of order 1 cm^{-3}. Most recently, clusters of water molecules on metal ions have been proposed as abundant mesospheric CN, based on MAVEN (Mars Atmosphere and Volatile Environment) orbiter observations of Mg^+ ions near 90 km altitudes (Plane et al., 2018). Another factor may be a distinct population of very fine dust particles (such as for the bimodal distribution identified by Fedorova et al., 2014), which has been considered in Mars GCM microphysical simulations of lower atmospheric H_2O clouds (Shaposhnikov et al., 2018).

All of these arguments remain poorly constrained, but the widespread occurrence of H_2O and CO_2 ice clouds in the Mars mesosphere is clear evidence that CN densities are significantly more abundant than current modeling studies have managed to reproduce. As developed below, the extensive occurrence of these clouds with large observed (relative to modeled) particle number densities implies efficient heterogeneous nucleation within minimum temperature perturbations associated with gravity waves and thermal tides in the Mars mesosphere. We return to the subject of mesospheric CN in subsequent discussion of CO_2 cloud iridescence.

5. Mesospheric cloud images

Two sets of mesospheric cloud images are presented here, regarding the CRISM limb observations and coincident MARCI nadir daily global imaging. The CRISM limb images are the spectral/spatial limb scan data from which the limb scan spectra are derived, with spatial averaging along the limb, to support the above aerosol analyses. This imaging resolution of order 0.5 km along the limb orthogonal to the limb fov extends roughly 30 km in Mars longitude. Because of several hundred kilometer optical paths along the limb fov and the longitudinal extent of mesospheric clouds, CRISM limb imaging generally reveals modest spatial variations in cloud brightness along the atmospheric limb over the ~30 km horizontal scales imaged. While this spatial resolution is not emphasized in the previous analysis, it does provide a limited opportunity to detect horizontal (longitudinal) variations in aerosol particle sizes.

MARCI nadir imaging can provide a more diagnostic characterization of the horizontal scales and extents of Mars mesospheric aerosols, to the degree they are bright enough to be seen in the nadir and their mesospheric altitudes are defined by (visible) color separation associated with parallax between the offset filter images of MARCI wide angle observing (Bell et al., 2009). In practice, this limits such mesospheric cloud detections to the brighter CO_2 clouds above reduced cloud and dust loading in the lower atmosphere. Nevertheless, this provides a rare opportunity to complement the mesospheric aerosol properties revealed in CRISM limb views with near-simultaneous descriptions of their horizontal distributions. The ephemeral nature of Mars mesospheric ice clouds in particular, with timescales as short as minutes (Listowski et al., 2014), is perhaps uniquely supported by the near-simultaneity of MARCI nadir and CRISM limb observations.

5.1. CRISM limb images

Fig. 19 presents a set of greyscale CRISM limb images for mesospheric CO_2 (panels A–E) and H_2O (panels F–G) ice clouds. Visible colors for these distinct mesospheric cloud layers are generally muted and affected by reflected illumination from the lower surface and atmosphere of Mars. Cloud particle sizes, which affect near-IR color ratios, vary among the presented mesospheric CO_2 ice clouds (panels A–E) from R_{eff} = 0.4–0.7 μm (panel B) to R_{eff} = 2 μm (panel A). Mesospheric H_2O ice clouds typically exhibit much smaller particle sizes (Fig. 12) and so are generally much less bright than mesospheric CO_2 clouds (Fig. 15). The mesospheric H_2O ice clouds in Fig. 19 (panels F, G) are both brighter and with slightly larger particle sizes (R_{eff} = 0.25–0.3 μm) than typical for such clouds. Both CO_2 and H_2O ice clouds often exhibit vertical layering where different altitude layers exhibit different particle sizes (panel B), although it is difficult to determine whether such layers are vertically or horizontally (along the limb path) stratified in limb viewing geometry. Mesospheric polar hood (H_2O ice) clouds, which are more widely distributed than wave clouds by nature, clearly exhibit vertical gradients in ice cloud particle sizes (e.g., Fig. 7).

The CRISM limb images of Fig. 19 offer limited views of horizontal gradients in mesospheric cloud opacities and particle sizes. The strongest horizontal variation in cloud brightness for a mesospheric CO_2 cloud in Fig. 19 is for 27May2014 (panel E, L_s = 137°). Fig. 20 presents 4 vertical profiles of limb brightness ($I/F_{\lambda=0.6\ \mu m}$) and corresponding reflectance spectra at 60–61 km (aeroid) for the color symbols/lines sampled horizontally across the limb image. Although the limb brightness varies by more than a factor of two among these positions, there is no indication that the cloud particles sizes vary by > 5–10% in association with these brightness changes. These are of course limb path integrated values that can lead to considerable spatial averaging along the limb fov. Määttänen et al. (2010) characterize perhaps ± 20% variations in cloud particle sizes within individual nadir, HRSC imaged mesospheric CO_2 clouds. These are quite bright clouds with R_{eff} of order 1.5–2.5 μm and optical depths of several tenths. Nadir imaging of mesospheric clouds requires such large optical depths both for identification and especially for surface-shadow derived opacities and cloud particle sizes.

5.2. MARCI nadir images

Wide-angle MARCI imaging provides daily global image maps of the Mars surface and atmosphere in ultraviolet and visible bandpasses (Malin et al., 2001), on the same MRO spacecraft from which CRISM limb observations are obtained. This provides nearly simultaneous nadir views of mesospheric clouds observed by CRISM, although with important limitations. The wide-angle global images provide the most extensive spatial coverage for mesospheric clouds, but also lead to modest spatial resolution (~1 km) that limits morphological assessments (e.g., cirrus versus cumulus) and cloud-surface contrast. In addition, there is a ~8 min offset in time between when a mesospheric cloud is observed by CRISM at the forward limb and when MARCI images the same cloud in the nadir. This introduces both a temporal offset, which is a significant fraction of mesospheric CO_2 cloud decay timescales (~20 min) outside of saturation conditions within gravity wave cold pockets (Listowski et al., 2014), and a longitudinal offset associated with Mars rotation over this time interval (~2° westward). The latter effect is more than compensated by the > 10° longitudinal extent of MARCI image swath widths. MARCI visible images also do not provide cloud compositional information, such as provided by CRISM and OMEGA near-IR spectral coverages (Montmessin et al., 2007; Vincendon et al., 2011). MARCI nadir imaging can, however, distinguish the high altitudes of mesospheric clouds through color image registration (parallax), similar in fashion to how high altitude clouds are defined in THEMIS, CRISM, and HRSC nadir images (McConnochie et al., 2010; Scholten et al., 2010; Vincendon et al., 2011).

As displayed in Figs. 21 and 22, MARCI nadir imaging provides extensive 2D imaging coverage in relation to CRISM limb measurements of Mars mesospheric CO_2 clouds. The left panels in each figure present color images with MARCI color filter registrations assigned to MOLA surface elevations. In this case, surface features (and near surface clouds) present good color registration while substantially elevated atmospheric clouds show distinct color separations. Color images (not

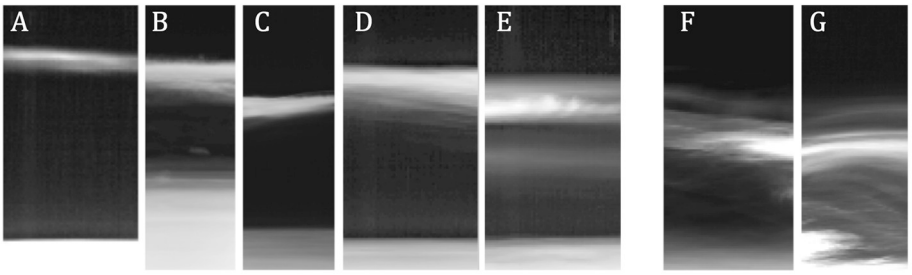

Fig. 19. CRISM limb images of mesospheric ice cloud layers: [A] CO_2 ice, 13Dec2013, L_s = 62°, 15S 73W, I/F (λ = 0.6 μm) = 0.08 at Z_{tan} = 65 km, R_{eff} = 2.0 μm; [B] CO_2 ice, 4Sep2015, L_s = 37°, 16S 356W, I/F (λ = 0.6 μm) = 0.07, 0.18, 0.02 at Z_{tan} = 57, 64, 67 km, R_{eff} = 0.6, 0.7, 0.4 μm; [C] CO_2 ice, 28Feb2016, L_s = 115°, EQ. 76W, I/F (λ = 0.6 μm) = 0.16 at Z_{tan} = 64 km, R_{eff} = 1.5 μm; [D] CO_2 ice, 5Feb2014, L_s = 86°, 13S 77W, I/F (λ = 0.6 μm) = 0.13 at Z_{tan} = 62 km, R_{eff} = 1.8 μm; [E] CO_2 ice, 27May2014, L_s = 137°, 8S 73W, I/F (λ = 0.6 μm) = 0.08 at Z_{tan} = 61 km, R_{eff} = 1.3 μm; [F] H_2O ice, 31Mar2011, L_s = 265°, 36S 100W, I/F (λ = 0.6 μm) = 0.05 at Z_{tan} = 62 km, R_{eff} = 0.25 μm; [G] H_2O ice, 31Mar2011, L_s = 265°, 25S 102W, I/F (λ = 0.6 μm) = 0.03 at Z_{tan} = 68 km, R_{eff} = 0.3 μm.

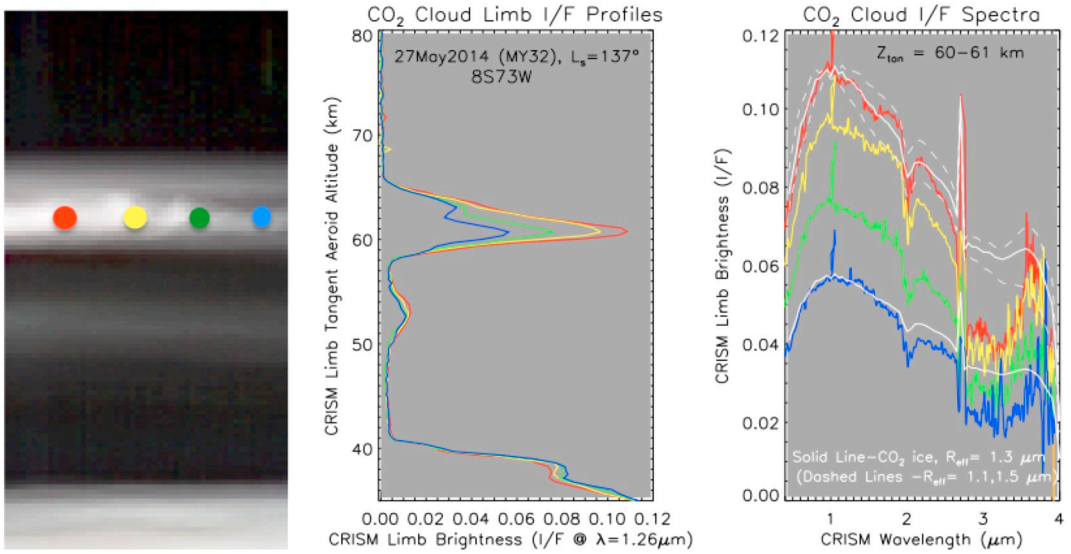

Fig. 20. The presented aerosol analyses employ limb profile brightness spectra that have been averaged along the in-orbit horizontal imaging direction of the CRISM observations. Spatial variations are typically modest over this ~30 km limb imaging direction (e. g., Fig. 19). The above image displays among the larger such variations (left, also in Fig. 19E), binned profiles of limb brightness across this horizontal extent (center, color coded to the locations), and binned spectra from 60 to 61 km peak scattering altitudes (right, same color coding versus position). Although the aerosol optical depth clearly varies along the limb, the CO_2 cloud particle sizes apparently do not. A fitted R_{eff} = 1.3 ± 0.2 μm spectral dependence for CO_2 ice (solid, dashed white lines) implies modest, if any, particle size variations.

shown) with registration set to the 60–70 km altitudes of mesospheric CO_2 clouds (as spectrally identified in coincident CRISM limb spectra), display white wispy (CO_2) clouds above strongly color-separated surface features. The right panels of Figs. 22–21 present violet-only MARCI images, registered spatially to a fixed altitude of 70–65 km above the surface. The widespread extent and wavelike patterns of linear, wispy cloud structures of mesospheric level clouds in these MARCI image sets correspond to the most extensive (in latitude) set of CRISM limb detections for bright mesospheric CO_2 clouds.

In the case of Fig. 21, a 4Sept2015 set of CRISM limb observations of mesospheric CO_2 ice clouds at L_s = 37° in MY33 (Figs. 5, 16, 19B) corresponds to both linear arcuate and clumpy bands of wispy high altitude clouds that extend for 10° or more in latitude and longitude over the Meridiani region. CRISM limb spectra taken along the 0W longitude of the MARCI image show CO_2 ice clouds at latitudes of 23S–6N, but the brightest such clouds are observed over the 13S–6N region of clouds exhibited in the MARCI image of Fig. 21. In the case of Fig. 22, a 28Feb2016 set of 17S–equator CRISM limb observations of mesospheric CO_2 ice clouds at L_s = 115.5° in MY33 (Figs. 5, 19C) corresponds to remarkably dense MARCI display of mesospheric clouds visible over a 10° × 10° expanse of latitude and longitude centered on the Valles Marineris region (75W, another center of mesospheric CO_2 cloud occurrence). They appear as a series of linear cloud streaks, oriented SE to NE or E to W and extending over ~30–100 km spatial scales individually. They are most prominent in the MARCI image where CRISM limb spectra show the brightest cloud I/F, from 10S to the equator.

A unique aspect of these MARCI views of mesospheric CO_2 clouds is their extended spatial range. Current nadir images of mesospheric clouds have generally extended over longitudinal ranges of 1° or less, and over latitudinal ranges of 1–3°. The MARCI images of Figs. 21 and 22 demonstrate that extensive latitudinal and longitudinal ranges can occur for these mesospheric CO_2 clouds, indicating the wave forcing conditions for these clouds are similarly extended at these times. Only quite bright mesospheric clouds can easily be identified in MARCI global color images, and such clouds are most easily discriminated when the lower atmospheric clouds and dust are minimized to provide peak surface-atmosphere contrast. Hence, fainter H_2O ice clouds prevalent during the perihelion season and CO_2 clouds presented above the aphelion cloud belt are not well characterized in MARCI imaging.

6. MCS comparisons

The Mars Climate Sounder (MCS) obtains limb scanned radiances in 8 thermal IR bandpasses (λ = 12 to 45 μm) and 1 solar band average bandpass from the Mars Reconnaissance Orbiter (MRO). The MRO orbit supports MCS and CRISM limb scans with pole-to-pole latitudinal coverage in ~13 orbit/longitude swaths per Mars day. However, MCS observes the atmospheric limb in the backward versus the forward (CRISM) direction of the MRO orbit, which leads to a ~16 min offset, in

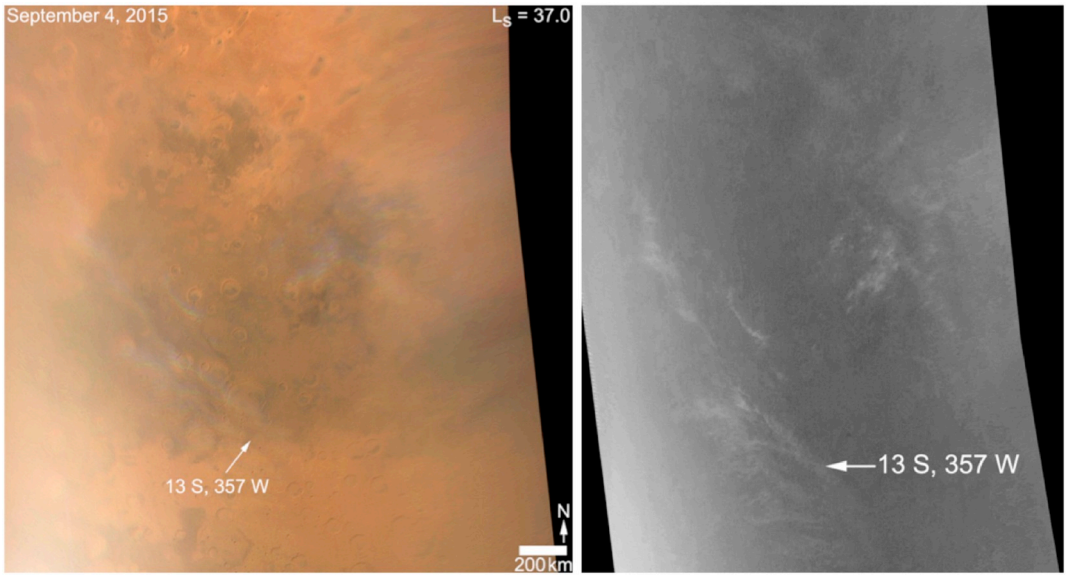

Fig. 21. MARCI daily global color imaging of the Mars surface and atmosphere on the MRO spacecraft provides contemporaneous (within 10 min) nadir imaging of the CRISM limb views, providing an extended spatial view of bright mesospheric CO_2 clouds through parallax separation of the MARCI color bands. In the left image, the MARCI color registration is based on a surface image plane such that wispy mesospheric CO_2 clouds at 60–70 km altitudes (compositionally identified in CRISM limb observations, Figs. 1B, 5, and 19B) are color misregistered. The violet (437 nm) MARCI image at right, which provides optimum cloud-surface contrast, is registered to a surface elevation of 65 km to reveal CO_2 cloud waveforms extending over Terra Meridiani (4Sep2015, L_s = 37°). The arrow indicates the approximate location of the corresponding CRISM limb observation.

measurements for the same limb tangent latitude. This also leads to a ~4° longitudinal offset, westward, for the MCS versus CRISM limb tangent longitudes, for the same viewed latitude. Despite these temporal/spatial offsets in MCS/CRISM limb observations, reasonably good comparisons are found between CRISM and MCS dust and H_2O ice profile retrievals for the lower atmosphere (Smith et al., 2013). The spatial/temporal offsets between MCS and CRISM limb observations are, however, more significant with respect to the temporal and spatial scales of variation for mesospheric ice clouds.

MCS and CRISM dust and H_2O ice aerosol measurements are very distinct in their wavelength coverages such that aerosol absorption versus aerosol scattering opacities are returned from MCS versus CRISM limb observations. Because aerosol scattering cross sections (and phase functions) are much more sensitive to aerosol particle sizes, CRISM limb aerosol retrievals are more dependent on, and sensitive to, aerosol particle sizes. MCS aerosol retrievals (and the lower atmospheric CRISM aerosol retrievals of Smith et al., 2013) assume larger Mars dust and H_2O aerosol particle sizes (R_{eff} = 1.06 and 1.41 μm, respectively, for

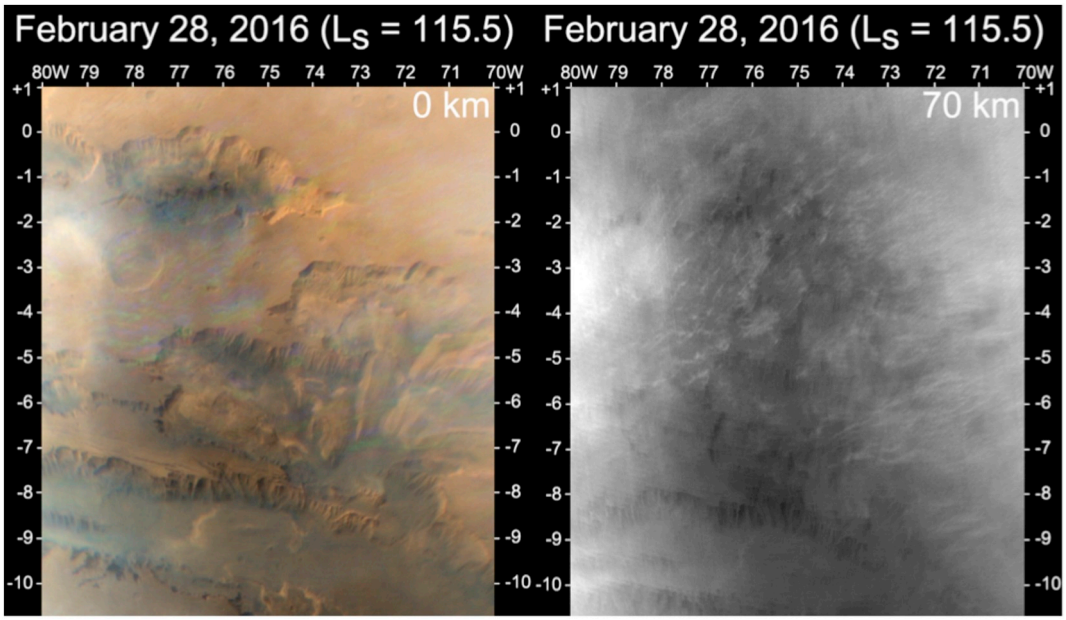

Fig. 22. MARCI daily global color imaging of the Mars surface and atmosphere on the MRO spacecraft provides contemporaneous (within 10 min) nadir imaging of the CRISM limb views, providing an extended spatial view of bright mesospheric CO_2 clouds through parallax separation of the MARCI color bands. In the left image, the MARCI color registration is based on a surface image plane such that wispy mesospheric CO_2 clouds at 60–70 km altitudes (compositionally identified in CRISM limb observations, Figs. 5 and 19C) are color misregistered. The violet (437 nm) MARCI image at right, which provides optimum cloud-surface contrast, is registered to a surface elevation of 70 km to reveal CO_2 cloud waveforms extending over the elevated Valles Marineris region (28Feb2016, L_s = 115.5°).

MCS; Kleinböhl et al., 2011) typical of lower atmospheric aerosol populations, but less appropriate for Mars mesospheric aerosols. In these respects, MCS and CRISM mesospheric aerosol retrievals present challenges in terms of direct quantitative comparisons. An interesting counterpoint to these distinctions regards the presence of mesospheric CO_2 ice clouds, which scatter conservatively over all MCS wavelength channels except within the 15 μm CO_2 gas band absorption. In fact, CO_2 ice clouds are not retrieved in MCS data processing in part because they lead to 15–16 μm (MCS channels A1–A3) scattering/emission enhancements that interfere with MCS temperature retrievals. Nevertheless, larger particle-size ($R_{eff} \geq 1$ μm) mesospheric CO_2 ice clouds are identifiable due to their scattering of Mars surface thermal IR emission into all MCS channels. These scattering contributions in MCS limb radiances can be presented in a similar fashion to the CRISM single scattering spectral analyses versus CO_2 ice cloud R_{eff}, but in even simpler terms as the direct (solar) component is not important except for the solar band MCS channel (A6) radiances. Hence, the single scattering phase function is less important because these clouds are only illuminated diffusely (i. e., over a large range of scattering angles) from below.

The following MCS and CRISM mesospheric aerosol comparisons are limited in numbers and purpose. The basic goal is to assess their consistency in terms of defining the seasonal/spatial distributions for Mars mesospheric dust and H_2O aerosols, and in their consistency in defining mesospheric CO_2 ice cloud occurrences and particle sizes. Published MCS mesospheric aerosol results include the spatial and seasonal dependences of MCS loop cloud detections (i. e., discrete aerosol layers) in MCS mesospheric limb radiances (Sefton-Nash et al., 2013), constraints on mesospheric dust loading in non-global dust storm conditions (Kleinböhl et al., 2015), and the identification of mesospheric CO_2 cloud scattering in MCS radiances at 60 km altitudes (Puspitarini et al., 2016). This current study considers the spatial/seasonal distribution of MCS mesospheric loop clouds in the context of CRISM mesospheric aerosol distributions, specific comparisons of mesospheric dust and H_2O/CO_2 ice identifications in the two data sets, mesospheric CO_2 ice particle sizes implied in MCS day and nighttime loop cloud radiances, and MCS mesospheric temperature profiles associated with specific CRISM dust and H_2O/CO_2 aerosol measurements. The selected comparisons are representative rather than comprehensive, consistent with the limited goals of this study.

6.1. Aerosol distribution comparisons

Overall, the spatial and seasonal distributions of MCS loop clouds presented in Figs. 7–9 of Sefton-Nash et al. (2013) are quite similar in character to those exhibited by the CRISM limb observations of Mars mesospheric aerosols (current Figs. 9 and 10). Fig. 7A of Sefton-Nash et al. (2013) presents solar band (A6) distributions in latitude/L_s characteristic of daytime mesospheric CO_2 clouds with low latitudes, altitudes of 53–80 km, and a seasonal range of Ł$_s$ = 0–150° with a distinct minimum over L_s = 40–100°. A somewhat similar low latitude distribution is apparent for band A4 (12 μm), although less distinct and with somewhat lower altitude ranges (surface altitudes of 53–70 km). Additional mid-latitude loop clouds are identified in this season in both channels, but the altitudes of these distinct latitude populations for aphelion clouds are not distinguished in Fig. 9 of Sefton-Nash et al. (2013). The MCS loop cloud distribution for the perihelion season (L_s ~150 – 360°) is also similar in many respects to that presented in the CRISM limb observations, although the low latitude minimum in mesospheric aerosols is more pronounced in the MCS versus the CRISM observations.

The MCS spatial/seasonal distributions of mesospheric loop clouds presented in Figs. 7, 9, and 11 of Sefton-Nash et al., 2013 are not very specific to mesospheric aerosol composition as they present MCS channel radiances in solar band (A6) and H_2O ice band (A4, 12 μm) MCS channels. Solar band scattering does not distinguish aerosol composition and while the MCS A4 channel is most sensitive to H_2O ice emission, it is also very sensitive to CO_2 ice scattering, as shown below. In order to characterize potential mesospheric aerosol compositions, Sefton-Nash et al. (2013) employ MCS mesospheric temperatures, which indicate cold atmospheric temperatures suggestive of aphelion CO_2 ice and perihelion H_2O ice (their Fig. 11). In addition, MCS long wave channel ratios (B1/B2, where B1 ~ 31 μm and B2 ~ 42 μm) are modeled in terms of their capability to distinguish dust from ice (their Fig. 12). Sefton-Nash et al. (2013) conclude that dust constitutes a modest fraction of the MCS loop cloud detections. It is not clear whether the 2007 (MY28) global dust storm period is included in the presented MCS loop cloud detections, but the employed loop cloud detection algorithm is not designed to detect spatially extended mesospheric dust loading associated with such storms (Heavens et al., 2015).

6.2. Daytime and nighttime CO_2 clouds

Mesospheric CO_2 clouds exhibit relatively few absorption bands, which also coincide with strong gas CO_2 absorption bands. Given that MCS temperature profiling depends on strong 15 μm CO_2 gaseous emission/absorption and Mars CO_2 ice clouds contribute scattering rather than emission, CO_2 ice opacities are not a standard product of MCS profile retrievals. Nevertheless, this scattering signal is well recognized for polar winter (Hayne et al., 2012) and aphelion mesospheric (Puspitarini et al., 2016) CO_2 clouds. Here, we consider the CO_2 ice particle size dependence of MCS spectral radiances in the context of near-coincident CRISM CO_2 ice cloud particle size determinations.

Figs. 23 and 24 present latitude cross sections of MCS radiances in 1 visible (A6) and 7 thermal infrared (A1–A5, B1, B2) channels that include distinct mesospheric ice cloud “loops” associated with CO_2 ice clouds. The daytime MCS loop clouds in Fig. 23 correspond with CRISM limb observations of a particularly bright set of mesospheric CO_2 clouds on 28Feb2016 (MY33, L_s = 115.4°) with relatively large particle sizes (R_{eff} = 1–2 μm). CRISM observed aspects of these clouds are presented in Figs. 5, 19C, and 22. Although the CRISM limb observations of CO_2 clouds are offset in longitude by ~4°E relative to the MCS limb scans, the MARCI cloud imaging of Fig. 22 shows that the CRISM and MCS limb observations pertain to an extensive (≥10°) longitudinal and latitudinal set of mesospheric CO_2 clouds. Three consecutive CRISM limb scans from 17S to the equator present CO_2 clouds; the MCS limb radiances of Fig. 23 exhibit loop clouds centered at 17S, 10S (very faint), and 7S (very bright), but not at the equator.

The channel or wavelength dependence of MCS loop clouds apparent in Figs. 23 and 24 (nighttime, discussed subsequently) reflects the particle size dependence of CO_2 cloud particle scattering. With respect to the bright 6S daytime MCS loop cloud of Fig. 23, scattered surface IR emission is identified in thermal IR channels A1–A5 (λ range of 12–22 μm), very faintly in B1 (λ = 32 μm), and scattered direct and reflected solar irradiance in the solar band A6 channel. With respect to the weaker 18S daytime MCS loop cloud of Fig. 23, scattered surface IR emission is identified in thermal IR channels A1–A4 (λ range of 12–17 μm) and scattered direct and reflected solar irradiance in the solar band A6 channel. Fig. 25 compares the relative radiance in MCS CO_2 loop cloud scattering versus MCS channel center wavelength, for two daytime (3 PM) observations (diamond and square symbols) and 1 nighttime (3 AM) MCS observation (asterisk symbols). The plotted wavelength variations in relative (arbitrary vertical scale) MCS channel radiances represent radiance departures from uniform (wavelength-independent) limb scattering of surface blackbody emission.

The various lines plotted in Fig. 25 represent the wavelength dependence of CO_2 scattering cross sections as a function of the ice particle size (R_{eff} = 1–7 μm), in relative units and scaled to match individual MCS observations. As indicated in the figure, the magnitudes of these scattering cross sections vary by orders of magnitude over the R_{eff} = 1–7 μm range, such that larger CO_2 ice particle sizes are much

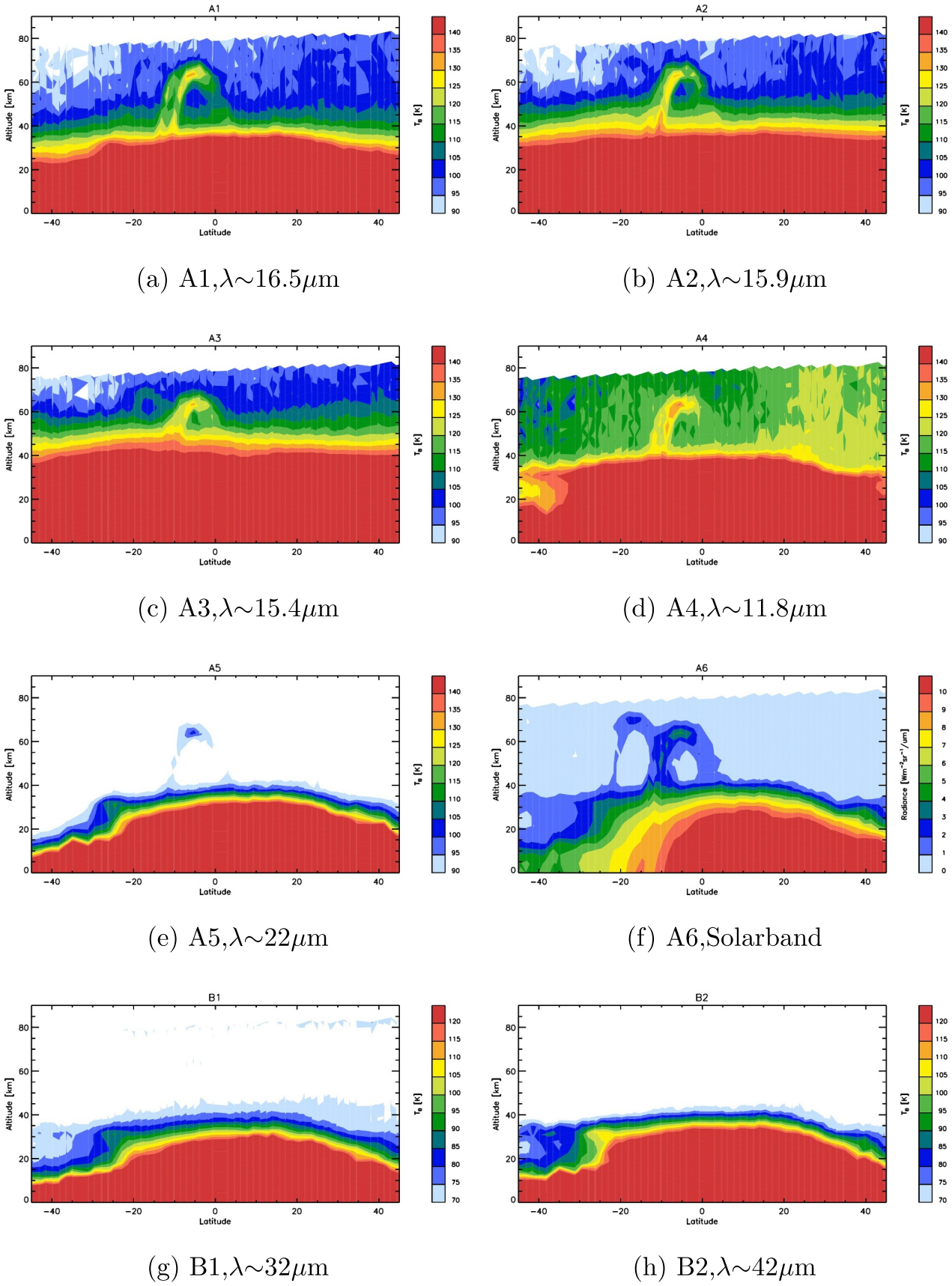

Fig. 23. Daytime (3 pm) 28Feb2016 (MY33, L_s = 115.4°, UTC = 15:10) loop clouds, extending over 17S–6S (80W), are presented for MCS thermal IR channels, corresponding to mesospheric CO_2 ice cloud scattering of surface thermal emission; and for band 6 (solar band, panel f), which is dominated by scattering of solar flux. These MCS latitude cross sections of brightness temperatures (apart from band 6) correspond to near-coincident (see text) CRISM limb measurements of CO_2 clouds (Figs. 5 and 19C) and to the MARCI nadir view of these clouds presented in Fig. 22. Such thermal IR scattering is strongly dependent of cloud particle sizes, such that larger particle sizes ($R_{eff} \geq 1$ μm) scattering in the MCS A channels (λ ≤22 μm) are most apparent.

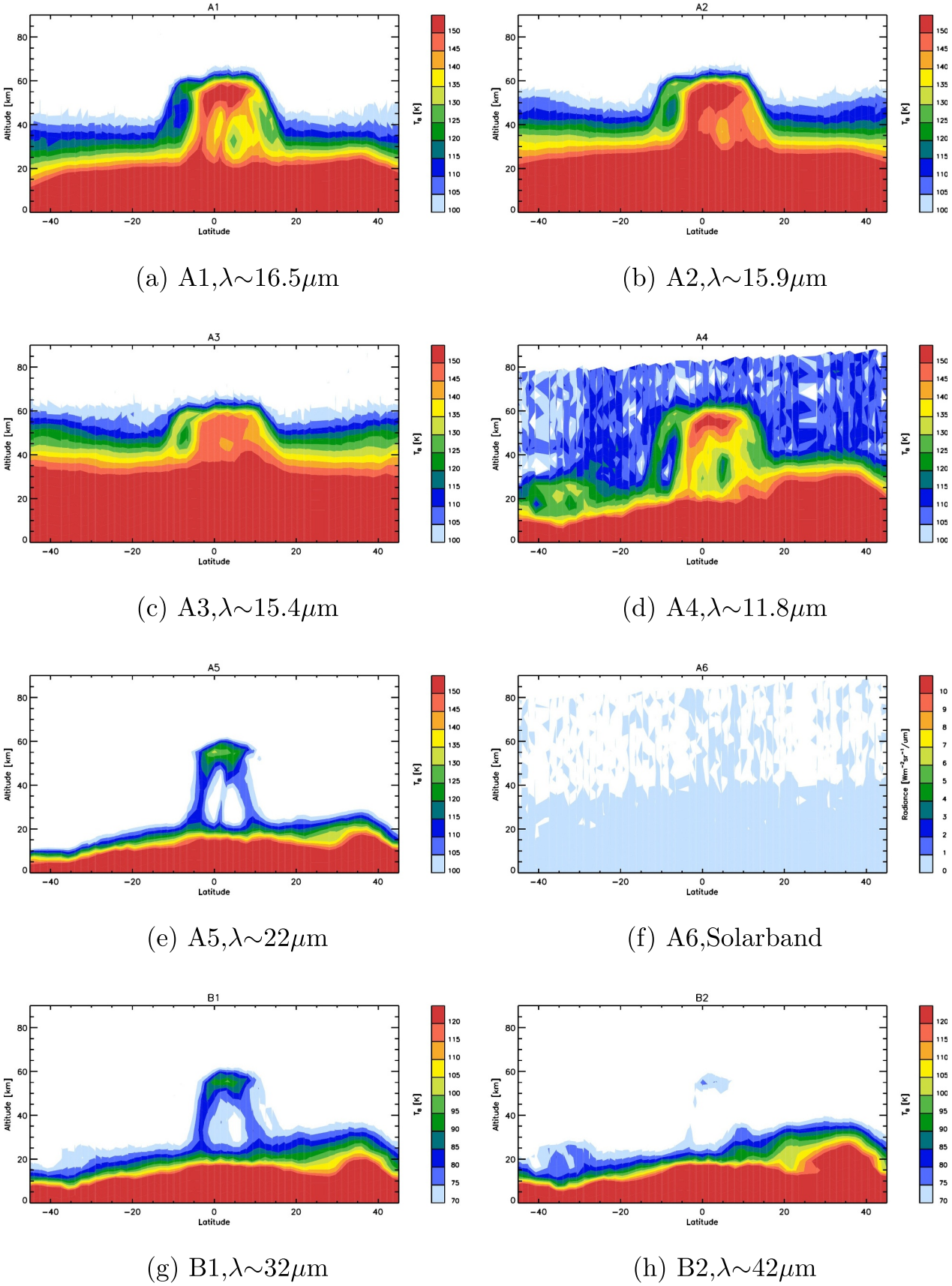

(a) A1,$\lambda\sim16.5\mu$m (b) A2,$\lambda\sim15.9\mu$m

(c) A3,$\lambda\sim15.4\mu$m (d) A4,$\lambda\sim11.8\mu$m

(e) A5,$\lambda\sim22\mu$m (f) A6,Solarband

(g) B1,$\lambda\sim32\mu$m (h) B2,$\lambda\sim42\mu$m

Fig. 24. Nighttime (3 am) 6Mar2008 (MY29, L_s = 41.1°, UTC = 00:38) loop clouds over the Xanthe Terra region (EQ42W) appear in all MCS thermal IR channels (with no solar illumination for band A6), indicating surprisingly large particle sizes (R_{eff} ~ 7 μm) at much lower altitudes (55–60 km aeroid) than previously recognized for nighttime mesospheric CO_2 clouds (> 90 km in Montmessin et al., 2006). These nighttime lower mesospheric CO_2 clouds appear frequently over the same locations and seasons as daytime mesospheric CO_2 clouds, based on Figs. 6, 7C of Sefton-Nash et al. (2013).

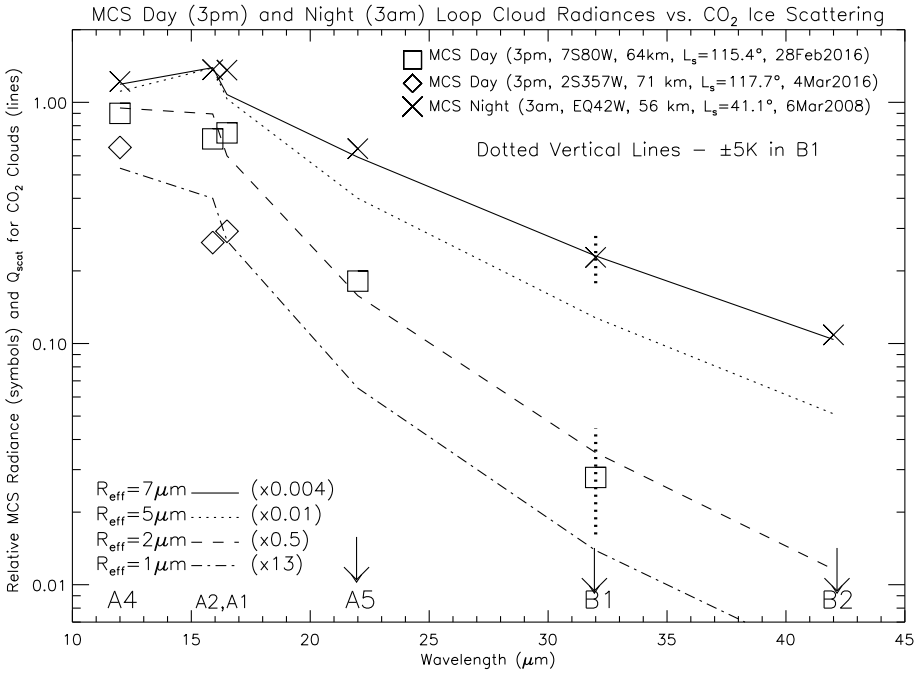

Fig. 25. The MCS channel, or wavelength, dependence of surface thermal IR emission scattered by mesospheric CO_2 clouds is strongly indicative of cloud particle sizes. The relative variations of MCS channel brightness temperatures are presented for two daytime (3 pm, MY33) mesospheric CO_2 clouds (square and diamond symbols, both associated with near-coincident CRISM CO_2 cloud measurements) and one nighttime (3 am, MY29) mesospheric CO_2 cloud (X symbols). Scaled scattering cross sections for CO_2 ice spheres with R_{eff} of 1–7 μm are compared as indicators of the effective particle sizes for these three MCS loop cloud observations. The range of scaling applied to these cross sections (lower left) indicates how strongly this scattering depends on cloud particle size for a given cloud particle number density. MCS approximate channel wavelengths are indicated at the bottom of the figure. Symbols with arrows indicate upper limits for MCS radiances, dotted vertical lines correspond to ± 5 K perturbations to observed B1 brightness temperatures.

brighter for a given cloud particle number density.

In this comparison of CO_2 ice scattering cross sections to relative MCS limb radiances, it is assumed that the wavelength-dependent departure of the MCS channel radiances from simple illumination by black body surface emission arises only from the wavelength-dependent scattering cross sections for CO_2 ice particles as a function of the ice particle size. Towards the modest goals of this analysis, the comparison of Fig. 25 serves to demonstrate the coarse sensitivity of the observed MCS limb radiances to CO_2 cloud particle size.

The MCS daytime cloud loops presented in Fig. 23 (28Feb2016) are denoted by square symbols in Fig. 25, where only an upper limit is indicated for the channel B2 radiance (indicated by arrow symbol). These loop clouds are consistent with cloud particle sizes of order R_{eff} = 2 μm, similar to CRISM derived CO_2 cloud particle sizes for this same season and approximate location (R_{eff} = 1.5 μm). The diamond symbols in Fig. 25 represent an isolated daytime mesospheric CO_2 cloud detected in near-coincident MCS and CRISM limb observations on 4Mar2016 over Meridiani. MCS channel radiance detections for this case extend over channels A1–A4 (and A6), indicating much smaller CO_2 ice particle sizes (R_{eff} < 1 μm). CRISM observations near-coincident with this MCS observation indicate CO_2 ice particles with R_{eff} = 0.5 μm.

One of the more striking aspects of mesospheric aerosol loop cloud distributions presented in Sefton-Nash et al. (2013) regards the nighttime (3 AM) A4 (12 μm) radiances in the aphelion season at low latitudes (Fig. 7C of Sefton-Nash et al., 2013). The seasonal variation of these MCS nighttime A4 loop clouds matches the seasonal character of daytime mesospheric CO_2 clouds (with a slight minimum over L_s = 40–90°), as do their latitudinal distributions. The plotted altitude distributions of Fig. 9 in Sefton-Nash et al., 2013 do not distinguish day and nighttime measurements, but overall peak altitudes extend from 55 to 65 km with latitudes of 15S–15N (longitudes are not specified). These nighttime mesospheric loop clouds, as displayed in Fig. 24, are also identified in MCS preprocessing that rejects scans with A2 (λ ~ 15.9 μm) signals associated with potential high altitude CO_2 clouds to prevent aerosol-biased MCS temperature retrievals. Such CO_2 cloud scattering is frequently identified (~5% of scans) in nighttime MCS limb radiances for the seasonal range of mesospheric daytime CO_2 clouds identified in non-MCS observations. This behavior strongly indicates nighttime mesospheric CO_2 clouds well below the high altitudes (90–100 km) of nighttime CO_2 clouds reported by Montmessin et al. (2006).

Fig. 24 shows MCS nighttime loop clouds observed over southeastern Xanthe Terra (EQ42W) on 6Mar2008 (L_s = 41.1°), corresponding to such lower mesospheric (~56 km), nighttime (3 AM) CO_2 clouds. In addition to the unexpected presence of such clouds, which further challenges the capability of Mars dynamical models to simulate CO_2 condensation temperatures in the Mars mesosphere, these clouds can exhibit surprisingly large particle sizes. This is evidenced by the presence of cloud scattering in the MCS longwave B1 (λ ~ 32 μm) and B2 (λ ~ 42 μm) channels in Fig. 24. As indicated in Fig. 25, the MCS channel radiances for this nighttime CO_2 ice cloud loop (there is also a weaker cloud feature to the south evident in the A1–A4 channels of Fig. 24) are consistent with cloud particle R_{eff} ~ 7 μm. Although the influence of minimum ~70 km temperatures associated with thermal tides is emphasized in the formation of daytime CO_2 clouds, thermal tides also produce nighttime minimum temperatures near 55 km, although not as cold a minimum as modeled for the daytime lower mesosphere (e. g., Fig. 5 of González-Galindo et al., 2011).

6.3. Temperature comparisons

Given the distinct mesospheric thermal conditions associated with dust, H_2O ice, and CO_2 ice aerosols, it is instructive to compare near-coincident MCS and CRISM aerosol measurements for each aerosol type with near-coincident MCS mesospheric temperature profile retrievals. Fig. 26 presents such comparisons, including LMD MCD temperatures (Millour et al., 2014), for CRISM/MCS near-coincident measurements of mesospheric dust (a), H_2O ice (b), and CO_2 ice (c). Fig. 26a regard the most widespread indication of mesospheric dust aerosols in CRISM 2009–2016 limb observations, as measured on 14Nov2012 for L_s = 207°. This mesospheric dust loading corresponds to the early onset of MY31 regional dust lifting reported in MCS observations (Heavens et al., 2015), which is characterized by considerable spatial variations at this time. In the limited longitudinal coverage of CRISM limb observations, this regional dust storm is evidenced by relatively small particle size dust aerosols (R_{eff} = 0.7–0.5 μm at 50–55 km, and R_{eff} = 0.2 μm at 60–70 km) extending over latitudes of 8S to 26N for a central longitude of 3E (spectra presented in Fig. 8). Minor dust aerosols below 53 km are also identified in CRISM limb scans centered on

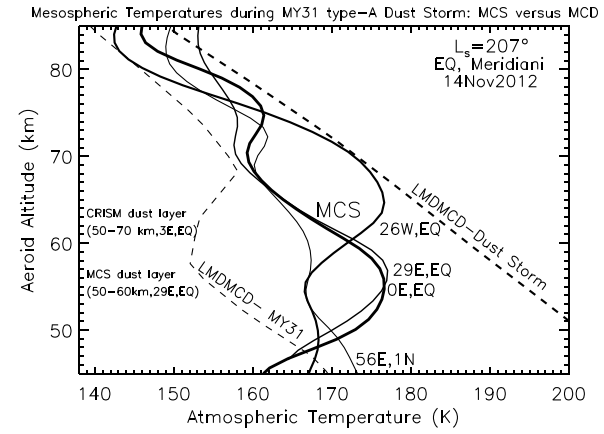

(a) Dust

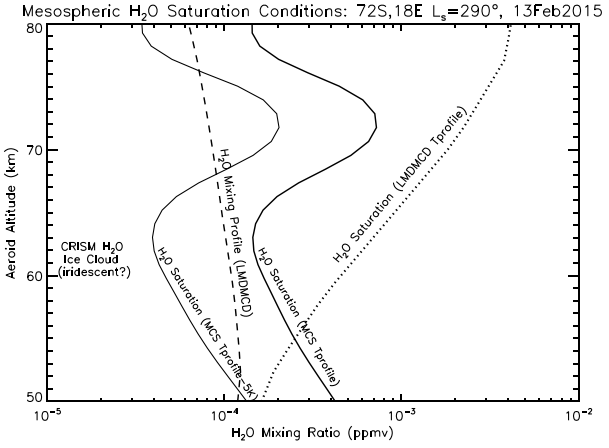

(b) H_2O Ice

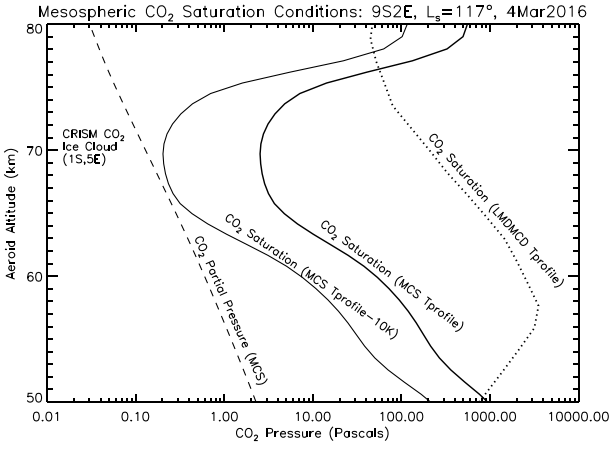

(c) CO_2 Ice

longitudes of 75W and 70E for latitudes of 26N and 30S, respectively. MCS equatorial profile retrievals for this period indicate mesospheric dust loading up to 60 km altitudes at 29E longitude, none detected at a longitude of 26W, and small dust opacities presented over 50–52 km altitude for a longitude of 0E. However, MCS retrieved temperatures for all three of these longitudes are significantly elevated over 50–70 km altitudes, as shown by the solid line temperature profiles in Fig. 26a. LMD MCD simulated mesospheric temperatures for average dust activity (MY31, thin dashed line) and global dust loading conditions (thick dashed line) indicate considerable dust heating of the mesosphere applies for all three MCS observed longitudes.

Fig. 26. MCS mesospheric temperature retrievals in close association in time and space with CRISM limb aerosol measurements indicate correspondences with dust heating (top panel A), and H_2O (middle panel B) CO_2 (bottom panel, C) saturation conditions. A) MCS and CRISM limb observations detect equatorial mesospheric dust associated with an L_s = 207° regional storm in MY31. MCS mesospheric temperatures indicate atmospheric heating over the 26W–56E longitude region, as compared to LMD MCD simulations of MY31 and Dust Storm conditions; B) CRISM detection of a mesospheric H_2O ice cloud (shown in Fig. 6) corresponds to a distinct minimum in retrieved MCS temperatures, approaching H_2O saturation conditions based on LMD MCD water vapor (but not temperature) simulations; C) CRISM detection of a mesospheric CO_2 ice cloud corresponds to a minimum in MCS mesospheric temperatures measured 8 degrees southward. This is ~10 K above CO_2 saturation conditions, which is comparable to the MCS temperature error. LMDGCM simulated temperatures are ~15 K warmer than returned by MCS.

In Fig. 26b, we consider MCS mesospheric temperatures retrieved near-coincident with CRISM limb measurements of mesospheric H_2O ice clouds on 13Feb2015 (L_s = 290°) at 73S (338W). Mesospheric water ice clouds are observed over a larger latitudinal range (20N–40N, 20S–75S) in CRISM limb observations at this time, but the 75S observation is notable in terms of larger particle sizes (R_{eff} = 0.5–0.7 μm) and indications of water ice cloud iridescence (Fig. 6). MCS limb observations exhibit increased A4 (12 μm) and A6 (solar band) radiances at 40S–70S latitudes for altitudes of 40–60 km, although not sufficient for water ice opacity retrievals. MCS retrieved mesospheric temperatures, near-coincident with the CRISM identified H_2O ice cloud at 72S over 58–64 km altitudes, are presented in Fig. 26b in terms of H_2O saturation mixing ratios for the MCS retrieved temperature profile (heavy solid line) and these MCS temperatures decreased by 5 K at all altitudes (thin solid line). The LMD MCD model H_2O vapor mixing profile and H_2O saturation profile (based on LMD MCD temperatures) are indicated by dashed and dotted lines, respectively. The MCS retrieved mesospheric temperatures indicate that H_2O ice condensation is approached at the altitudes of the CRISM water ice cloud detection, the lack of MCS retrieved water ice opacity presumably reflects the ephemeral timescales for these mesospheric clouds relative to the temporal/spatial offsets of the MCS and CRISM limb measurements.

Similarly, Fig. 26c presents CO_2 ice saturation conditions relevant to CRISM limb measurements of a bright (limb I/F = 0.15) CO_2 ice cloud observed on 4Mar2016 (L_s = 117°, MY33) at 1S5E and an altitude of 70 km. This is an isolated, iridescent CO_2 cloud in CRISM limb observations with relatively small cloud particle sizes (R_{eff} = 0.5 μm). It is also detected in MCS A1, A2, and A4 radiances (diamond symbols in Fig. 25) and occurs 4 days after the extensive set of mesospheric CO_2 clouds presented in the MARCI images of Fig. 22 (see also Fig. 27). The observed MCS 15 μm scattering by CO_2 ice precludes MCS temperature profile retrievals for CO_2 saturation calculations so that we must employ MCS temperatures ~8° to the south (9S2E) to consider potential CO_2 saturation conditions for this cloud observation. Fig. 26c presents such CO_2 saturation conditions for MCS retrieved (solid lines) versus LMD MCD simulated mesospheric temperature profiles, relative to the MCS derived CO_2 partial pressure profile (dashed line). Despite the 8° shift in latitude between the CRISM (and MCS) CO_2 cloud detections and the employed MCS temperature profile, there is a strong suggestion that ~70 km CO_2 saturation conditions accompany these clouds (Fig. 26c). However, we stress that MCS does not measure CO_2 ice saturation temperatures. MCS observed (at 9S2E) temperatures at 70 km are 117 K, whereas CO_2 saturation temperatures fall below 105 K. Due

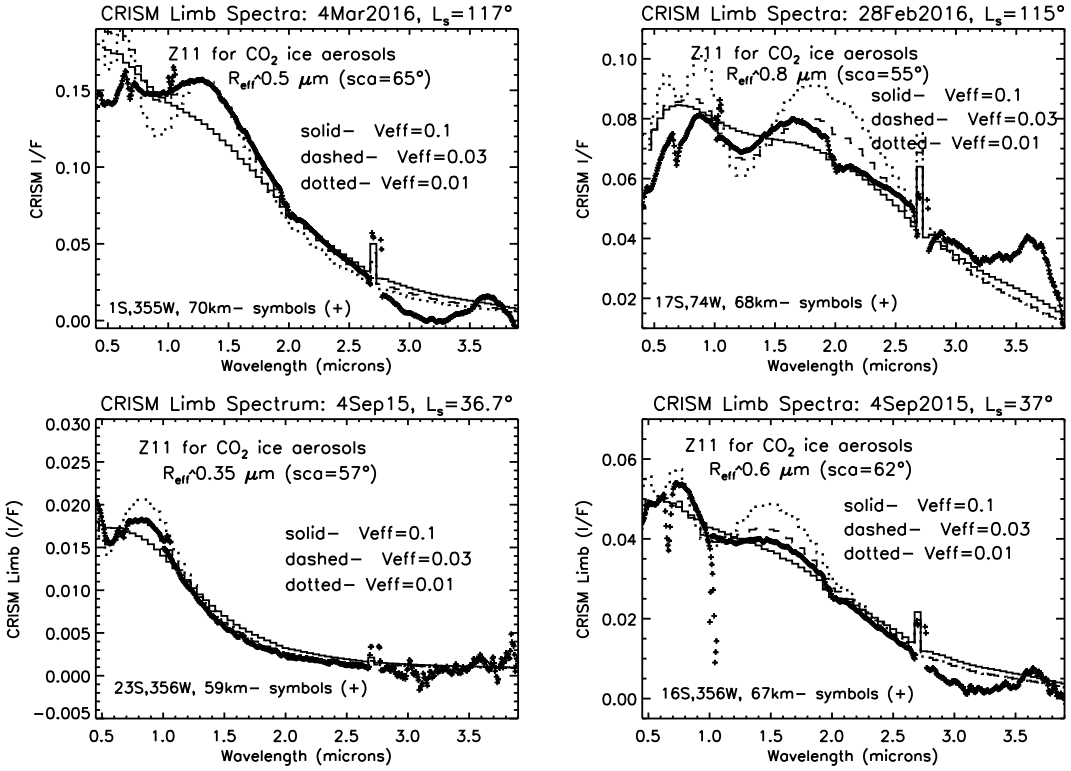

Fig. 27. A set of four CRISM limb reflectance spectra indicating narrow particle size distributions ($V_{eff} \sim 0.03$) for mesospheric CO_2 ice clouds. The CRISM observed spectra (bold + symbols) are compared to SSA fitted reflectance spectra employing T-Matrix scattering phase functions generated for CO_2 ice with cylindrical shapes (D/L = 1). Modeled spectra with solution R_{eff} indicated on each panel are generated for gamma particle size distributions employing size distribution widths (variances, V_{eff}) of 0.1 (solid lines), 0.03 (dashed lines), and 0.01 (dotted lines). The observed diffraction interference patterns are roughly consistent with $V_{eff} = 0.03$, implying that Mars mesospheric CO_2 ice clouds are significantly iridescent.

to 15 μm scattering by CO_2 ice, MCS mesospheric temperature retrievals are not configured to measure CO_2 saturation temperatures in the presence of mesospheric CO_2 ice clouds. It is also true that MCS temperature retrieval uncertainties increase to 10–15 K for the very low temperatures corresponding to these conditions (versus ~2 K for the temperature profiles of Fig. 26a and b).

7. Cloud iridescence

As discussed earlier, iridescence associated with Mars mesospheric clouds (and in particular, mesospheric CO_2 ice clouds) is expressed by interference patterns within CRISM limb 0.4–4 μm reflectance spectra (Fig. 5). This behavior is also presented in at least one CRISM limb observation of mesospheric H_2O ice clouds (Fig. 6). In Fig. 27, we present a set of CRISM limb spectra of mesospheric CO_2 ice clouds with spectral reflectance interference variations. All of the model comparisons derive from T-matrix code (Mishchenko et al., 1996; Mishchenko et al., 2016) simulations of scattering by specified size distributions of randomly oriented cylinders (D/L = 1) with CO_2 ice optical indices (Hansen, 2005). The phase of the observed interference patterns exhibited in Fig. 27 is dependent on particle shape, as demonstrated in Fig. 28a. Such particle shape dependence limits our ability to fit the observed interference variations in the observed limb spectra in detail. Averaging of different ice populations along the tangent cloud sampling further complicates precise model fits.

Roughly a third of the CRISM identified mesospheric CO_2 clouds indicate such cloud iridescence, but it is possible (perhaps likely) that most of the CRISM observed mesospheric CO_2 clouds are iridescent. This conclusion reflects the fact that, apart from one case, all of the observed CO_2 clouds with particle sizes (R_{eff}) less than ~1 μm exhibit iridescence, whereas CO_2 clouds with particle $R_{eff} > 1$ μm do not with one possible exception. This is generally consistent with the predicted scattering angle dependence of cloud iridescence versus cloud particle size (see Fig. 1 of Sassen, 2003), where the scattering angle for cloud iridescence display increases strongly with decreasing cloud particle size. The minimum scattering angle obtained from the CRISM limb observations of mesospheric CO_2 clouds is 51°, the largest is 79° (corresponding to the one case of small CO_2 cloud particles where iridescence is not detected). Optimum iridescence of cloud particle sizes (R_{eff}) of 1–3 μm is presented at scattering angles of 10–30°, versus > 30° for smaller particle sizes. The large scattering angles observed from CRISM indicate that even for smaller CO_2 particle sizes, interference diffraction orders will significantly overlap and iridescence will be weak (see below).

Terrestrial cloud iridescence is associated with diffractive interference by forward illuminated clouds with very narrow size distributions (nearly mono-dispersed), small water (or ice) particle sizes (e. g., $R_{eff} \leq 10$ μm), and equidimensional particle shapes (Neiman and Shaw, 2003; Sassen, 1979; Sassen, 2003). Terrestrial iridescent clouds are infrequently observed, due in part to their formation at high, cold altitudes (10–12 km) in isolated cirrus forms and jet contrails. They are closely related to coronal optical displays, but localized and extending to larger scattering angles (6–40°) due to smaller cloud particle sizes (e. g., $R_{eff} \leq 5-7$ μm). Hence, small cloud particle iridescence is ideally separated from the bright Sun for optimum optical display. Iridescence in clouds refers to their vibrant diffractive interference, blue-to-red color variations corresponding to changes in particle sizes of nearly mono-dispersed cloud particle populations along the cloud horizontal extent.

The observational geometry of CRISM limb spectroscopic imaging is not conducive to observing strong visible iridescence of mesospheric CO_2 clouds, given the lack of observational scattering angles < 50°, the limb path viewing through the horizontal extents of the clouds, and the predominance (in the case H_2O ice) of particle sizes smaller than visible

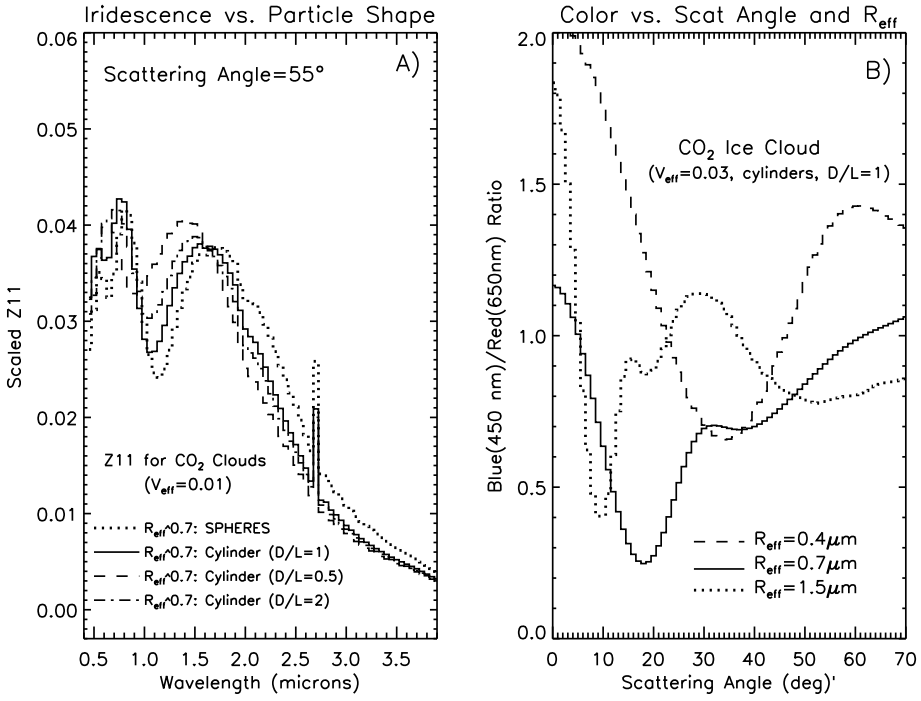

Fig. 28. A) The detailed spectral phase of diffraction interference patterns exhibited in CRISM limb scattering spectra of mesospheric CO_2 ice clouds can be affected by cloud particle shapes. Spectral (λ = 0.4–3.8 μm) scattering phase functions are plotted for CO_2 ice particles with gamma particle size distributions (R_{eff} = 0.7 μm, V_{eff} = 0.01), viewed at a scattering angle of 55°, and based upon particle shapes for spheres and cylinders with different aspect ratios (D/L = 1, 0.5, 2). B) Cloud iridescent colors are muted at the > 50° scattering angles sampled in CRISM limb observations of low latitude mesospheric CO_2 ice clouds. The scattering angle of peak iridescent red color occurs at scattering angles < 35° and depends strongly on cloud particle size. Optimum red color is obtained for $R_{eff} \geq 1$ μm at scattering angles ≤20°.

wavelengths. These conditions lead to increased multiple scattering, averaging of cloud particle size gradients, and overlapping of diffraction orders, all of which reduce iridescent colors. The CRISM limb images of Fig. 19 are presented in black and white because it is difficult to discern distinct visible colors for these clouds. On the other hand, Mars mesospheric clouds should be well suited to producing brilliant iridescent colors as viewed from the surface, at smaller scattering angles and along more normal (hence smaller) optical paths. This reflects the R_{eff} = 1–4 μm particle sizes of Mars ice clouds in general and the narrow size distributions of Mars mesospheric clouds in particular, both of which are optimum for forming iridescent displays. Fig. 28b presents scattering angle variations in red/blue phase function ratios for randomly oriented cylinders (D/L = 1) of CO_2 ice for three particle size distributions (R_{eff} = 0.4, 0.7, 1.5 μm), all with narrow size dispersions (V_{eff} = 0.03, cf. Fig. 27). Distinctly red cloud colors are indicated near scattering angles of 10 and 20° for ice particle R_{eff} of 1.5 and 0.7 μm. Weaker red colors (as increasingly affected by order overlap) are presented at scattering angles beyond 30° for smaller CO_2 ice particle sizes ($R_{eff} \leq 0.4$ μm).

7.1. CO_2 cloud formation conditions

The mono-dispersed particle sizes for iridescent clouds reflect uniform histories of cloud particle growth (referred to as “top hat”) generally consistent with abrupt forcing due to topographically (or jet) forced atmospheric waves. Uniform condensation conditions (temperature and condensation nuclei, CN) are also implied. The identification of iridescence in relatively small particle size CO_2 clouds (Fig. 27) indicates that CN particle sizes are small (R_{eff} < 0.03 μm) in order to avoid CN related increases in particle size variance. This limited constraint, coupled with the condition of (locally) uniform CN density, implied mesospheric cloud densities (0.1–10 cm^{-3}, Fig. 18), and the persistence (within seasonal and spatial constraints) of mesospheric CO_2 (and H_2O) clouds, suggest widely distributed CN sources with relatively high number densities that are not derived from seasonally dependent lower atmospheric aerosols. Meteoric ion chemistry, such as proposed by Plane et al. (2018) for molecular water clustered on Fe,$MgCO_3$ products of meteoric ablation, could perhaps meet such conditions. This argument is quantitatively supported by MAVEN IUVS measurements of mesospheric Mg^+ ions in the context of observed upper limits for Mg (Plane et al., 2018). Plane et al. (2018) further show that coagulation of these metal carbonate-molecular H_2O clusters can produce CN of sufficient size and densities to produce mesospheric CO_2 ice clouds with particle number densities of order 1 cm^{-3}, consistent with modeled (Listowski et al., 2014) and observed (Fig. 18) mesospheric CO_2 (and potentially H_2O) cloud particle number densities and optical depths. Other candidates include very fine dust or ice background aerosol particles, as suggested in SPICAM solar extinction measurements (Fedorova et al., 2014), although the widespread (in season and latitude) extent of mesospheric H_2O and CO_2 clouds would appear to favor a more global and seasonally independent CN source. Particle size variations in such aerosol CN will also tend to broaden the CO_2 particle size distribution variance (Eric Jensen, personal communication, 2018), which may not satisfy the observed, very narrow size distributions for mesospheric CO_2 clouds reflected in the current study.

8. Mesospheric O_2 singlet delta emission ($O_2(^1\Delta_g)$)

CRISM limb profiling of electronically excited O_2 emission at 1.27 μm in the lower Mars atmosphere is described in Clancy et al. (2017), in which such O_2 singlet delta ($O_2(^1\Delta_g)$) volume emission rate (VER) profiles are retrieved from the same CRISM limb profile data analyzed in the current study for mesospheric aerosols. Photolysis of O_3, which dominates $O_2(^1\Delta_g)$ production in the lower Mars atmosphere, leads to an anti-correlation of $O_2(^1\Delta_g)$ volume rates with water vapor, as water vapor photolysis products catalyze destruction of Mars odd oxygen species O_3 and O (Clancy et al., 2017; Nair et al., 1994). These CRISM $O_2(^1\Delta_g)$ profile retrievals extend to mesospheric altitudes (up to 76 km aeroid), but detections of emission peaks above 40 km are rare, although at high latitudes atomic O recombination creates distinctive winter polar peaks in 40–60 km $O_2(^1\Delta_g)$ emission rates (see below). In fact, for latitudes below 40NS, there are only 7 CRISM measurements of $O_2(^1\Delta_g)$ at altitudes above 60 km in this data set and they all occur in the cold aphelion period. Fig. 29 presents 1.27 μm limb brightness profiles (left panel) for 5 of these mesospheric $O_2(^1\Delta_g)$ measurements, compared to coincident (i. e., same limb observations) 1.2 μm limb brightness profiles (right panel) indicating bright CO_2 ice clouds.

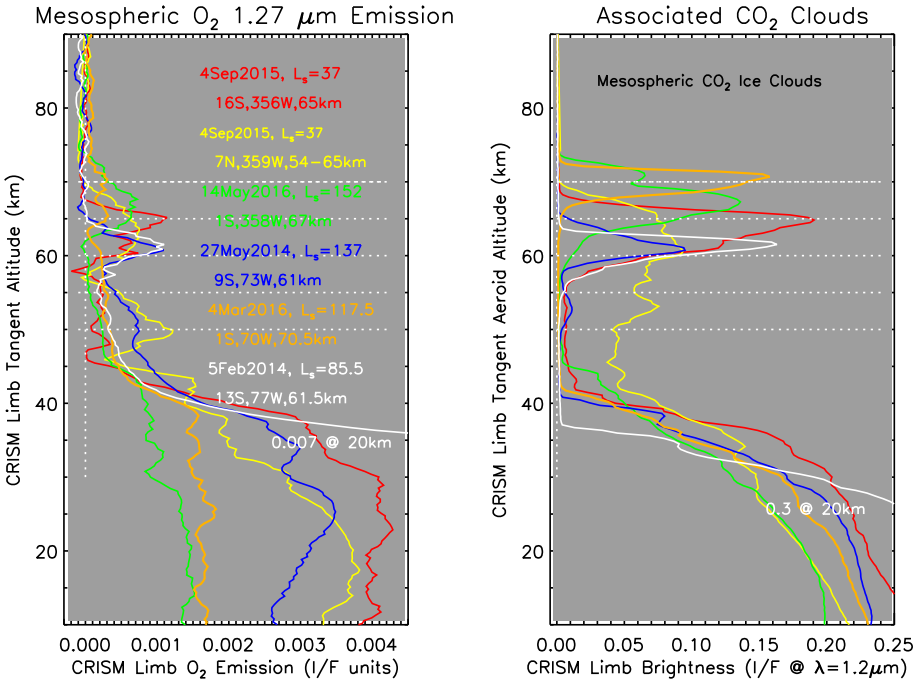

Fig. 29. Vertical profiles of CRISM limb radiance associated with $O_2(^1\Delta_g)$ emission ($\lambda = 1.27\,\mu m$, left panel) and mesospheric CO_2 ice scattering ($\lambda = 1.2\,\mu m$) show corresponding mesospheric layers for 6 limb profile observations (as coded by color). This represents roughly 25% of limb profile observations with CO_2 ice clouds. The mesospheric peaks in 1.27 μm emission correspond to $O_2(^1\Delta_g)$ volume emission rates (VER) of $\sim 10^5$ photons/cm^{-3}/s (see Fig. 30).

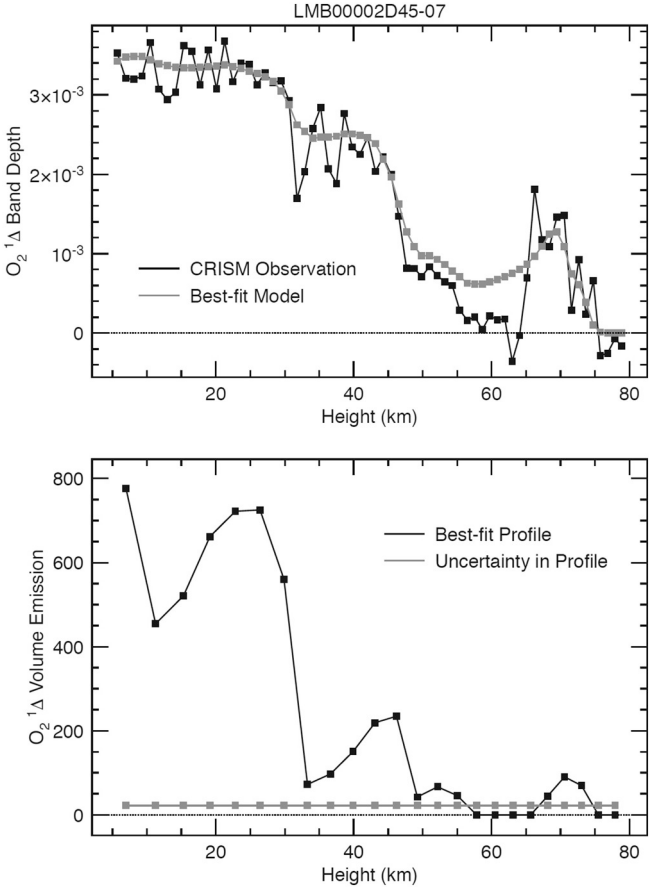

Fig. 30. A pseudo-spherical RT, non-linear profile inversion is performed on the 14May2016 limb observation presented in Fig. 29 (green profile, $L_s = 152^\circ$, 1S356W) to retrieve CO_2 (and H_2O) ice optical depth and $O_2(^1\Delta_g)$ VER. The observed (black) and fitted (grey) $O_2(^1\Delta_g)$ band depth limb profiles are presented in the upper panel. The retrieved vertical profile of $O_2(^1\Delta_g)$ VER (black) and 1σ uncertainty (grey, ~20%) are presented in the lower panel. $O_2(^1\Delta_g)$ VER are in units of 10^3 photons/cm^{-3}/s.

Fig. 29 indicates enhanced $O_2(^1\Delta_g)$ emission in the presence of mesospheric CO_2 ice clouds, but does not separate the local $O_2(^1\Delta_g)$ emission at CO_2 cloud heights from scattering of lower atmospheric $O_2(^1\Delta_g)$ emission (below 40 km in Fig. 29) by these clouds. In order to establish the magnitude of the mesospheric $O_2(^1\Delta_g)$ emission, mesospheric $O_2(^1\Delta_g)$ VER and CO_2 ice opacity are simultaneously retrieved for the 14May2016 CRISM observation in Fig. 29 (green lines, 1S356W, $L_s = 152^\circ$). In this case, CO_2 ice indices are employed for mesospheric aerosol retrieval (versus H_2O ice in Clancy et al., 2017). Fig. 30 presents the results of this retrieval for the full $O_2(^1\Delta_g)$ VER profile (lower panel) and the observed versus retrieved $O_2(^1\Delta_g)$ band depth (upper panel). The employed multiple scattering, limb RT (described in Clancy et al., 2017) includes scattering of lower atmospheric $O_2(^1\Delta_g)$ emission by the simultaneously retrieved mesospheric CO_2 ice cloud opacity. Notice that the observed mesospheric $O_2(^1\Delta_g)$ emission profile is effectively zero below the mesospheric emission peak at 65–75 km (i. e., over 45–65 km), which indicates the enhanced mesospheric $O_2(^1\Delta_g)$ emission occurs over discrete spatial scales as does the CO_2 ice cloud. The employed spherical shell RT cannot simulate this behavior such that the modeled $O_2(^1\Delta_g)$ emission does not fall to zero below the cloud (top panel), whereas the retrieved $O_2(^1\Delta_g)$ VER does. This behavior increases the effective error of the retrieved mesospheric peak in $O_2(^1\Delta_g)$ VER to roughly 20%. The VER units of the bottom panel of Fig. 30 are 10^3 photons/cm^{-3}/s, as compared to 10^6 photons/cm^{-3}/s units presented in Clancy et al. (2017).

8.1. LMDGCM simulations of mesospheric $O_2(^1\Delta_g)$

Surprisingly, the LMD (Laboratoire de Météorologie Dynamique) GCM (General Circulation Model, Lefèvre et al., 2008) simulates comparable mesospheric peaks in $O_2(^1\Delta_g)$ VER corresponding to periods (L_S, LT) and locations (latitude, longitude, altitude) of mesospheric cloud occurrence, but not actually for conditions (i. e., cold atmospheric temperatures) of mesospheric CO_2 cloud formation. LMD GCM simulations of such mesospheric $O_2(^1\Delta_g)$ emission peaks correspond to warm atmospheric layers associated with thermal tides, in which downwelling of atomic oxygen leads to increases in $O_2(^1\Delta_g)$ emission associated with three body recombination of $O_2(O + O + M \rightarrow O_2(^1\Delta_g) + M)$, similar to the origin of polar night $O_2(^1\Delta_g)$ emission

near 60 km (Bertaux et al., 2012; Clancy et al., 2012). This model behavior occurs fairly frequently at the same locations and times as for Mars mesospheric CO_2 ice clouds, although clearly not with the cold temperatures that lead to such clouds. Rather, the warm phase of mesospheric thermal tides produces increased $O_2(^1\triangle_g)$ over similar spatial and seasonal ranges. CRISM limb measurements of mesospheric $O_2(^1\triangle_g)$ at low latitudes are rare (6–7 such measurements) and always correspond to coincident detections of mesospheric CO_2 clouds, which are indicative of very cold atmospheric temperatures. Hence, the CRISM and model results for low latitude mesospheric $O_2(^1\triangle_g)$ emission peaks are not consistent with one another in terms of atmospheric conditions or frequency of occurrence.

It is also true, however, that mesospheric water vapor does substantially affect mesospheric $O_2(^1\triangle_g)$ emission rates. LMD model simulations in which water vapor is arbitrarily decreased by a factor of ten yield 3–4× increases in $O_2(^1\triangle_g)$ emission rates, which approach CRISM measurements of mesospheric $O_2(^1\triangle_g)$ increases. The increased model $O_2(^1\triangle_g)$ emission reflects reductions in odd oxygen (O and O_3) loss rates associated with reduced catalysis by odd hydrogen (OH, HO_2, H) products of water vapor dissociation. The resulting increase in atomic O leads to the largest increase in $O_2(^1\triangle_g)$ emission at mesospheric altitudes, but both O and O_3 are shown to be regulated by water vapor decreases. A factor of ten decrease in water vapor abundance is likely to be an underestimate of water vapor decreases in the presence of mesospheric CO_2 ice clouds, which require local temperature to fall below ~100 K (Listowski et al., 2014). In such conditions, water vapor abundance should decrease by several orders of magnitude. However, it is not straightforward to calculate such water vapor conditions given the complex (and not understood) microphysics and dynamics (in terms of local water transport) of cold mesospheric layers consistent with CO_2 ice cloud formation.

9. Rocket dust?

The final subject of this paper is the singular occurrence of a discrete mesospheric dust layer with large particle sizes (R_{eff} = 2 μm), observed on 26May2010 in northern summer (L_s = 96°) at low latitudes (14S) over the elevated Syria Planum region (104W), as presented in Fig. 31. The observed (solid line) and fitted (dashed line) limb reflectance spectra are presented for an aeroid altitude of 55 km in the left panel, which corresponds to the peak reflectance altitude as demonstrated in the vertical I/F profile presented for a wavelength of 1.24 μm in the right panel. The vertical profile of limb reflectance also indicates that this is a horizontally discrete dust layer due to the vanishing brightness observed below the layer peak. This is a quite faint (I/F ~ 0.005) limb scattering feature, that might not be detectable for limb observations after early 2012 due the change to forward versus backward in orbit limb scanning, after which a diffuse (in altitude) scattered light artifact of similar signal appears in the CRISM limb spectra (although with a very different spectral character). Hence, it is a bit difficult to assess the true frequency of such dust scattering layers in the full CRISM limb data set, although it likely falls below several percent. This compares to the ~1% frequency of detached dust layers reported over L_s = 35–155° in MCS observations (Heavens et al., 2015). It is also interesting to note that the aerosol scattering exhibited in this limb profile just below 40 km altitude indicates water ice clouds with small particle sizes (R_{eff} ~ 0.3 μm). This is very distinct from a large particle size, dust scattering layer some 15 km above it, indicating this mesospheric dust layer is not injected locally. The large dust particle sizes indicated for this mesospheric dust layer would seem to indicate it is of recent origin, given the short fall times for such particle sizes (order of hours, Kahre et al., 2008). Although one such observation is hardly diagnostic, it is interesting to consider this mesospheric dust layer in the context of recent modeling of enhanced dust injection mechanisms (Rafkin, 2012; Spiga et al., 2013; Daerden et al., 2015; Tyler et al., 2017), proposed in part to explain altitude increasing dust mixing ratios in northern summer as observed by MCS (Heavens et al., 2015). However, the mesospheric dust layer reported here (Fig. 31, 55 km) lies well above the maximum dust heights so far simulated in these models (30–40 km in Spiga et al., 2013).

10. Conclusions

A dedicated analysis of 2009–2016 CRISM limb spectra (λ = 0.4–4 μm) regarding dust and ice (H_2O, CO_2) aerosols in the Mars mesosphere (50–100 km) supports the following conclusions:

1) Mesospheric aerosols present a very distinct orbital dichotomy in which CO_2 clouds are restricted to the cold aphelion period (L_s = 0–160°), and H_2O ice clouds and dust are largely restricted to

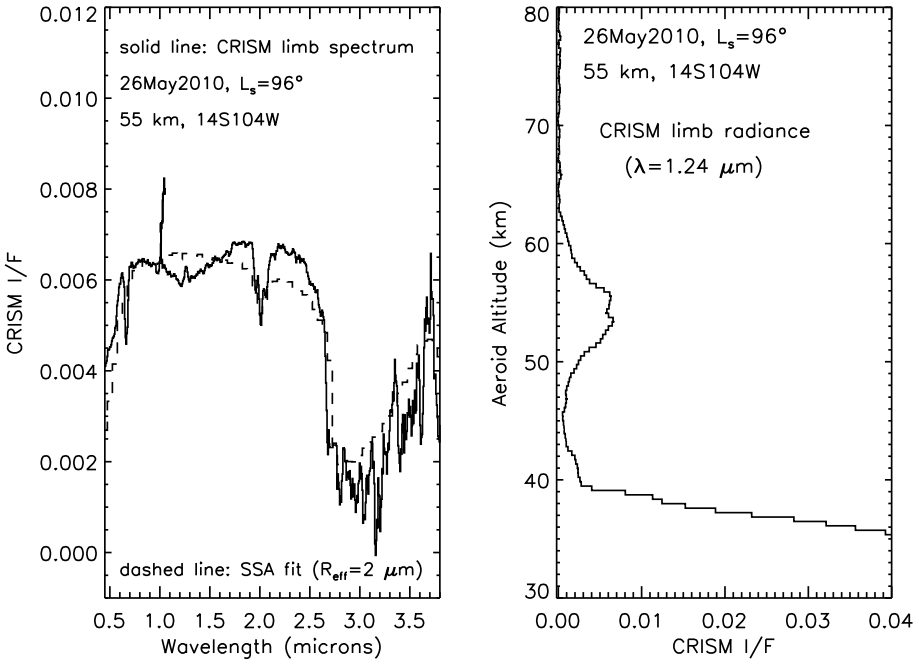

Fig. 31. A unique observation of a northern summer (L_s = 96°) dust layer presents a reflectance spectrum (left panel) indicative of large (R_{eff} = 2 μm) dust particle sizes. The vertical profile of near-IR (λ = 1.27 μm) limb radiance (right panel) indicates the dust layer, centered at 55 km (projected, aeroid), is horizontally discrete. Aerosol scattering spectra just below 40 km (not shown) are consistent with fine H_2O ice clouds (R_{eff} = 0.3 μm).

the perihelion period (L_s = 160–360°).

2) Mesospheric dust aerosols were relatively rare over the non-planet encircling dust storm era of the CRISM limb observations, constituting < 3% of the detected mesospheric aerosols.
3) Mesospheric CO_2 clouds are observed over specific latitude (20S–10N), longitude (0, 70W), and altitude (55–75 km) ranges identified in previous studies. These spatial distributions largely conform to minimum temperatures in the mesosphere around Mars aphelion (e. g., Millour et al., 2014).
4) Mesospheric H_2O ice clouds extend over all four longitude corridors sampled in CRISM limb data, over 50–90 km altitudes, and over 50S–50N sun-lighted (observable) latitudes with a distinct low latitude minimum. These spatial distributions also largely conform to minimum temperatures in the mesosphere around Mars perihelion (e. g., Millour et al., 2014).
5) No aerosol scattering is identified above 90 km altitudes, up to the 120–160 km vertical limit of CRISM limb profiling.
6) Mesospheric CO_2 ice clouds exhibit a broadly distributed range of particle sizes, from R_{eff} of 0.3 to 2.2 μm. The smaller particle sizes are concentrated on the altitude and latitude margins of CO_2 cloud occurrence.
7) Mesospheric H_2O ice clouds exhibit a narrower range of much smaller particle sizes, with R_{eff} predominately falling within 0.1–0.3 μm. On average, mesospheric H_2O cloud particle sizes decrease with increasing altitudes.
8) Peak mesospheric aerosol number densities of 0.1–10 cm^{-3} are estimated from profile retrievals of R_{eff} and τ for a subset of the CRISM limb measurements. H_2O ice clouds with particle number densities of 1 cm^{-3} and $R_{eff} \sim 0.3$ μm roughly correspond to 10% of available water vapor mass at 60 km altitudes.
9) Mesospheric CO_2 ice clouds (and some H_2O ice clouds) exhibit iridescence associated with narrow particle size distributions ($V_{eff} \sim 0.03$), indicative of abrupt and uniform particle growth histories (and perhaps non-aerosol CN).
10) Near-simultaneous CRISM limb spectra and MARCI cloud images determine widely distributed ($\geq 10° \times 10°$ in latitude and longitude) waveform mesospheric CO_2 clouds.
11) MCS mesospheric loop cloud distributions (Sefton-Nash et al., 2013) are broadly consistent with CRISM definitions of the spatial and seasonal distributions of mesospheric aerosols.
12) Near-simultaneous/coincident CRISM and MCS limb observations demonstrate correspondence of near-saturation conditions associated with mesospheric CO_2 and H_2O clouds, and atmospheric heating associated with mesospheric dust aerosols.
13) Near-simultaneous/coincident CRISM and MCS limb observations of mesospheric CO_2 cloud scattering imply similar particle sizes for larger R_{eff} (≥ 1 μm). Smaller CO_2 particle sizes are less apparent in MCS IR channels beyond λ = 16.5 μm (A1), which limits size determinations.
14) Nighttime (3 am) MCS IR channels indicate very large ($R_{eff} \sim 7$ μm) particle size CO_2 clouds with seasonal/spatial distributions similar to daytime (3 pm) CO_2 clouds, very distinct from the fine nighttime CO_2 clouds reported by Montmessin et al. (2006) for the upper mesosphere (> 90 km).
15) Mesospheric CO_2 clouds are occasionally accompanied by (coincident with) mesospheric $O_2(^1\triangle_g)$ emission peaks of order 10^5 photons/cm^{-3}/s. Low water vapor abundances associated with the cold temperatures of CO_2 cloud formation can produce such behavior.
16) A singular case of a discrete dust layer with large particles ($R_{eff} \sim 2$ μm) occurs over Syria Planum at an altitude of 55 km in northern summer (L_s = 96°), as perhaps evidence of non-local dust lifting argued from MCS northern summer dust profiles (Heavens et al., 2015).

Acknowledgements

We are indebted to the excellent MRO and CRISM operations staff for the collection and processing of CRISM limb observations presented here. Grant support for this work was provided by the NASA MDAP Program (under NASA contract award number NNX15AQ07G). Additionally, parts of this work were performed at the Jet Propulsion Laboratory, California Institute of Technology, under a contract with the National Aeronautics and Space Administration.

References

Anderson, E., Leovy, C., 1978. Mariner 9 television limb observations of dust and ice hazes on Mars. J. Atmos. Sci. 35, 723–734. https://doi.org/10.1175/1520-0469035<0723:MTLOOD>2.0.CO;2.

Aoki, S., Sato, Y., Giuranna, M., Wolkenberg, P., Sato, T.M., Nakagawa, H., Kasaba, Y., 2018. Mesospheric CO_2 ice clouds on Mars observed by planetary Fourier spectrometer onboard Mars Express. Icarus 302, 175–190. https://doi.org/10.1016/j.icarus.2017.10.047.

Bell, J.F., Wolff, M.J., Malin, M.C., Calvin, W.M., Cantor, B.A., Caplinger, M.A., Clancy, R.T., Edgett, K.S., Edwards, L.J., Fahle, J., Ghaemi, F., Haberle, R.M., Hale, A., James, P.B., Lee, S.W., McConnochie, T., Noe Dobrea, E., Ravine, M.A., Schaeffer, D., Supulver, K.D., Thomas, P.C., 2009. Mars Reconnaissance Orbiter Mars Color Imager (MARCI): instrument description, calibration, and performance. J. Geophys. Res. Planets 114, E08S92. https://doi.org/10.1029/2008JE003315.

Bertaux, J.L., Gondet, B., Lefèvre, F., Bibring, J.P., Montmessin, F., 2012. First detection of O_2 1.27 μm nightglow emission at Mars with OMEGA/MEX and comparison with general circulation model predictions. J. Geophys. Res. Planets 117, E00J04. https://doi.org/10.1029/2011JE003890.

Clancy, R.T., Sandor, B.J., 1998. CO_2 ice clouds in the upper atmosphere of Mars. Geophys. Res. Lett. 25, 489–492. https://doi.org/10.1029/98GL00114.

Clancy, R.T., Lee, S.W., Gladstone, G.R., McMillan, W.W., Rousch, T., 1995. A new model for Mars atmospheric dust based upon analysis of ultraviolet through infrared observations from Mariner 9, Viking, and PHOBOS. J. Geophys. Res. 100, 5251–5263. https://doi.org/10.1029/94JE01885.

Clancy, R.T., Grossman, A.W., Wolff, M.J., James, P.B., Rudy, D.J., Billawala, Y.N., Sandor, B.J., Lee, S.W., Muhleman, D.O., 1996. Water vapor saturation at low altitudes around Mars aphelion: a key to Mars climate? Icarus 122, 36–62. https://doi.org/10.1006/icar.1996.0108.

Clancy, R.T., Sandor, B.J., Wolff, M.J., Christensen, P.R., Smith, M.D., Pearl, J.C., Conrath, B.J., Wilson, R.J., 2000. An intercomparison of ground-based millimeter, MGS TES, and Viking atmospheric temperature measurements: seasonal and interannual variability of temperatures and dust loading in the global Mars atmosphere. JGR 105, 9553–9572. https://doi.org/10.1029/1999JE001089.

Clancy, R.T., Wolff, M.J., Christensen, P.R., 2003. Mars aerosol studies with the MGS TES emission phase function observations: optical depths, particle sizes, and ice cloud types versus latitude and solar longitude. J. Geophys. Res. Planets 108, 5098. https://doi.org/10.1029/2003JE002058.

Clancy, R.T., Wolff, M.J., Whitney, B.A., Cantor, B.A., Smith, M.D., 2007. Mars equatorial mesospheric clouds: global occurrence and physical properties from Mars global surveyor thermal emission spectrometer and Mars Orbiter Camera limb observations. J. Geophys. Res. Planets 112, E04004. https://doi.org/10.1029/2006JE002805.

Clancy, R.T., Wolff, M.J., Whitney, B.A., Cantor, B.A., Smith, M.D., McConnochie, T.H., 2010. Extension of atmospheric dust loading to high altitudes during the 2001 Mars dust storm: MGS TES limb observations. Icarus 207, 98–109. https://doi.org/10.1016/j.icarus.2009.10.011.

Clancy, R.T., Sandor, B.J., Wolff, M.J., Smith, M.D., Lefèvre, F., Madeleine, J.B., Forget, F., Murchie, S.L., Seelos, F.P., Seelos, K.D., Nair, H.A., Toigo, A.D., Humm, D., Kass, D.M., Kleinböhl, A., Heavens, N., 2012. Extensive MRO CRISM observations of 1.27 μm O_2 airglow in Mars polar night and their comparison to MRO MCS temperature profiles and LMD GCM simulations. J. Geophys. Res. Planets 117, E00J10. https://doi.org/10.1029/2011JE004018.

Clancy, R.T., Smith, M.D., Lefèvre, F., McConnochie, T.H., Sandor, B.J., Wolff, M.J., Lee, S.W., Murchie, S.L., Toigo, A.D., Nair, H., Navarro, T., 2017. Vertical profiles of Mars 1.27 μm O_2 dayglow from MRO CRISM limb spectra: seasonal/global behaviors, comparisons to LMDGCM simulations, and a global definition for Mars water vapor profiles. Icarus 293, 132–156. https://doi.org/10.1016/j.icarus.2017.04.011.

Curran, R.J., Conrath, B.J., Hanel, R.A., Kunde, V.G., Pearl, J.C., 1973. Mars: Mariner 9 spectroscopic evidence for H_2O ice clouds. Science 182, 381–383. https://doi.org/10.1126/science.182.4110.381.

Daerden, F., Whiteway, J.A., Neary, L., Komguem, L., Lemmon, M.T., Heavens, N.G., Cantor, B.A., Hébrard, E., Smith, M.D., 2015. A solar escalator on Mars: self-lifting of dust layers by radiative heating. Geophys. Res. Lett. 42, 7319–7326. https://doi.org/10.1002/2015GL064892.

Deirmendjian, D., 1964. Scattering and polarization properties of water clouds and hazes in the visible and infrared. Appl. Opt. 3, 187. https://doi.org/10.1364/AO.3.000187.

Fedorova, A.A., Korablev, O.I., Bertaux, J.L., Rodin, A.V., Montmessin, F., Belyaev, D.A., Reberac, A., 2009. Solar infrared occultation observations by SPICAM experiment on Mars-Express: simultaneous measurements of the vertical distributions of H_2O, CO_2 and aerosol. Icarus 200, 96–117. https://doi.org/10.1016/j.icarus.2008.11.006.

Fedorova, A.A., Montmessin, F., Rodin, A.V., Korablev, O.I., Määttänen, A., Maltagliati, L., Bertaux, J.L., 2014. Evidence for a bimodal size distribution for the suspended

aerosol particles on Mars. Icarus 231, 239–260. https://doi.org/10.1016/j.icarus.2013.12.015.
González-Galindo, F., Määttänen, A., Forget, F., Spiga, A., 2011. The Martian mesosphere as revealed by CO_2 cloud observations and general circulation modeling. Icarus 216, 10–22. https://doi.org/10.1016/j.icarus.2011.08.006.
Guzewich, S.D., Talaat, E.R., Toigo, A.D., Waugh, D.W., McConnochie, T.H., 2013. High-altitude dust layers on Mars: observations with the thermal emission spectrometer. J. Geophys. Res. Planets 118, 1177–1194. https://doi.org/10.1002/jgre.20076.
Hansen, G.B., 2005. Ultraviolet to near-infrared absorption spectrum of carbon dioxide ice from 0.174 to 1.8 μm. J. Geophys. Res. Planets 110, E11003. https://doi.org/10.1029/2005JE002531.
Hansen, J.E., Travis, L.D., 1974. Light scattering in planetary atmospheres. Space Sci. Rev. 16, 527–610. https://doi.org/10.1007/BF00168069.
Hayne, P.O., Paige, D.A., Schofield, J.T., Kass, D.M., Kleinböhl, A., Heavens, N.G., McCleese, D.J., 2012. Carbon dioxide snow clouds on Mars: south polar winter observations by the Mars Climate Sounder. J. Geophys. Res. Planets 117, E08014. https://doi.org/10.1029/2011JE004040.
Heavens, N.G., Cantor, B.A., Hayne, P.O., Kass, D.M., Kleinböhl, A., McCleese, D.J., Piqueux, S., Schofield, J.T., Shirley, J.H., 2015. Extreme detached dust layers near Martian volcanoes: evidence for dust transport by mesoscale circulations forced by high topography. Geophys. Res. Lett. 42, 3730–3738. https://doi.org/10.1002/2015GL064004.
Heavens, N.G., Kleinböhl, A., Chaffin, M.S., Halekas, J.S., Kass, D.M., Hayne, P.O., McCleese, D.J., Piqueux, S., Shirley, J.H., Schofield, J.T., 2018. Hydrogen escape from Mars enhanced by deep convection in dust storms. Nat. Astron. 2, 126–132. https://doi.org/10.1038/s41550-017-0353-4.
Jaquin, F., Gierasch, P., Kahn, R., 1986. The vertical structure of limb hazes in the Martian atmosphere. Icarus 68, 442–461. https://doi.org/10.1016/0019-1035(86)90050-3.
Kahre, M.A., Hollingsworth, J.L., Haberle, R.M., Murphy, J.R., 2008. Investigations of the variability of dust particle sizes in the Martian atmosphere using the NASA Ames general circulation model. Icarus 195, 576–597. https://doi.org/10.1016/j.icarus.2008.01.023.
Kleinböhl, A., Schofield, J.T., Kass, D.M., Abdou, W.A., Backus, C.R., Sen, B., Shirley, J.H., Lawson, W.G., Richardson, M.I., Taylor, F.W., Teanby, N.A., McCleese, D.J., 2009. Mars Climate Sounder limb profile retrieval of atmospheric temperature, pressure, and dust and water ice opacity. J. Geophys. Res. Planets 114, E10006. https://doi.org/10.1029/2009JE003358.
Kleinböhl, A., Schofield, J.T., Abdou, W.A., Irwin, P.G.J., de Kok, R.J., 2011. A single-scattering approximation for infrared radiative transfer in limb geometry in the Martian atmosphere. J. Quant. Spectrosc. Radiat. Transf. 112, 1568–1580. https://doi.org/10.1016/j.jqsrt.2011.03.006.
Kleinböhl, A., Kass, D.M., Schofield, J.T., McCleese, D.J., 2013. Temperature and dust profiles in Martian dust storm conditions retrieved from Mars Climate Sounder measurements. In: AGU Fall Meeting Abstracts, P41C-1937.
Kleinböhl, A., Schofield, J.T., Kass, D.M., Abdou, W.A., McCleese, D.J., 2015. No widespread dust in the middle atmosphere of Mars from Mars Climate Sounder observations. Icarus 261, 118–121. https://doi.org/10.1016/j.icarus.2015.08.010.
Lefèvre, F., Bertaux, J.L., Clancy, R.T., Encrenaz, T., Fast, K., Forget, F., Lebonnois, S., Montmessin, F., Perrier, S., 2008. Heterogeneous chemistry in the atmosphere of Mars. Nature 454, 971–975. https://doi.org/10.1038/nature07116.
Listowski, C., Määttänen, A., Montmessin, F., Spiga, A., Lefèvre, F., 2014. Modeling the microphysics of CO_2 ice clouds within wave-induced cold pockets in the Martian mesosphere. Icarus 237, 239–261. https://doi.org/10.1016/j.icarus.2014.04.022.
Määttänen, A., Fouchet, T., Forni, O., Forget, F., Savijärvi, H., Gondet, B., Melchiorri, R., Langevin, Y., Formisano, V., Giuranna, M., Bibring, J.P., 2009. A study of the properties of a local dust storm with Mars Express OMEGA and PFS data. Icarus 201, 504–516. https://doi.org/10.1016/j.icarus.2009.01.024.
Määttänen, A., Montmessin, F., Gondet, B., Scholten, F., Hoffmann, H., González-Galindo, F., Spiga, A., Forget, F., Hauber, E., Neukum, G., Bibring, J.P., Bertaux, J.L., 2010. Mapping the mesospheric CO_2 clouds on Mars: MEx/OMEGA and MEx/HRSC observations and challenges for atmospheric models. Icarus 209, 452–469. https://doi.org/10.1016/j.icarus.2010.05.017.
Magalhães, J.A., Schofield, J.T., Seiff, A., 1999. Results of the Mars Pathfinder atmospheric structure investigation. J. Geophys. Res. 104, 8943–8956. https://doi.org/10.1029/1998JE900041.
Malin, M.C., Calvin, W., Clancy, R.T., Haberle, R.M., James, P.B., Lee, S.W., Thomas, P.C., Caplinger, M.A., 2001. The Mars Color Imager (MARCI) on the Mars Climate Orbiter. JGR 106, 17651–17672. https://doi.org/10.1029/1999JE001145.
McCleese, D.J., Heavens, N.G., Schofield, J.T., Abdou, W.A., Bandfield, J.L., Calcutt, S.B., Irwin, P.G.J., Kass, D.M., Kleinböhl, A., Lewis, S.R., Paige, D.A., Read, P.L., Richardson, M.I., Shirley, J.H., Taylor, F.W., Teanby, N., Zurek, R.W., 2010. Structure and dynamics of the Martian lower and middle atmosphere as observed by the Mars Climate Sounder: seasonal variations in zonal mean temperature, dust, and water ice aerosols. J. Geophys. Res. Planets 115, E12016. https://doi.org/10.1029/2010JE003677.
McConnochie, T.H., Bell, J.F., Savransky, D., Wolff, M.J., Toigo, A.D., Wang, H., Richardson, M.I., Christensen, P.R., 2010. THEMIS-VIS observations of clouds in the Martian mesosphere: altitudes, wind speeds, and decameter-scale morphology. Icarus 210, 545–565. https://doi.org/10.1016/j.icarus.2010.07.021.
Millour, E., Forget, F., Spiga, A., Navarro, T., Madeleine, J.B., Montabone, L., Lefèvre, F., Chaufray, J.Y., Lopez-Valverde, M.A., Gonzalez-Galindo, F., Lewis, S.R., Read, P.L., Desjean, M.C., Huot, J.P., MCD/GCM Development Team, 2014. The Mars Climate Database (MCD version 5.1). In: LPI Contributions 1791, pp. 1184.
Mishchenko, M.I., Travis, L.D., Macke, A., 1996. Scattering of light by polydisperse, randomly oriented, finite circular cylinders. Appl. Opt. 35. https://doi.org/10.1364/AO.35.004927.
Mishchenko, M.I., Zakharova, N.T., Khlebtsov, N.G., Videen, G., Wriedt, T., 2016. Comprehensive thematic T-matrix reference database: a 2014–2015 update. J. Quant. Spectrosc. Radiat. Transf. 178, 276–283. https://doi.org/10.1016/j.jqsrt.2015.11.005.
Montmessin, F., Bertaux, J.L., Quémerais, E., Korablev, O., Rannou, P., Forget, F., Perrier, S., Fussen, D., Lebonnois, S., Rébérac, A., Dimarellis, E., 2006. Subvisible CO_2 ice clouds detected in the mesosphere of Mars. Icarus 183, 403–410. https://doi.org/10.1016/j.icarus.2006.03.015.
Montmessin, F., Gondet, B., Bibring, J.P., Langevin, Y., Drossart, P., Forget, F., Fouchet, T., 2007. Hyperspectral imaging of convective CO_2 ice clouds in the equatorial mesosphere of Mars. J. Geophys. Res. Planets 112, E11S90. https://doi.org/10.1029/2007JE002944.
Murchie, S., Arvidson, R., Bedini, P., Beisser, K., Bibring, J.P., Bishop, J., Boldt, J., Cavender, P., Choo, T., Clancy, R.T., Darlington, E.H., Des Marais, D., Espiritu, R., Fort, D., Green, R., Guinness, E., Hayes, J., Hash, C., Heffernan, K., Hemmler, J., Heyler, G., Humm, D., Hutcheson, J., Izenberg, N., Lee, R., Lees, J., Lohr, D., Malaret, E., Martin, T., McGovern, J.A., McGuire, P., Morris, R., Mustard, J., Pelkey, S., Rhodes, E., Robinson, M., Roush, T., Schaefer, E., Seagrave, G., Seelos, F., Silverglate, P., Slavney, S., Smith, M., Shyong, W.J., Strohbehn, K., Taylor, H., Thompson, P., Tossman, B., Wirzburger, M., Wolff, M., 2007. Compact Reconnaissance Imaging Spectrometer for Mars (CRISM) on Mars Reconnaissance Orbiter (MRO). J. Geophys. Res. Planets 112, E05S03. https://doi.org/10.1029/2006JE002682.
Murchie, S.L., Mustard, J.F., Ehlmann, B.L., Milliken, R.E., Bishop, J.L., McKeown, N.K., Noe Dobrea, E.Z., Seelos, F.P., Buczkowski, D.L., Wiseman, S.M., Arvidson, R.E., Wray, J.J., Swayze, G., Clark, R.N., Des Marais, D.J., McEwen, A.S., Bibring, J.P., 2009. A synthesis of Martian aqueous mineralogy after 1 Mars year of observations from the Mars Reconnaissance Orbiter. J. Geophys. Res. Planets 114, E00D06. https://doi.org/10.1029/2009JE003342.
Nair, H., Allen, M., Anbar, A.D., Yung, Y.L., Clancy, R.T., 1994. A photochemical model of the Martian atmosphere. Icarus 111, 124–150. https://doi.org/10.1006/icar.1994.1137.
Neiman, P.J., Shaw, J.A., 2003. Coronas and iridescence in mountain wave clouds over northeastern Colorado. Bull. Am. Meteorol. Soc. 84, 1373–1386. https://doi.org/10.1175/BAMS-84-10-1373.
Plane, J.M.C., Carrillo-Sanchez, J.D., Mangan, T.P., Crismani, M.M.J., Schneider, N.M., Määttänen, A., 2018. Meteoric metal chemistry in the Martian atmosphere. J. Geophys. Res. Planets 123, 695–707. https://doi.org/10.1002/2017JE005510.
Press, W.H., Teukolsky, S.A., Vetterling, W.T., Flannery, B.P., 1992. Numerical Recipes in FORTRAN. The Art of Scientific Computing, 2nd ed. University Press, Cambridge.
Puspitarini, L., Määttänen, A., Fouchet, T., Kleinboehl, A., Kass, D.M., Schofield, J.T., 2016. Analysis of high altitude clouds in the Martian atmosphere based on Mars Climate Sounder observations. J. Phys. Conf. Ser. 012049. https://doi.org/10.1088/1742-6596/771/1/012049.
Rafkin, S.C.R., 2012. The potential importance of non-local, deep transport on the energetics, momentum, chemistry, and aerosol distributions in the atmospheres of Earth, Mars, and Titan. Planet. Space Sci. 60, 147–154. https://doi.org/10.1016/j.pss.2011.07.015.
Sassen, K., 1979. Iridescence in an aircraft contrail. J. Opt. Soc. Am. 69, 1080 (1917–1983).
Sassen, K., 2003. Cirrus cloud iridescence: a rare case study. Appl. Opt. 42, 486–491. https://doi.org/10.1364/AO.42.000486.
Scholten, F., Hoffmann, H., Määttänen, A., Montmessin, F., Gondet, B., Hauber, E., 2010. Concatenation of HRSC colour and OMEGA data for the determination and 3D-parameterization of high-altitude CO_2 clouds in the Martian atmosphere. Planet. Space Sci. 58, 1207–1214. https://doi.org/10.1016/j.pss.2010.04.015.
Sefton-Nash, E., Teanby, N.A., Montabone, L., Irwin, P.G.J., Hurley, J., Calcutt, S.B., 2013. Climatology and first-order composition estimates of mesospheric clouds from Mars Climate Sounder limb spectra. Icarus 222, 342–356. https://doi.org/10.1016/j.icarus.2012.11.012.
Shaposhnikov, D.S., Rodin, A.V., Medvedev, A.S., Fedorova, A.A., Kuroda, T., Hartogh, P., 2018. Modeling the hydrological cycle in the atmosphere of Mars: influence of a bimodal size distribution of aerosol nucleation particles. J. Geophys. Res. Planets 123, 508–526. https://doi.org/10.1002/2017JE005384.
Smith, M.D., Wolff, M.J., Clancy, R.T., 2011. Vertical distribution of aerosols and water vapor using CRISM limb observations. In: Forget, F., Millour, E. (Eds.), Mars Atmosphere: Modelling and Observation, pp. 188–190.
Smith, M.D., Wolff, M.J., Clancy, R.T., Kleinböhl, A., Murchie, S.L., 2013. Vertical distribution of dust and water ice aerosols from CRISM limb-geometry observations. J. Geophys. Res. Planets 118, 321–334. https://doi.org/10.1002/jgre.20047.
Spiga, A., González-Galindo, F., López-Valverde, M.Á., Forget, F., 2012. Gravity waves, cold pockets and CO_2 clouds in the Martian mesosphere. Geophys. Res. Lett. 39, L02201. https://doi.org/10.1029/2011GL050343.
Spiga, A., Faure, J., Madeleine, J.B., Määttänen, A., Forget, F., 2013. Rocket dust storms and detached dust layers in the Martian atmosphere. J. Geophys. Res. Planets 118, 746–767. https://doi.org/10.1002/jgre.20046.. arXiv:1208.5030.
Stamnes, K., Tsay, S.C., Jayaweera, K., Wiscombe, W., 1988. Numerically stable algorithm for discrete-ordinate-method radiative transfer in multiple scattering and emitting layered media. Appl. Opt. 27, 2502–2509. https://doi.org/10.1364/AO.27.002502.
Tomasko, M.G., Doose, L.R., Lemmon, M., Smith, P.H., Wegryn, E., 1999. Properties of dust in the Martian atmosphere from the imager on Mars Pathfinder. J. Geophys. Res. 104, 8987–9008. https://doi.org/10.1029/1998JE900016.
Toon, O.B., Pollack, J.B., Sagan, C., 1977. Physical properties of the particles composing the Martian dust storm of 1971–1972. Icarus 30, 663–696. https://doi.org/10.1016/0019-1035(77)90088-4.

Tyler, D., Barnes, J.R., Wilson, R.J., Murphy, J., 2017. Topographic circulations on Mars: surface pressure, convective boundary layers and network implications. In: Forget, F., Millour, M. (Eds.), The Mars Atmosphere: Modelling and Observation, pp. 1110.

Vincendon, M., Pilorget, C., Gondet, B., Murchie, S., Bibring, J.P., 2011. New near-IR observations of mesospheric CO_2 and H_2O clouds on Mars. J. Geophys. Res. Planets 116, E00J02. https://doi.org/10.1029/2011JE003827.. arXiv:1103.3448.

Warren, S.G., Brandt, R.E., 2008. Optical constants of ice from the ultraviolet to the microwave: a revised compilation. J. Geophys. Res. Atmos. 113, D14220. https://doi.org/10.1029/2007JD009744.

Wolff, M.J., Smith, M.D., Clancy, R.T., Arvidson, R., Kahre, M., Seelos, F., Murchie, S., Savijärvi, H., 2009. Wavelength dependence of dust aerosol single scattering albedo as observed by the Compact Reconnaissance Imaging Spectrometer. J. Geophys. Res. Planets 114, E00D04. https://doi.org/10.1029/2009JE003350.

Yang, P., Baum, B.A., Heymsfield, A., Hu, Y.X., Huang, H.L., Tsau, S.C., Ackerman, S., 2003. Single scattering properties of droxtals. J. Quant. Spectrosc. Radiat. Transf. 79, 1159. https://doi.org/10.1016/S0022-4073(02)00347-3.

Yiğit, E., England, S.L., Liu, G., Medvedev, A.S., Mahaffy, P.R., Kuroda, T., Jakosky, B.M., 2015. High-altitude gravity waves in the Martian thermosphere observed by MAVEN/NGIMS and modeled by a gravity wave scheme. Geophys. Res. Lett. 42, 8993–9000. https://doi.org/10.1002/2015GL065307.. arXiv:1508.03095.